Titre: Title:	Towards Direct Numerical Simulation of a Low-Swirl Laboratory Turbulent CH4/H2 Flame Impinging on an Inclined Wall
Auteur: Author:	Mohammadreza Nozari
Date:	2023
Type:	Mémoire ou thèse / Dissertation or Thesis
Référence: Citation:	Nozari, M. (2023). Towards Direct Numerical Simulation of a Low-Swirl Laboratory Turbulent CH4/H2 Flame Impinging on an Inclined Wall [Mémoire de maîtrise, Polytechnique Montréal]. PolyPublie. https://publications.polymtl.ca/55742/

URL de PolyPublie: PolyPublie URL:	https://publications.polymtl.ca/55742/
Directeurs de recherche: Advisors:	Bruno Savard
Programme: Program:	Génie mécanique

POLYTECHNIQUE MONTRÉAL
affiliée à l'Université de Montréal

Towards Direct Numerical Simulation of a Low-Swirl Laboratory Turbulent CH_4/H_2 Flame Impinging on an Inclined Wall

MOHAMMADREZA NOZARI
Département de génie mécanique

Mémoire présenté en vue de l'obtention du diplôme de *Maîtrise ès sciences appliquées*
Génie mécanique

Août 2023

POLYTECHNIQUE MONTRÉAL
affiliée à l'Université de Montréal

Ce mémoire intitulé :

Towards Direct Numerical Simulation of a Low-Swirl Laboratory Turbulent CH_4/H_2 Flame Impinging on an Inclined Wall

présenté par **Mohammadreza NOZARI**
en vue de l'obtention du diplôme de *Maîtrise ès sciences appliquées*
a été dûment accepté par le jury d'examen constitué de :

Roberto PAOLI, président
Bruno SAVARD, membre et directeur de recherche
Bruno BLAIS, membre

ACKNOWLEDGMENTS

I'm grateful for my family, my parents and my brother, who have supported me all throughout my life, including this journey.

I want to express my deep gratitude towards Prof. Bruno Savard who gave me the opportunity to work under his supervision and gain invaluable knowledge and experience, and also his help and support which made this thesis become possible. Next, I want to thank Patrizio Vena and Luming Fan from the National Research Council Canada (NRC), Marc Day and Lucas Esclapez from the National Renewable Energy Laboratory (NREL) of the United States, Sandeep Jella from Siemens Energy Canada, and also my lab-mate Martin Vabre for their supports and contributions to this project.

I also acknowledge the support of the Natural Sciences and Engineering Research Council of Canada (NSERC) (funding reference numbers RGPIN-2019-04309, RGPAS-2019-00131, DGCER-2019-00390). Computational resources were provided by Compute Ontario and Digital Research Alliance of Canada.

RÉSUMÉ

La transition vers des carburants à faibles émissions de carbone est sans doute le sujet le plus recherché dans la communauté de la combustion de nos jours. L'hydrogène s'est révélé très prometteur pour son utilisation dans les turbines à gaz destinées aux secteurs de la production d'électricité et des transports. Dans les turbines à gaz, les flammes subissent des interactions complexes avec les parois de la chambre de combustion, qui ont un impact sur le rendement du moteur et les émissions polluantes. Ces interactions, qui ont lieu à l'échelle microscopique, ne sont pas bien comprises et ne sont pas bien prises en compte dans les logiciels de simulation commerciaux. L'objectif de ce projet est de résoudre de telles interactions jusqu'aux plus petites échelles pertinentes, grâce à la simulation numérique directe (DNS). Plus précisément, une configuration est établie pour effectuer une DNS d'une flamme de laboratoire de CH_4/H_2 prémélangée, pauvre et à faible tourbillon frappant un mur incliné. L'accent est mis sur trois aspects : 1) les conditions aux limites des flux entrants, 2) les exigences de résolution de la couche limite pour le solveur utilisé, et 3) les résultats préliminaires, sous-résolus. Un défi majeur concernant la simulation d'une flamme en laboratoire consiste à prescrire les bons profils d'entrée. Deux approches ont été testées. La première approche consiste à utiliser les profils mesurés expérimentalement pour la moyenne et la variance des trois composantes de vitesse à la sortie de l'injecteur comme débit entrant. Les fluctuations de vitesse turbulente sont superposées à l'aide d'un spectre modèle. Dans la deuxième approche, une simulation auxiliaire de type LES (simulation aux grandes échelles) de l'écoulement à l'intérieur de l'injecteur a été utilisée pour prescrire l'écoulement entrant pour la simulation principale. Les résultats de la deuxième approche ont montré, dans un écoulement non réactif, un meilleur accord avec les résultats expérimentaux et ont donc été choisis comme écoulement entrant pour la simulation principale de l'interaction flamme-paroi. Ensuite, une série de DNS est effectuée sur des couches limites thermiques turbulentes non réactives pour évaluer la résolution requise pour résoudre la couche limite turbulente formée sur la paroi inclinée dans la simulation réactive. Trois ensembles de simulations sont effectués en utilisant différentes résolutions au niveau du mur, et il est montré qu'avoir $y^+ \approx 1.4$ sur la première cellule est suffisant pour obtenir des résultats indépendants du maillage en termes de statistiques du premier et du deuxième ordre. Enfin, la simulation réactive de la flamme tourbillonnante interagissant avec le mur est réalisée et des résultats préliminaires sous-résolus sont présentés. Un bon accord en termes de hauteur et de position de décollage de la flamme est observé entre la simulation et l'expérience. Un gros nuage de formaldéhyde est observé dans le domaine. Ceci est attribué à richesse localement réduite et à un taux de déformation

élevé qui entraînent une combustion incomplète et des espèces intermédiaires non brûlées. Un flux de chaleur important vers le mur a également été observé. Avec la confiance apportée par les résultats de cette thèse, la résolution sera ensuite augmentée au niveau DNS.

ABSTRACT

Transitioning to low-carbon fuels is arguably the highest sought-after topic in the combustion community nowadays. Hydrogen has shown good promise for usage in gas turbines for the power generation and transport sectors. In gas turbines, flames undergo complex interactions with the combustor walls, which impact engine efficiency and pollutant emissions. These interactions, which take place at the microscale, are not well understood and are not well accounted for in commercial simulation software. The aim of this project is to resolve such interactions down to the smallest relevant scales, through direct numerical simulation (DNS). Specifically, a setup is established to perform a DNS of a laboratory premixed, lean, low-swirl CH_4/H_2 flame impinging on an inclined wall. The emphasis is put on three aspects: 1) inflow boundary conditions, 2) boundary layer resolution requirements for the solver used, and 3) preliminary, under-resolved, results. A major challenge regarding simulating a laboratory flame is prescribing the right inflow profiles. Two approaches have been tested. The first approach consists of using the experimentally measured profiles for average and rms of the three velocity components at the nozzle outlet as the inflow. Turbulent velocity fluctuations are superimposed using a model spectrum. In the second approach, an auxiliary large eddy simulation of the nozzle flow has been used to prescribe the inflow for the main simulation. Results in a non-reactive environment from the second approach showed better agreement with the experimental results, and hence it was chosen as the inflow for the main flame-wall interaction simulation. Next, a series of DNS are performed on non-reactive, turbulent thermal boundary layers to assess the required resolution to resolve the turbulent boundary layer formed on the inclined wall in the reactive simulation. Three sets of simulations are performed using different resolutions at the wall, and it is shown that having $y^+ \approx 1.4$ on the first cell is enough to obtain grid independent results in terms of first and second order statistics. Finally, the reactive simulation of the swirl flame interacting with the wall is performed and preliminary, under-resolved results are presented. Good agreement in terms of flame lift-off height and position is observed between the simulation and the experiment. A large cloud of formaldehyde is observed in the domain. This is shown to be attributed to locally reduced equivalence ratio and high strain rate which result in incomplete combustion and unburned intermediate species. Large amount of heat flux to the wall was also observed. With the confidence provided by the results in this thesis, resolution will next be increased to DNS level.

TABLE OF CONTENTS

LIST OF TABLES

LIST OF FIGURES

LIST OF SYMBOLS AND ACRONYMS

DNS	Direct numerical simulation
GT	Gas turbine
LES	Large eddy simulation
RANS	Reynolds averaged Navier-Stokes
FWI	Flame-wall interaction
rms	root mean square
HOQ	Head-on quenching
SWQ	Side-wall quenching
EB	Embedded boundary
PIV	Particle image velocimetry
PLIF	Planar laser induced fluorescent
ODE	Ordinary differential equation
AMR	Adaptive mesh refinement
HAB	Height above burner
HRR	Heat release rate
JPDF	Joint probability density function
SFWI	Swirl flame-wall interaction
TBL	Turbulent boundary layer
NRSF	Non-reactive swirl flow
HIT	Homogeneous isotropic turbulence

LIST OF APPENDICES

CHAPTER 1 INTRODUCTION

1.1 Background

Combustion still contributes to more than 85% of the world's energy consumption [3]. It is also the main source of greenhouse gas emission on the planet and is responsible for smog and air pollution in large cities [13]. One on-going line of research to reduce pollution is towards using renewable energy. However, renewable energy sources such as wind and solar are generally intermittent and unpredictable and can be specific to certain geographical locations [14, 15]. Combustion, on the other hand, is not intermittent and can be utilized in any place. This makes it a great supplement for renewable energy. Gas turbines (GTs), in particular, are suitable choices in that they are highly flexible in terms of operability [16].

Restricting carbon footprint and nitrogen oxides (NO_x) to certain thresholds are among the main focuses of research nowadays [17, 18], as was agreed upon at COP21 in Paris [15]. As a result, we observe a decrease in nitrous oxide (also known as NO_x) emissions, e.g., in the US [3], which is a great accomplishment. However, there is still much to do to minimize the CO_2 emissions of combustion systems, such as GTs, which are heavily used for power generation and aeronautical propulsion. Various combustion technologies have been proposed in the last few years to reduce pollution and increase efficiency in GTs, such as MILD (moderate or intense low oxygen dilution) [19], LPP (lean prevaporized premixed) [20], RQL (rich-quench-lean) combustors [21], using hydrogen-based and bio fuels [15, 22–25], etc. All of these technologies seek three main goals: 1. pollution reduction (most importantly NO_x and CO_x), 2. increased efficiency, 3. removing the need for fossil fuels.

One growing and promising line of research in the combustion community is using low-carbon fuels such as hydrogen in engines, e.g., GTs [26, 27]. This calls for immediate need to study low-carbon flames in GT-relevant environments to gradually replace carbon-rich fuels such as natural gas. That being said, many challenges are attributed with burning hydrogen. To mitigate high NO_x emissions, hydrogen flames should be at lean conditions to reduce the flame temperature and thermal NO_x as a consequence, which is the main source of NO_x production in flames [28]. Lean hydrogen flames are more prone to thermo-diffusive instability, low combustion efficiency with high amounts of unburned fuel emitted, and also flashback [29–31]. Since GT combustors operate in closed vessels, the flame is inevitably interacting with the combustor walls. The interaction between the latter is called flame-wall interaction (FWI) in the literature and is widely studied. FWI can exacerbate leakage of unburned fuel or combustion intermediates due to heat loss to the cold wall, which can be

more severe in lean flames (they can be understood also as "weak" flames) [32–35].

The work in this thesis aims at providing better understanding of the role of FWI on the stability and emission characteristics of lean high H_2 content flames, representative of GTs.

The flow in the combustor of a GT is highly turbulent due to the rapid fluctuations in the incoming air, and also the complex flow pattern which is a combination of the swirler and cooling holes [3,16]. In order to predict the convoluted flow behaviour in the combustor, one can either perform experimental investigations or numerical simulations. Doing experiments in the realistic situations in a GT combustor (very high pressure and temperature) is very expensive. Moreover, optical measurements are only viable in transparent environments. Numerical simulations come with a much lower cost and time.

Three approaches have been developed in the numerical realm to simulate a turbulent reacting flow: Reynolds averaged Navier-Stokes (also called "RANS"), large eddy simulation (called "LES"), and direct numerical simulation (called "DNS") [36,37]. In the RANS framework, none of the turbulent motions are resolved, though their effect on the mean flow is approximated by closure models, including for the Reynolds stresses, the chemical reaction source term, and other unclosed terms. In LES, the "filtered" Navier-Stokes equations are solved and only large eddies in the flow are resolved. These equations contain additional terms which account for the effects of the small-scale eddies (eddies smaller than the filter size) on the large-scale eddies and chemical reactions. Models called sub-filter-scale models are required for these unresolved stresses and filtered chemical source term [5]. Finally, DNS solves the instantaneous Navier-Stokes equations governing the flow motion and resolves all the length and time scales, from integral to Kolmogorov scale, attributed with the flow and the flame.

In this project, a setup is put in place for direct numerical simulations of lean, turbulent, laboratory low-carbon flames interacting with a wall, which will be used to unravel the complex flow-chemistry interactions.

1.2 Flame-wall interaction phenomena and the pivotal role of direct numerical simulations

Almost all combustion engines operate in closed vessels, such that the flame frequently interacts with the wall. This is not a trivial process since studies have shown that the structure of a flame close to a wall differs considerably from an adiabatic one [38, 39]. Downsizing of the engines in the last decades has also accentuated this phenomenon in the combustors.

FWI controls the lifetime and also the cooling techniques used on the chamber wall [6] of a gas

turbine combustor. Studies show that wall heat flux can reach as high as 1 MW/m^2 [27, 39] in a combustor. It can also have crucial consequences on the pollution and efficiency of the combustor. A flame near the wall impacts the turbulent boundary layer and vice versa, leading to changes in flame properties such as flame speed and chemical reaction rates. Heat flux from the cold wall degrades reaction rates and leads to incomplete combustion. Unburned hydrocarbons (UHC) and CO emissions are the main consequences of incomplete combustion [16].

This phenomenon is quite complicated since it involves three components: flame, turbulence, and wall. Figure 1.1 illustrates the interactions between these three components. The wall impacts the flow, in a different way it impacts non-reactive flow, and previous laws on the turbulent boundary layer such as law-of-the-wall are not applicable to the reactive boundary layer [38]. Turbulence-flame interactions were also found to be different from the adiabatic premixed flames [38, 39].

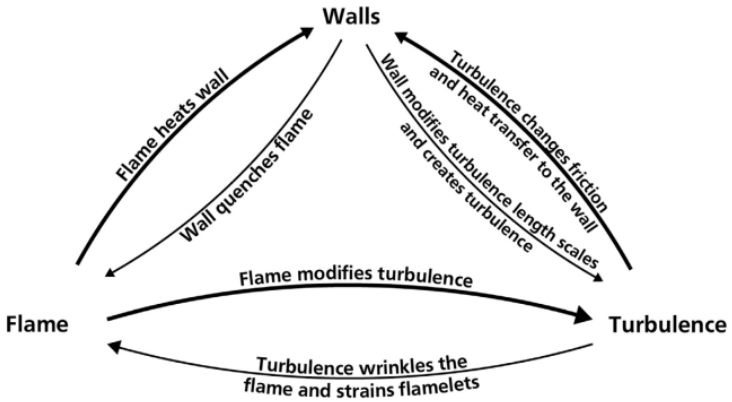

Figure 1.1 Interplay of flame, wall and turbulence. Taken from [1].

Due to its complexity, FWI has not yet been understood thoroughly in the literature. Existing premixed turbulent combustion models do not involve special treatment for wall effects [40]. Thus, there is vital need for combustor designers to develop dependable turbulent flame models that take into account the wall effects. DNS is a great tool to study this phenomenon. This kind of simulation can capture the fine length and time scales in the near-wall region. Doing experiments using laser diagnostics is hard to do in that region because of small length scales in the near-wall region and has been limited to few research groups [7]. For instance, for atmospheric stochiometric methane/air flame, head-on quenching configuration lasts for around 0.2 ms and quenching distance is around 0.1 mm. Also, scattering of the laser beams from the wall may result in low signal to noise ratio and must be carefully taken care of [27]. Moreover, the three-dimensional structure of turbulence and flame structure is

not easy to capture with these methods. DNS can be a great tool to capture the complex three-dimensional structures in the near-wall region with enough resolution and accuracy.

1.3 Challenges with hydrogen combustion

Hydrogen flames are intrinsically unstable due to their high diffusivity [2]. This type of instability arises in the flames with fuel Lewis number lower than unity. Lewis number is the ratio of thermal and mass diffusivity. Figure 1.2 shows a schematic of this type of instability. Once a flame is wrinkled, it is divided into concave and convex segments to the unburned side. Since concave segment is reactant-deficient and the mass diffusivity is higher than heat diffusivity, fuel consumption speed increases and the flame wrinkles even more which means the flame is intrinsically unstable. The opposite scenario goes for higher than unity Lewis number flames.

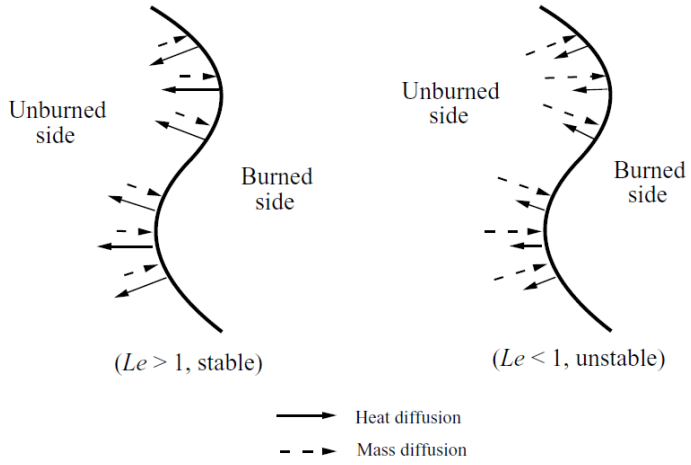

Figure 1.2 Illustration of thermo-diffusive cellular instability. Taken from [2].

This type of instability leads to cellular burning structure of the flame and enhanced burning rates as shown in Figure 1.3 [41]. This figure shows the cellular structure of lean hydrogen-air mixtures expanding spherically using Schlieren technique on the left column, and a stable flame front on the right column. High turbulence reduces this instability on a macrospoic point of view, but local instabilities are shown to be still present [42]. Modeling these instabilities requires modeling the interplay of chemistry and transport processes in the turbulent flow, which demands high temporal and spatial resolutions and detailed chemistry and transport models [43].

Moreover, hydrogen combustion comes with high adiabatic flame temperatures which leads

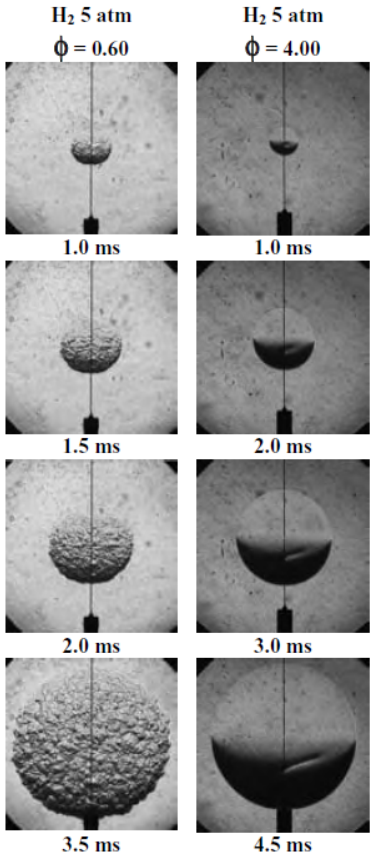

Figure 1.3 Thermo-diffusive instability of spherically expanding hydrogen/air flames using the Schlieren technique, showing the presence of thermo-diffusive instability for the lean case. Equivalence ratio (ϕ) is defined as the mass-based oxidizer/fuel ratio at stochiometric conditions over actual condition. Taken from [2].

to high NO_x emissions [30] and can also result in reduced combustor lifetime due to high thermal stresses on the combustor wall [44]. As a result, hydrogen is mainly burned in very lean conditions to minimize NO_x emissions.

1.4 Knowledge gap

As discussed above, there is a vital need for more detailed analysis of wall and heat loss effects on low-carbon flames to facilitate low-pollution, high-efficiency GT combustors. Direct numerical simulations can give valuable insights since they resolve all the relevant flow and chemical time and length scales. So far, there has been very limited research on swirl flames interacting with walls, which are the typical type of flames in gas turbines. Quenching mechanism, pollutant emission, heat transfer, and flame structure in the near-wall region of

swirl flames is not well understood. Targeting laboratory flames in this project also enables us to combine the advantage of experiments, which allow to do large parametric studies, and simulation that enables access to fine-grained data everywhere in the domain.

1.5 Objectives

To fill the knowledge gap mentioned above, this project aims at developing a setup for DNS of low-carbon swirl flames interacting with a wall. More specifically, the setup replicates a laboratory flame studied in [10]. The wall in the study is inclined which enables investigating flame quenching in both wall-normal and wall-parallel scenarios. The premixed fuel-air mixture is lean ($\phi = 0.41$), and the fuel consists of 70% H_2 and 30% CH_4 by volume. This represents the ideal conditions for GT applications, limiting both carbon and NO_x emissions. Particularly, the objectives are as follows: 1) develop a setup for DNS of laboratory lean, low-carbon swirl flames interacting with a wall, 2) perform a preliminary numerical analysis on the flame structure, 3) identify and quantify the role of heat loss to the wall.

1.6 Thesis outline

The outline of the next chapters in the thesis is as follows. First, a literature review of the topics related to the project including premixed flames (both laminar and turbulent), highly turbulent flames, flame-wall interaction, and finally, DNS of laboratory turbulent flames is given. Next, the methodology used to perform the simulations is discussed. Simulations performed include non-reactive swirl flows, turbulent thermal boundary layer, and finally swirl flame-wall interaction. In the next chapter, results of the simulations are presented and discussed. Then, a conclusion is given.

CHAPTER 2 LITERATURE REVIEW

The literature review, based on the scope of this project, can be divided into five major parts: laminar premixed flames, turbulent premixed flames, FWI (including laminar and turbulent flames), high turbulence flames (high Ka flames), and DNS of laboratory turbulent flames. It is noteworthy to mention that the author of the thesis has contributed to Ref. [10], which is reviewed in subsection 2.3.2. However, this contribution is not sufficiently important to be included in the Results chapter, and is not explicitly mentioned.

2.1 Laminar premixed flames

Laminar premixed flames are used frequently, examples include ovens, heating devices, and Bunsen burners. Studying them can also produce fruitful results applicable to turbulent flames and many turbulent flame theories are based on laminar flames. A schematic of a laminar premixed flame is shown in Figure 2.1a. The laminar flame, also known as deflagration wave, moves towards a combustible mixture, or unburned mixture (denoted by subscript u in Figure 2.1a), and the products or burned mixture are left behind the wave (denoted by subscript b). On a wave-relative coordinate, the unburned mixture moves towards the wave with velocity $u_u = S_L$ and the burned products leave the wave with velocity u_b. Figure 2.1b shows the structure of such a laminar 1D flame. The unburned mixture enters the domain from the left side. The coordinate system is located on the flame. The flame is divided into two main zones: a preheat zone and a reaction zone. In the preheat zone little heat is released and the mixture is heated up by conduction from the reaction zone downstream, hence the temperature rises continuously until ignition occurs and large heat release rate is observed in the reaction zone. Hence it can be argued that the preheat zone is dominated by diffusive and convective processes, whereas the reaction zone is dominated by reaction and diffusion [2]. Generally speaking, the thickness of the reaction zone is much less than that of the preheat zone. Consumption of the deficient reactant in the reaction zone generates a concentration gradient in the preheat zone. For mixtures with $Le = 1$, the rate of temperature increase corresponds to the rate of concentration decrease.

Each laminar flame is recognized with two distinctive values: laminar flame thickness (l_F) and laminar flame speed (S_L). These values are affected by fuel-oxidizer mixture properties.

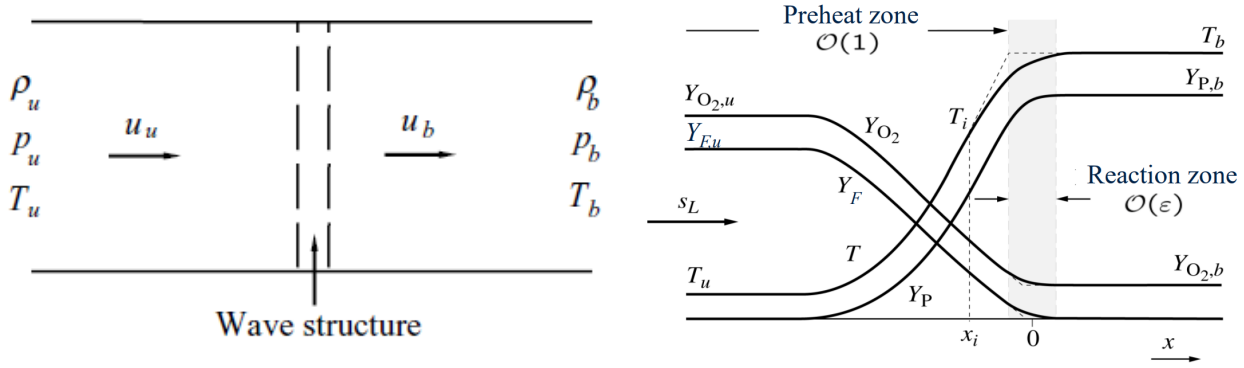

(a) (b)

Figure 2.1 (a) 1D premixed combustion wave sketch. Taken from [3]. (b) Structure of a laminar 1D flame. Taken from [4].

2.2 Turbulent premixed flames

Turbulence is still not fully understood in classical physics. There is no accurate definition of turbulence, but there are some characteristics that are attributed with all turbulent flows: they are irregular (random), diffusive, three-dimensional, dissipative, and occur at large Reynolds numbers [45].

Although turbulent flames are not well understood, they are the type of flames that occur in most combustion engines [2]. Turbulence increases burning rate, compared to laminar flames, by increasing heat exchange and mixing between reactants and burned products. Turbulence results in flame wrinkling which increases the flame area available for reaction. However, quenching can also be accentuated because of intense eddies. Chemistry can also impact turbulence. For example, because of heat release, Reynolds number can decrease due to density decrease and viscosity increase, which can have laminarization effects on the flow [2]. Chemistry can also affect turbulence via enstrophy generation through baroclinic torque [46].

The integral length scale, l_0, is the length scale with the largest turbulent kinetic energy (TKE) density in wave number space. Because of that, eddies in this length scale are named energy-containing eddies. This parameter is attributed to large-scale instabilities of the flow and is bound by the dimensions of the device/confinement [3]. Assuming isotropy, TKE can be expressed as:

$$k \approx \frac{3{u_0'}^2}{2} \tag{2.1}$$

where u_0' is the rms of velocity fluctuations. TKE dissipation rate can be estimated using the following:

$$\epsilon \approx \frac{{u_0'}^3}{l_0} \tag{2.2}$$

At the other end of the length scale cascade, lies the Kolmogorov length scale, η which is associated with the smallest eddies in the flow and where kinetic energy dissipates into heat via viscous effects:

$$\eta \approx (\frac{\nu^3}{\epsilon})^{1/4} \tag{2.3}$$

where ν is the kinematic viscosity. Practical engines operate at extreme levels of turbulence intensity which is attributed with large Karlovitz numbers. Karlovitz number (Ka) is defined as the ratio of flame time to Kolmogorov time, $Ka = t_F/t_\eta$. Flame time can be expressed using $t_F = D/{S_L}^2$, where D is thermal diffusivity. Kolmogorov time is given by $t_\eta = (\nu/\eta)^{0.5}$. There is also a second Karlovitz number based on the reaction zone thickness (l_δ) defined as $Ka_\delta = {l_\delta}^2/\eta^2 = \delta^2 Ka$ where δ is the inner layer to flame thickness ratio. Turbulent Damköhler number (Da) is also defined as $Da = S_L l_0/u_0' l_F$.

Figure 2.2a shows the diagram known as Borghi-Peters diagram for turbulent premixed flames [5]. Based on the ratio of the velocity fluctuation over laminar flame speed, and integral length scale over flame thickness, premixed flames are divided into five major regimes.

In the *Laminar flame regime* turbulence intensity is weak and the flame remains laminar with low levels of wrinkling. In the *Wrinkled flamelet regime* since Ka<1, the flame thickness is smaller than the Kolomogorov length scale. Hence, the laminar flame structure stays almost intact. Since $u_0' < S_L$, as the flame surface travels through the eddies, it is weakly wrinkled (see Figure 2.2b(I)). In the *Corrugated flamelet regime*, since Ka<1, the flame is laminar, however, since $u_0' > S_L$, it becomes highly corrugated during traversing of the eddy (see Figure 2.2b(II)). The *Thin reaction zones regime* is bounded with Ka=1 from below and Ka_δ=1 from above. In this condition, small eddies can enter inside the preheat zone and broaden the flame. This results in enhanced mass transfer and mixing (see Figure 2.2b(III)). The reaction sheet, however, is only wrinkled. In the *Broken reaction zones regime* the Kolmogorov eddies are smaller than the reaction zone thickness and can penetrate it. This phenomenon accelerates heat transfer and species diffusion to the preheat zone which can cause extinction of the flame.

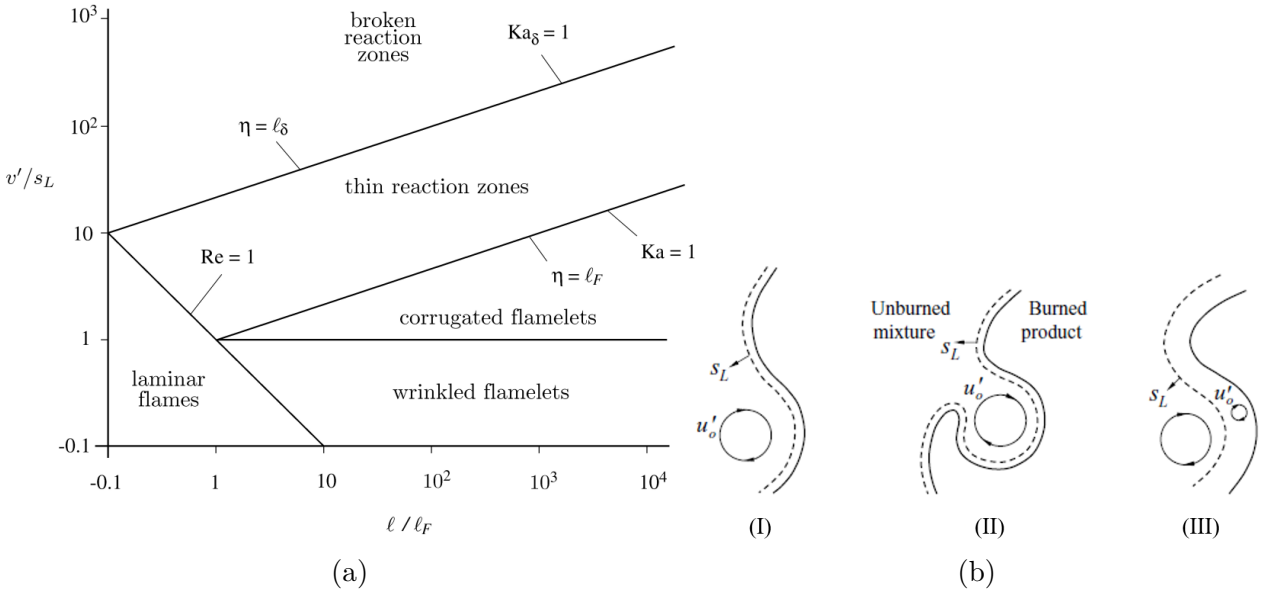

Figure 2.2 (a) Regime diagram for turbulent premixed flames, taken from [5]. (b) Different kinds of flame-vortex interactions, resulting in different flamelet regimes: (I) Weak interaction of vortex and flame ($u'_0 < S_L$), causing wrinkled flamelet. (II) Strong interaction of flame and vortex ($u'_0 > S_L$) causing corrugated flamelet. (III) Strong interaction of vortex and eddies, small eddies entering into the preheat zone [5].

2.2.1 High Ka flames

Flames in most practical engines feature high turbulence intensities [47] and Reynolds numbers. Simulating these flames comes with huge computational costs since they are attributed with a broad range of length and time scales [37]. As a result, few DNS studies of these flames have been performed so far [42, 43, 48–51]. Performing experimental measurements of these flames also is challenging and only few research groups have studied these flames [47, 52–57]. That said, understanding the complex flow-chemistry interaction in these flames is crucial for design and optimization of combustion systems. Recent studies have shown that the flame exhibits behaviours which are far different from the known laminar flame structures [49].

Savard et al. [48] performed DNS of n-heptane/air premixed flames up to $Ka \approx 300$. They showed that turbulence affects the flame to a large degree for unity Lewis number flames. Preheat zone of the flame was observed to broaden significantly. However, it was observed that the structure of this flame (unity Lewis number) is very similar to the laminar one in temperature space (species mass fractions vs. temperature). On the other hand, turbulence affects the structure of the flames with non-unity Lewis significantly so that the flame lies between a flamelet with full transport and a flamelet with unity Lewis number. Aspden

et al. performed DNS of very high Karlovitz number (up to 9000) methane and hydrogen flames. They showed that turbulence can broaden the reaction zone only for hydrogen flame for $Ka \approx 9000$, by an order of magnitude, and thermo-diffusive effects were not seen in this regime [49]. Mohammadnejad et al. [47] studied turbulent methane flames with turbulence intensities (u_0'/S_L) up to 45 and showed that the preheat zone can be broadened up to a factor of 6 compared to the laminar flame, which was consistent with previous findings. However, they also observed thickening of the reaction zone for a flame with $Ka \approx 76$ by a factor of 4. Fan et al. investigated turbulent jet ammonia flames up to $Ka \approx 4700$ [54, 58]. They also observed that the reaction layer remains thin up to $Ka \approx 300$. However, they observed significant thickening of the reaction layer (marked by NH in these flames) for the flame with $Ka > 600$ and set the boundary for transition from thin reaction zone to distributed reaction zones between $Ka \approx 300 - 600$. This boundary for methane flames on the same burner was $Ka \approx 100$ [59] while other studies with larger burners suggested $Ka \approx 550$ [60]. They argued that not only fuel type can control the regime change in turbulent flames, burner size and geometry can also impact such transition.

These studies show that the flame structure at high Ka is quite unpredictable and different from the laminar one. Different conclusions are made for various fuels in different configurations. For example, there is not a unanimous conclusion regarding the onset of the distributed reaction zones in the literature. Further studies on high Ka flames can pave the way to understand these flames in more detail.

2.3 Flame-wall interaction

FWI can be divided into two categories, laminar and turbulent. Although almost all engines operate in a turbulent regime, it is beneficial to study laminar FWI as it gives fundamental insights into the quenching phenomenon occurring in practice.

2.3.1 Laminar FWI

Two basic configurations may occur in a premixed laminar flame undergoing interactions with a wall: head-on quenching (HOQ), and side-wall quenching (SWQ), as shown in Figure 2.3. In the HOQ scenario, the flame front is almost parallel to the wall and propagates toward the unburned mixture in the vicinity of the wall and stops at a certain distance (y_H). In the SWQ configuration, the flame front is perpendicular to the wall surface with a distance (y_S), which is higher than its counterpart y_H and leads to lower heat flux to the wall [6]. These two configurations will be discussed in more detail.

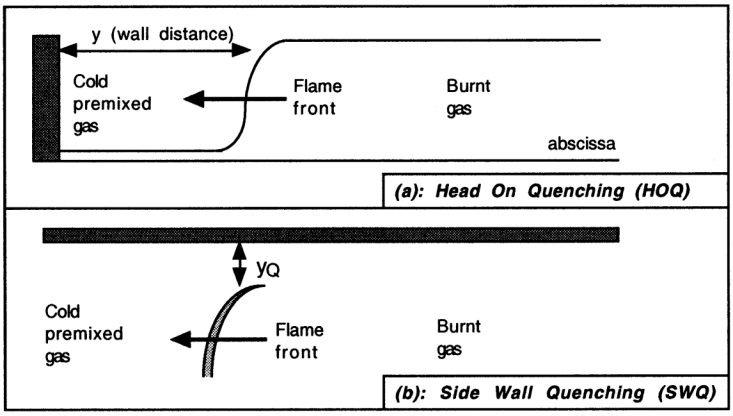

Figure 2.3 FWI configurations of a laminar premixed flame interacting with a wall. Taken from [6].

Head-on quenching

Two parameters are often used to characterize FWI: minimum distance of the flame from the wall and maximum heat flux to the wall [61]. The Peclet number, Pe is the non-dimensional parameter for measuring the flame distance from the wall and is defined as flame-wall distance over unstrained laminar flame thickness. Maximum wall heat flux coincides with the minimum flame distance from the wall [7]. Maximum wall heat flux is denoted as $\dot{Q}_{N,Q}$ which is the heat flux normalized by the unstrained laminar flame power. In the literature, for HOQ without thermal boundary layer, values of $\dot{Q}_{N,Q}$ around 1/3 and 0.13 are reported for hydrocarbons and hydrogen fuels, respectively [62].

Head-on quenching (HOQ) is always a transient process [7]. In a head-on quenching scenario, the flame propagates perpendicular to the wall. Peclet number decreases linearly with time. As the flame approaches the wall, the flame starts to lose its power and starts to lose heat to the wall. Poinsot et al [63] name this region the "influence zone" as depicted in Figure 2.4. Heat flux to the wall rises until it overcomes the heat release from the reactions. As a result unburned fuel, intermediate species and radicals are left in a near-wall region called the "quenching zone". This minimum distance of the flame to the wall is defined as the quenching distance, and the related Peclet number is Pe_Q. Quenching distance is dependent on the gas mixture properties and the wall temperature [64–67]. For HOQ, minimum Peclet number, Pe_Q, was reported around 3.5 for laminar flames [7]. This zone is attributed with fairly low temperatures.

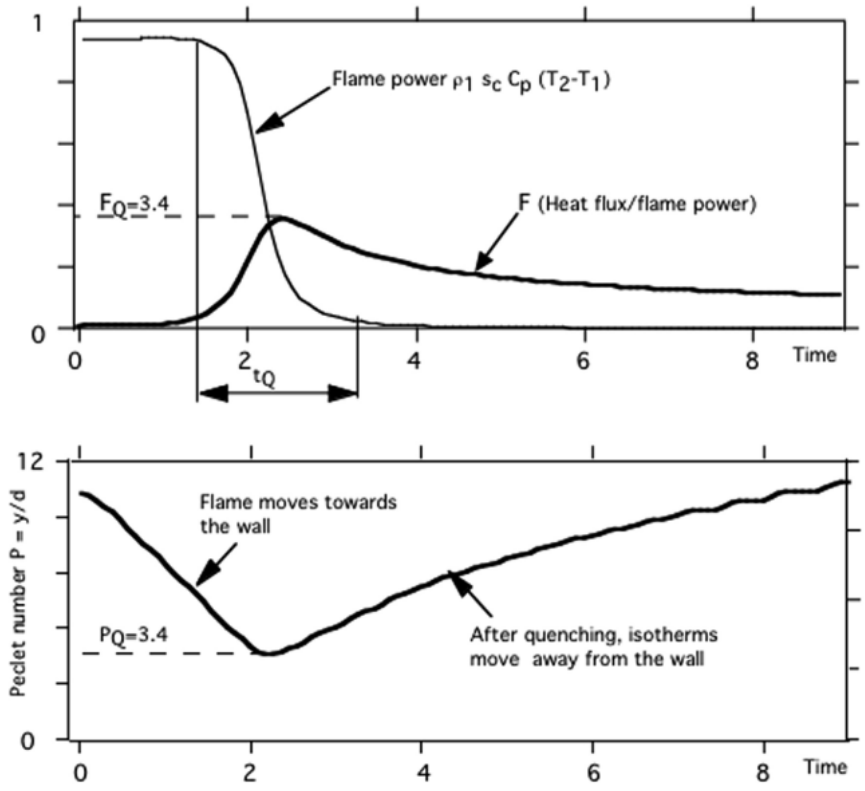

Figure 2.4 Different stages of HOQ as a function of normalized time t, divided into (1) flame approaching the wall (t <1.4); (2) flame undergoing quenching ($1.4 < t < 3.3$); (3) flame after quenching has taken place ($t > 3.3$). Taken from [7].

In the quenching zone which is attributed with low temperatures, radical-fuel reactions start to vanish. Instead, radical recombination reactions with low activation energies emerge and take control of the heat flux to the wall [27,62,66,68]. As a result, radicals are consumed and oxidation reactions are terminated. These phenomena change the flame structure drastically compared to the unquenched flame. In an unquenched flame, the peak concentration of intermediate hydrocarbons and radicals coincides with the flame region, whereas in a quenched flame, the peak concentration of radicals is located near the wall where the temperature gradient is at its maximum. It is noteworthy that these conclusions are only valid for inert walls and walls incorporating surface reactions do not fall into these conclusions.

Studies have also shown that single-step chemistry can predict the temperature field, Peclet number and heat fluxes to the wall with reasonable accuracy [38, 63]. However, detailed or skeletal chemistry must be employed to predict the gas composition in the post-quenching region [7].

Side-wall quenching

In a side-wall quenching scenario (SWQ) the flame propagates parallel to the wall. It can be a steady-state process for laminar flames. The flame stabilizes at a certain distance from the wall which is known as the quenching distance. SWQ is not studied as much as HOQ since it involves at least two dimensions, in contrast to HOQ which can be one-dimensional [69].

Figure 2.5 shows a typical experimental setup geometry for a laminar SWQ study (left) and the numerical domain (right) showing the simulated temperature from [8]. A cooled wall is placed on the left boundary of the domain to study FWI, and a rod is used to stabilize the flame. A V-shaped flame is consequently formed that undergoes SWQ at $z_q = 0$. Minimum Peclet numbers and maximum normalized wall heat flux in the SWQ are in the order of $Pe_Q \approx 7$ and $\dot{Q}_{N,Q} \approx 0.16$ respectively [63]. As a result, compared to HOQ, flames during SWQ are farther away from the wall and lose less heat.

In SWQ, locations of maximum heat release are followed by long sections of heat transfer from the hot combustion products to the cold wall. Locations with highest heat release near the walls are crucial for thermal fatigue failure and material design. Prolonged regions of heat release rate from combustion products to the combustor wall can affect the combustor life and requires optimized wall cooling techniques employed on the liner of the combustor [7].

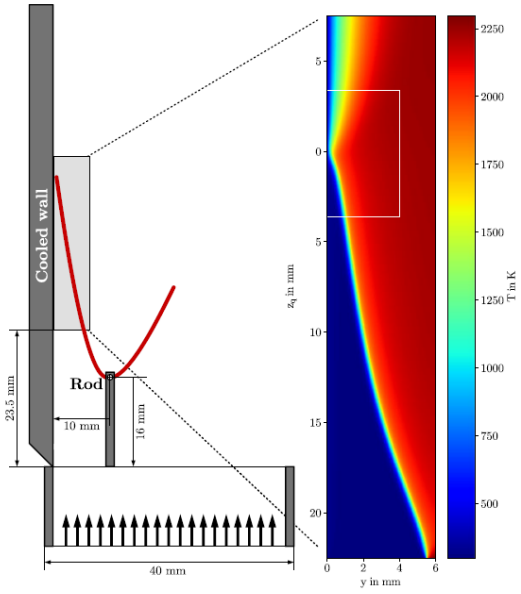

Figure 2.5 Illustration of the experimental setup for a laminar SWQ study (left) and the numerical result showing temperature contours (right). Taken from [8].

.

2.3.2 Turbulent FWI

The two configurations mentioned for laminar FWI can become more complicated in a turbulent flame regime. In a very recent study by Zentgraf et al. [9], it was shown that a turbulent flame undergoing FWI can incorporate both SWQ and HOQ like scenarios at different instances of time. They proposed a criterion based on the flame position upstream of the quenching point to distinguish HOQ and SWQ scenarios, and showed that quenching mechanism can oscillate between these two mechanisms in the matter of milliseconds. Figure 2.6 shows the sequences of FWI using OH planar laser induced fluorescent (PLIF) images. The first row shows a SWQ scenario. At $t_0 + 5ms$, HOQ mechanisms are observed because of the parallel flame region to the wall. At the same time a strong region of counterclockwise vortex is observed in region II which is pushing the flame towards the wall. It was observed in the direct numerical simulation of turbulent FWI using detailed chemistry as well that vortices play a crucial role in the flame dynamics in the near wall region [27]. They have shown that turbulent flames have lower quenching distance and higher heat flux to the wall, compared to the laminar flames due to the action of the vortices on the flame. They also confirmed that the radical recombination plays a major role in wall heat flux, accounting for 70% of total wall heat flux. They argued that vortices present in some regions of the domain push the flame front towards the wall, resulting in enhanced heat flux at some regions, or they may pull the flame further away from the wall resulting in decreased wall heat flux. They also observed local flame thickening near the wall, and also regime change from flamelet away from the wall to thicken flame in the near-wall region. This was observed also by Jainski et al. [70], in which they observed thinner boundary layer in the reactive channel flow compared to the non-reactive case. Higher fluctuations in the flow field parameters were also noted in the reactive channel flow compared to the adiabatic one. Kosaka et al. [71] also observed that the reaction zone shape changes dramatically in the near-wall region of a turbulent flame-wall interaction scenario compared to the laminar flames. All these studies show that turbulent flames deviate significantly from laminar flames in the near-wall region in a complex manner. This can have strong consequences on the models used in RANS and LES simulations.

High-fidelity DNS of more realistic scenarios closer to combustion engines have also been performed. Niemietz et al. [72] executed a DNS of a turbulent lean methane/air jet flame interacting with isothermal walls. The focus of this study was to investigate contributors to CO formation under gas turbine relevant conditions. They concluded that the main source of CO formation is governed by mean strain rate of the flow, FWI, and flame-recirculation zone interactions, and differs widely from the freely propagating flame. Jiang et al. [33]

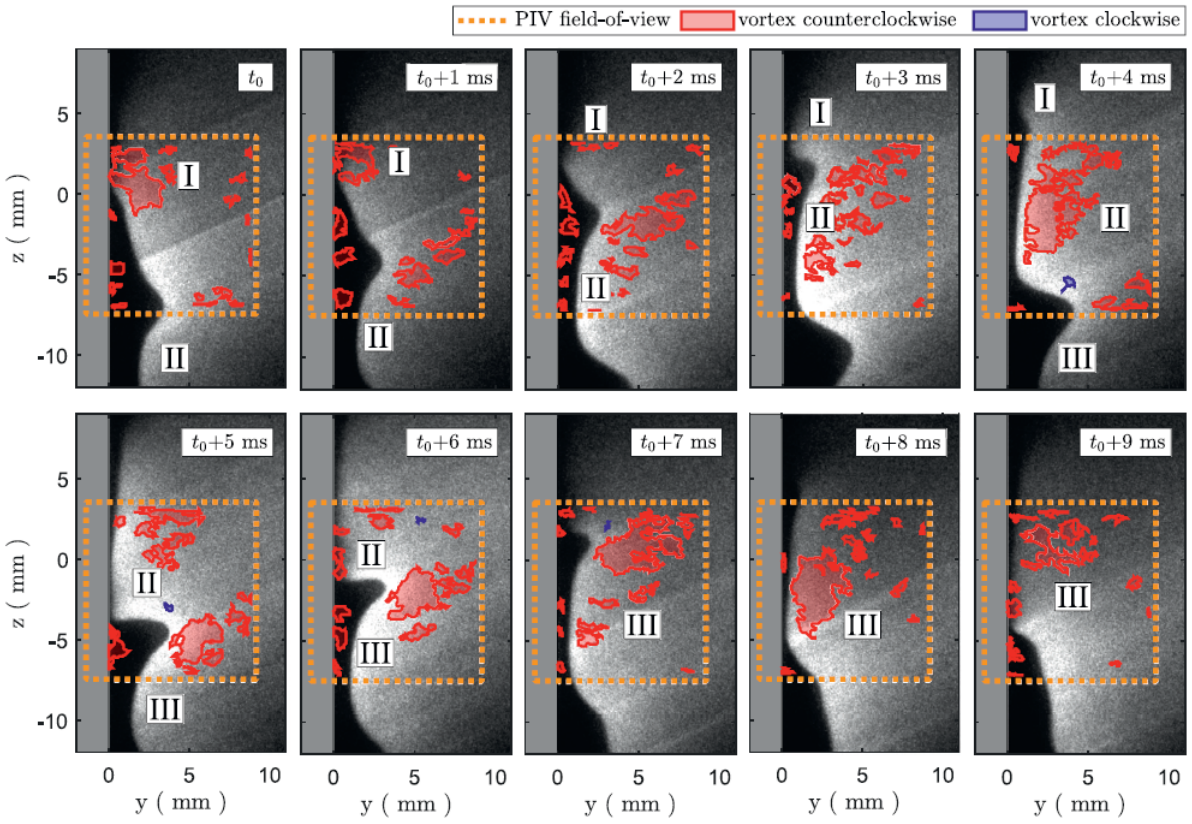

Figure 2.6 OH-PLIF images showing different stages of a transient turbulent flame quenching. Red and blue regions indicate vortex structures. The Roman numbers show consecutive approaching reaction zones. The wall is shown with a grey rectangle on the left-hand side. Taken from [9].

also performed a DNS study of methane/air turbulent V-shaped flames diluted by combustion products interacting with both cold and hot walls. Higher CO concentrations are also observed near the cold wall. Near the cold wall, flame interacted with the boundary layer all along the domain length, resulting in incomplete combustion near the wall and high CO concentrations. Whereas for the hot wall, the flame could touch the wall without quenching which results in more complete combustion and lower CO pollution.

Lai et al. [73] performed DNS study on side-wall quenching (SWQ) of V-shaped flames and head-on quenching (HOQ) scenarios for a turbulent premixed flame interacting with isothermal walls. A single-step irreversible chemistry was used to reduce computation costs. Wall heat flux statistics and flame topologies and their contributions to heat loss were analyzed. Eight flow topologies were extracted based on the three invariants of the velocity gradient tensor. It was revealed that for the HOQ configuration, heat losses are most dominated by nodal flow topologies (i.e., dominated by strain rate), whereas for the SWQ configuration, it

was mostly dominated by focal flow topologies (i.e., vorticity dominated). These differences result in discrepancies in terms of wall heat flux and quenching distances. The maximum wall heat flux was found to be larger in SWQ compared to the HOQ, contrary to the quenching distance which was found to be smaller in the SWQ configuration.

Wang et al. [74] performed DNS of inclined non-premixed methane flames impinging on a wall. Two branches of heat release rate were observed, one close to the wall, the other further away. They investigated two cases, with different Damköhler numbers, one twice the other. They observed more pronounced regions of extinction in the case with lower Da. Heat flux to the wall for the case with lower Da is also noticeably lower than the other case due to the extinction of the lower branch. It was also observed that the quenching distance and wall heat flux are negatively correlated.

LES simulations have also been performed at relatively high Re due to lower costs than DNS. Massey et al. [75] performed LES of lean swirl flames near blowout limit with isothermal boundary conditions on the walls. The modelling is a tabulated chemistry approach, based on unstrained premixed flamelets. They investigated the sensitivity of using different heat loss models in the combustion model, one using adiabatic and the other non-adiabatic formulations of the combustion models. Results are compared with experimental data and a previous simulation with adiabatic combustion model and adiabatic walls. It was revealed that axial velocity and mixture fraction are not affected by including heat loss in the combustion model. However, not including heat loss effects in the combustion model resulted in wrong prediction of the flame shaped, from V-shape in the experiments to M-shape in the adiabatic combustion model. It was also shown that using non-adiabatic combustion model results in a more dynamic flame. Agostinelli et al. [76] also performed an LES of a premixed methane-air swirl-stabilized GT combustor flame interacting with isothermal walls, and compared the results with the experiments. Their simulation showed good agreement with the experiments in terms of flow field velocity and temperature. The goal was to investigate the effect of wall heat transfer treatment in LES on the thermoacoustic response of the GT combustor. They used two approaches for wall heat transfer treatment, one using a simplified model based on the prescription of the thermal resistance tuned from the experiments, and the other based on full conjugate heat transfer simulation. They concluded that using precise boundary conditions on the wall on top of inflow and outflow is necessary for predicting the thermoacoustic behaviour of the combustion chamber.

In recent years, due to immediate need for transition to low-carbon fuels such as hydrogen in power generation and aeronautical sectors, there is a huge interest in these kinds of fuels. Swirl flames are usually utilized in these engines due to their higher combustion efficiency

and stability [16]. Fan et al. [10] performed a series of experiments on premixed methane/ hydrogen swirl flames impinging on a cooled inclined wall. They used simultaneous stereo-PIV and OH, CH2O PLIF to capture the flow and flame characteristics. They could reach mixtures as lean as 0.22 in equivalence ratio (defined as the actual air to fuel ratio over stochiometric one) and Karlovitz numbers as high as 1100 using pure hydrogen. These ultra-lean flames were only stable when the inclined wall was used. Three reasons were mentioned for such an observation. First, they argued that using the wall creates a low-velocity region due to the impingement which leads to better stabilization of the flame. Second, this could be due to the recirculation zone created near the wall which enhances mixing of the fresh mixtures with the products which finally leads to better stabilization. Third, this could be due to the semi-confinement which inhibits the penetration of the cold air from the surroundings. Figure 2.7 shows measured contours of OH concentration (left), CH2O concentration (middle), and their product, a proxy for heat release rate (right), for some of these flame. All cases feature constant Ka. Laminar flame speed is kept constant by changing the equivalence ratio for cases S1, S2, and S4, while hydrogen fraction is 0%, 30%, 70%, and 70% for cases S1, S2, S4, and K1 respectively. Case K1 has higher equivalence ratio than case S4, but also has higher bulk velocity to reach the same Ka. One interesting observation is that by increasing hydrogen fraction, the flame starts to move closer to the wall and penetrates the swirl region. This is because of the higher turbulent flame speed of hydrogen which allows the flame to propagate faster. Moreover, the flame front becomes more wrinkled because of thermodiffusive instabilities associated with hydrogen flames. Isolines of extinction strain rate are plotted on the formaldehyde concentration contours (middle). It is observed that the flame undergoes extinction as it reaches the isolines of extinction strain rate and leads to high amounts of formaldehyde which is an intermediate species. This large cloud of formaldehyde is significant and was not observed in previous studies. In a previous study on high Ka jet flame it was also observed that at high shear rates due to low residence time, species do not have enough time for complete combustion which resulted in depletion of intermediates [77].

Based on the papers on turbulent FWI mentioned here, flame structure and pollutant emission undergo complex, drastic changes in the near-wall region. However, literature still lacks detailed studies on wall effects on low-carbon swirl flames. None of the studies except for one experimental study [10] investigate this kind of flames. The motivation of this study is to generate a DNS of the aforementioned laboratory flame [10], which can give valuable insights since we will have access to all the flow and flame parameters of a realistic flame, contributing to the literature to a large degree. We will give a literature review on the DNS of laboratory flames in the next section.

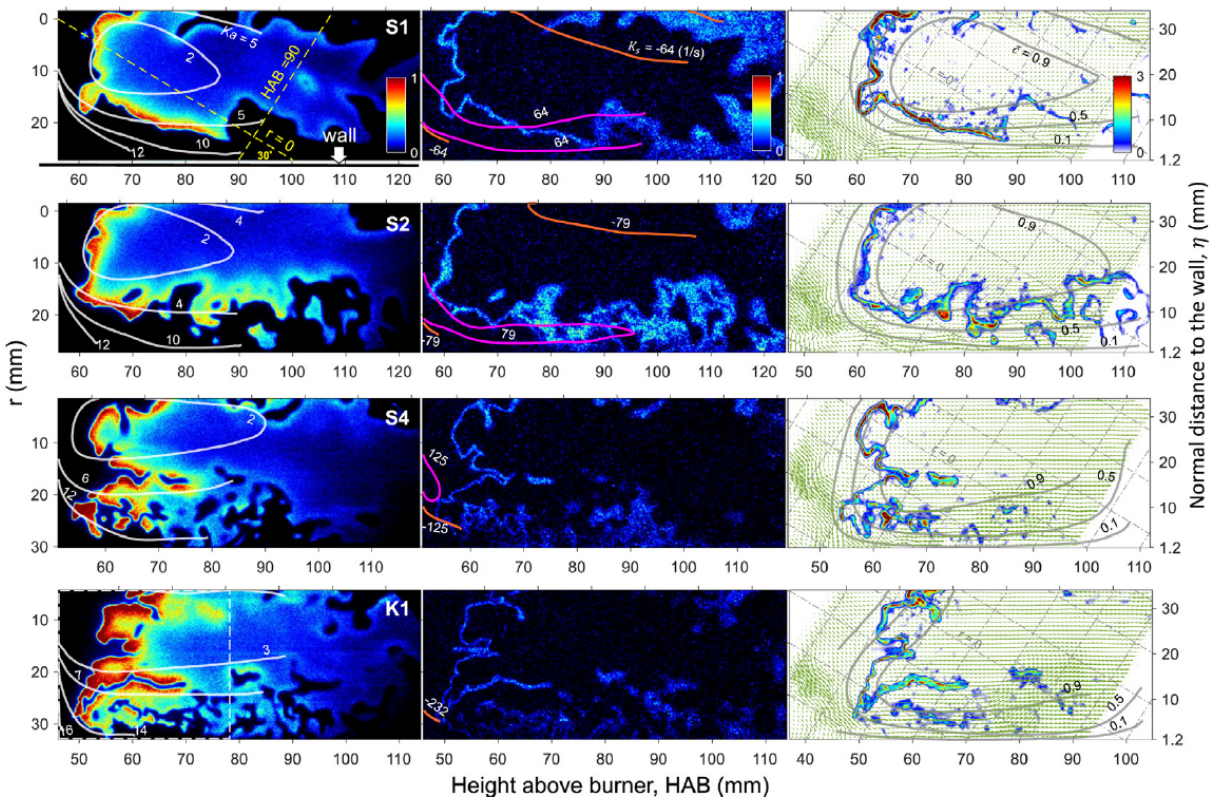

Figure 2.7 OH concentration (left), CH2O concentration (middle), and the velocity field superimposed by calculated HRR (right). Each row corresponds to a different hydrogen/methane mixture and equivalence ratio, but all at an almost constant unstrained laminar flame speed. The ticks on the left side of OH concentration denote distance to the nozzle center, and on the right side of the HRR denote the normal distance to the wall. Contours of Ka , mean in-plane laminar extinction strain rate, and progress variables are plotted on OH, CH2O, and HRR images, respectively [10].

2.4 DNS of laboratory turbulent flames

DNS of laboratory flames are aimed to complement the measurements obtained from the experiments and to access 3D time- and space-resolved data for all flow and (reactive) scalar fields unachievable with experiments.

Wang et al. conducted a DNS study on an experimental turbulent premixed methane-air jet-flame at high Karlovitz number [78–80] using detailed chemistry. Their DNS showed good agreement with the experiments in the 2D comparisons. The validity of the surrogates for heat release rate were examined using the DNS data and [CH2O][O] was found to be the best candidate for heat release rate measurements. Important results on flame surface area generation/destruction due to flow field features were also provided.

In a series of studies by Day et al., [41, 81], DNS of a lean, low-swirl, turbulent laboratory flame using methane and hydrogen flames were conducted. Comparisons of the flow field and flame characteristics from simulation and experiments were satisfactory, but still significant discrepancies were observed, in particular related to the flame stabilization location and mean flow field. To generate the inflow from the nozzle exit, they imposed measurements from the experiments including mean and turbulent fluctuations at the nozzle dump plane. In a LES study by Nogenmyr et al. [82], it was revealed that resolving the flow inside the injector using an auxiliary simulation and linking that to the reactive simulation leads to better agreement with the experiment.

Cheng et al. [83] performed a DNS study on a laboratory jet in a crossflow configuration. The goal was to understand the flame structure and stabilization mechanism for a lean ethylene-air jet flame. The jet Reynolds number was 6200. Overall, a good agreement was observed between the DNS and experiments.

Wang et al. [84] performed a DNS of a laboratory lifted jet flame and compared the results with the experiments. The results showed good agreement for the conditional means of reactive scalars. Analyses of the combustion mode also showed that the flame is diffusion stabilized at the base, and transitions to premixed mode further downstream. The flame was observed to stabilize at lean mixtures with low scalar dissipation rates.

In this project, numerical simulations of a laboratory turbulent flame interacting with a wall will be conducted which has not been done before. Major findings from the DNS and the experiments of the flame will potentially produce new data for low-carbon, high Ka swirl flames near the wall.

2.5 Critical analysis

Based on the detailed literature review presented in this section on the topic of turbulent FWI, it can be concluded that most of the DNS studies are either performed on canonical turbulent FWI configuration, such as HOQ [40,73,85,86], or V-shaped flames [9,27,33,71,87]. While being crucial for fundamental insights to the phenomenon of flame quenching and developing sub-grid models for LES and RANS, these studies do not investigate the actual flame-wall interactions taking place in real combustors, such as gas turbines which incorporate swirl flames. Although some studies have been performed on swirl flame interacting with walls using LES [75, 76], or experiments [10], no DNS study was found on the topic. DNS investigations can give invaluable insights to the phenomenon, not achievable through the means of LES or experimental techniques. This project can fill this knowledge gap. Moreover,

since the DNS is on a high Ka flame incorporating lean hydrogen-diluted flame, it can also contribute to the literature on the structure of highly turbulent low-carbon flames, which are raising interest in the community due to their potential use in transport and power generation sectors. On top of that, the target simulation is a laboratory flame, which can serve as a reference for other simulations in the future as well.

CHAPTER 3 METHODOLOGY

In this section, first, an overview of the code used to perform the numerical simulations is given. Next, a series of simulations are performed on a non-reactive swirl flow (NRSF) setup. This series of simulations are performed to find the inflow velocity profiles that generate a flow field that has the best match with the experimental results including three components of velocity average and rms at different heights above the burner. Two approaches have been considered which will be discussed. Next, we discuss the turbulent boundary layer (TBL) simulations. The aim is to investigate the required resolution to resolve the turbulent boundary layer formed on the swirl flame-wall interaction (SFWI) wall with the solver used. This series of simulations are performed on a non-reactive turbulent boundary layer representative of the SFWI simulation. Finally, preliminary results of the SFWI simulation are presented. In this thesis, DNS results are not presented, and only preliminary underresolved results are given. More details are given in the related section.

3.1 Governing equations

Consider the reactive Navier-Stokes equations in the low Mach number regime, in which the characteristics fluid velocity is small compared to the speed of sound and the effect of acoustic waves are removed. In this regime, the pressure is divided into two parts: a spatially constant thermodynamic pressure P_0 and a perturbational pressure π that drives the flow. In the low mach number regime, $P_0 >> \pi$.

The set of conservation equations specific to this flow is a system of PDEs with advection, diffusion, and reaction processes constrained to evolve on the manifold of a spatially constant thermodynamic pressure P_0:

$$\frac{\partial \rho}{\partial t} + \nabla . (\rho \mathbf{u}) = 0 \tag{3.1}$$

$$\frac{\partial (\rho \mathbf{u})}{\partial t} + \nabla . (\rho \mathbf{u}\mathbf{u} + \boldsymbol{\tau}) = -\nabla \pi \tag{3.2}$$

$$\frac{\partial (\rho Y_m)}{\partial t} + \nabla . (\rho Y_m \mathbf{u} + \mathbf{F_m}) = \rho \dot{\omega}_m \tag{3.3}$$

$$\frac{\partial(\rho h)}{\partial t} + \nabla.(\rho h\mathbf{u} + \mathbf{Q}) = 0 \tag{3.4}$$

where ρ is density, $\mathbf{u}$ is the flow velocity vector, h is mass-weighted enthalpy, T is temperature, and Y_m is mass fraction of species m, $\dot{\omega}_m$ is its chemical production rate, $\boldsymbol{\tau}$ is the viscous stress tensor, $\mathbf{Q}$ is heat flux, $\mathbf{F_m}$ is species diffusion flux. Body force due to gravity is ignored. These equations are supplemented by the equation of state which involves the thermodynamic pressure:

$$P_0 = \rho RT \sum_m \frac{Y_m}{W_m} \tag{3.5}$$

where R is the universal gas constant and W_m is the molecular weight of species m. Enthalpy (h) is calculated using:

$$h = \sum_m Y_m h_m(T) \tag{3.6}$$

in which h_m is the enthalpy of species m at the corresponding temperature T. The viscous stress tensor $\boldsymbol{\tau}$ is calculated using:

$$\tau_{i,j} = \frac{2}{3}\mu\delta_{i,j}\frac{\partial u_k}{\partial x_k} - \mu\left(\frac{\partial u_i}{\partial x_j} + \frac{\partial u_j}{\partial x_i}\right) \tag{3.7}$$

where μ is the shear viscosity. $\mathbf{Q}$ is calculated as:

$$\mathbf{Q} = \sum_m h_m \mathbf{F_m} - \lambda\nabla T \tag{3.8}$$

where λ is the thermal conductivity. Soret and Dufour effects are neglected. Plots comparing 1D laminar unstrained flames with various transport models are presented in Appendix A, showing negligible role of Soret and Dufour effects on the flame structure for the thermo-chemical conditions relevant to this work. Species diffusion fluxes, $\mathbf{F_m}$, with mixture-averaged assumption is calculated using:

$$\mathbf{F_m} = -\rho D_{m,mix}\frac{W_m}{W}\nabla X_m \tag{3.9}$$

where $D_{m,mix}$ is the mass diffusion coefficient of species m into the mixture, X_m is the mole fraction of species m, and W is the mixture-averaged molar weight. To impose the low-Mach

assumption, we set the thermodynamic pressure constant by:

$$\frac{DP_0}{Dt} = 0 \tag{3.10}$$

Using the equation of state, chain rule and the continuity equation one can obtain:

$$\nabla.\mathbf{u} = \frac{1}{T}\frac{DT}{Dt} + W\sum_m \frac{1}{W_m}\frac{DY_m}{Dt} \tag{3.11}$$

This divergence constraint is imposed on the velocity field to take into account the low-Mach assumption.

To obtain chemical reaction source term:

$$\dot{\omega}_m = \sum_{j=1}^{M_r} \nu_{m,j} R_j \tag{3.12}$$

in which M_r is the number of elementary reaction steps and:

$$\nu_{m,j} = \nu''_{m,j} - \nu'_{m,j} \tag{3.13}$$

where ${\nu_{m,j}}'$ and ${\nu_{m,j}}''$ are the stochiometric coefficients on the reactant and product sides of reaction j respectively. The rate of reaction, R_j, is expressed as:

$$R_j = k_{f,j}\prod_{m=1}^{N_s}[X_m]^{\nu'_{m,j}} - k_{r,j}\prod_{m=1}^{N_s}[X_m]^{\nu''_{m,j}} \tag{3.14}$$

where $[X_m]$ is the molar concentration of species m, N_s is the number of species and k_f is the forward reaction rate coefficient and is calculated as:

$$k_f = AT^{\beta} exp\left(\frac{-E_a}{RT}\right) \tag{3.15}$$

in which A is the pre-exponential factor, β is the temperature exponent and E_a is the activation energy. The reverse reaction rate coefficient is expressed as:

$$k_{r,j} = \frac{k_{f,j}}{K_{c,j}(T)} \tag{3.16}$$

in which $K_{c,j}$ is the equilibrium constant for reaction j:

$$K_{c,j} = K_{p,j} \left(\frac{P_0}{RT} \right)^{\sum_{k=1}^{N_s} \nu_{k,j}} \tag{3.17}$$

with:

$$K_{p,j} = exp \left(\frac{\Delta {S_j}^0}{R} - \frac{\Delta {H_j}^0}{RT} \right) \tag{3.18}$$

${\Delta H_j}^0$ and ${\Delta S_j}^0$ are changes in enthalpy and entropy of the reaction j in standard states.

3.2 Numerical solver

3.2.1 General code description

The set of equations presented in the previous section are solved numerically using the solver PeleLMeX [11], an adaptive-mesh low Mach number code for reacting flows. The adaptive implementation is based on a block-structured adaptive mesh refinement (AMR) strategy. In this approach, regions to be refined, which are defined by the user based on arbitrary criteria such as heat release rate or species mass fraction, are organized into rectangular patches. Each AMR level has twice the spatial resolution in each direction than the lower level. Adaptive refinement is performed both in time and in space. Compared to a uniform fine grid, using AMR reduces computational costs by an order of magnitude [41] in case the region with highest required resolution represents a small fraction of the total domain. PeleLMeX is a finite-volume code. For time-stepping, it makes use of spectral deferred corrections (SDC) to incorporate a split-type iterative approach [88]. Conservation of mass, energy, and species are subject to a constrained velocity field. Advection and diffusion terms are treated using explicit Godunov and semi-implicit Crank-Nicolson methods, respectively. A temporal splitting approach is used for the equations related to the conservation of species. Overall time step size is constrained by the fluid velocity using advective Courant–Friedrichs–Lewy (CFL) constraint, instead of the acoustic wave speed. This increases the time step size by a factor of around 10 compared to the compressible flow equations. The overall scheme has shown to be second order accurate in space and time [42]. PeleLMeX supports embedded boundary to represent complex geometries and it is parallelized with MPI + OpenMP for CPUs [41, 89].

3.2.2 Code algorithm

In PeleLMeX, all state variables including $\mathbf{u}$, ρ, T, Y_m, h_m are cell-centered, except for π which is defined on the cell nodes. PeleLMeX uses a second-order projection method to solve the momentum equation [90]. Using this equation, velocity is integrated in time and projected to impose the divergence constraint shown in equation 3.11. For reactive flows, the scalar thermodynamic advance is performed between these two steps (step 2) within the SDC context. The PeleLMeX time advance algorithm, which is fully described in [11], is summarized here:

1. Predict a time-centred velocity (U^{ADV^*}) at the cell faces using the cell centered data at t^n and a time-lagged pressure gradient ($\nabla\pi^{n-1/2}$) using a second-order Gudonov procedure. To enforce the divergence constraint (equation 3.11), a discrete projection scheme is applied to this velocity field. This field (U^{ADV}) is the advection velocity used for computing the advective fluxes.

2. Use spectral deferred correction (SDC) approach [88] to integrate over the time step. This gives the time advanced species mass fractions and enthalpy.

3. Using an explicit advection term and a Crank-Nicolson implicit scheme for the diffusion term, compute an intermediate cell-centered velocity field (U^{n+1^*}). A Nodal-projection scheme is applied to this provisional velocity field (U^{n+1^*}) to satisfy the divergence constraint, and the new velocity field (U^{n+1}) and pressure at $t^{n+1/2}$ are thus obtained.

Figure 3.1 shows a flowchart of the time advance algorithm used in PeleLMeX [11] with some more details. For a more detailed description of the algorithm the reader is referred to [90–92].

3.3 Configurations

3.3.1 Non-reactive swirl flow

As mentioned in the introduction section, this project aims at performing simulations on a laboratory flame. Here, we first elaborate on the burner setup.

Figure 3.2 shows a schematic of the low-swirl injector setup [12]. Flow field upstream of the swirler exit plane is divided into two main regions: one is the core flow which is a pipe flow, and the other is the outer swirler. The flow first goes through an expanding section to reduce the velocity. Then, it goes through a mesh screen and a honeycomb to increase the unirformity of the flow. A 3D printed plenum is used to converge the flow. Next, it goes through a turbulence generator and then the injector nozzle. The injector comprises of

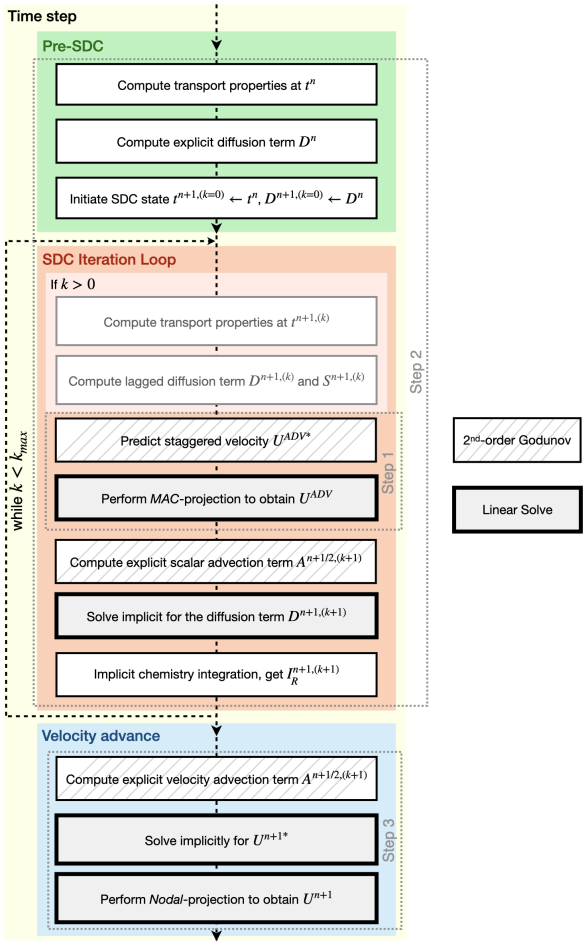

Figure 3.1 Flowchart of the time advance algorithm used in PeleLMeX. Taken from [11].

a central channel which has a diameter of 20.2 mm. This channel is shrouded by a swirler which has an outer diameter of 32.4 mm. The vanes of the swirler have 40° angle with the nozzle centerline, and the swirl number is 0.47. The tip of the injection nozzle is located 46.0 mm upstream of the burner exit nozzle which has a 32.0 mm diameter.

To evaluate the flow field created by the swirler, a series of simulations were executed in a non-reactive environment. As mentioned in the beginning of Chapter 3, the aim of this series of simulations is to find the best inflow that generates a flow field that best matches the experiments. The simulation domain is a box which has a length 5 times the diameter of the swirler and is shown in Figure 3.3. The temperature and pressure of the domain is atmospheric, i.e., 300K and 1 atm. Grid count in each direction at the base level (level zero AMR) is 128. Although three levels of AMR is needed to resolve the Kolmogorov length scale, one level of AMR was shown to be enough to capture the flow field characteristics after comparing the results with one and two levels of AMR. Statistics for the axial, azimuthal

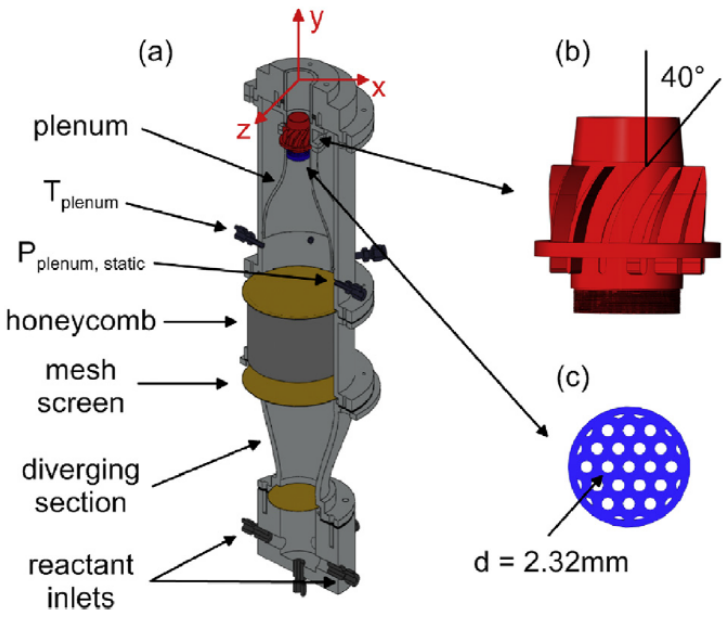

Figure 3.2 Drawings of (a) the low-swirl injector, (b) the low-swirl injection nozzle, and (c) the turbulence generator. Taken from [12].

and radial velocity average and rms at six different heights above the burner are shown in Appendix B. D is the diameter of the burner exit. The data extraction plane goes through the center of the nozzle. Excellent agreement is observed for all three velocity components. The simulations were run for more than 5 flow through times.

Two approaches have been considered to generate the inflow which are discussed here.

First approach: convected homogeneous isotropic turbulence

In the first approach, inflow velocity including mean and rms of the three components of velocity are the same as the measurements at the nozzle exit in the experiments. To impose turbulent fluctuations to the mean flow, a three-dimensional homogeneous isotropic turbulence (HIT) box is introduced at the inlet. This HIT box, including positions and three-component velocity fluctuations, is created and stored in a file. Based on the mean velocity of the flow and assuming Taylor's hypothesis, the position of the sampling plane in the HIT box is calculated in space, and velocity fluctuations are read from the file. To impose the velocity rms curve measured from the experiments to the simulation, a curve-fitting approach has been used. The fitted curve is obtained using a 10-degree polynomial. This curve is finally multiplied to the velocity fluctuations which have an rms of unity, and is added to the mean flow.

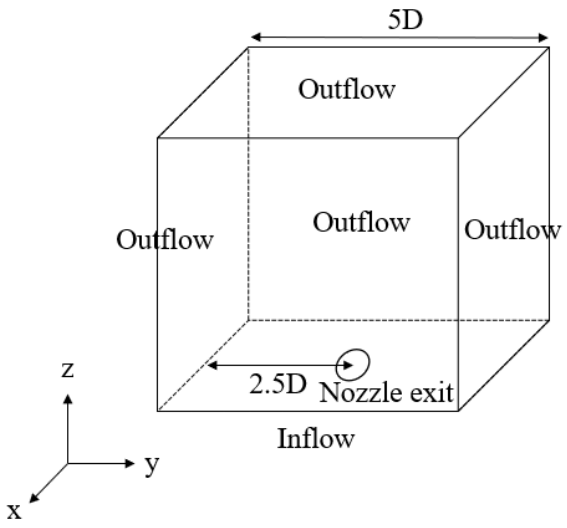

Figure 3.3 Computational domain for NRSF simulations

Figures 3.4a and 3.4b show the radial dependency of axial velocity average and rms from the experiments (blue curves) and the curve fitting (yellow curves) which are imposed in the simulation. The same is done for other velocity components. A coflow velocity, U_c, was also used outside the nozzle exit. There is uncertainty regarding the magnitude of coflow velocity, which is dependant on the power of the fan used in the experiments to flush out the products. Based on the distance of the nozzle dump to the fan and the power used during the experiments, coflow velocity is estimated to vary somewhere between 0.2 m/s to 2 m/s. Precise measurements will be conducted in the near future.

Figure 3.5 shows the axial integral length scale from the experiment near the nozzle exit as a function of radial distance from the nozzle center. Higher values are observed near the center compared to the edge of the nozzle. Figure 3.6 shows the generated velocity fluctuations in the HIT box based on the turbulent kinetic energy spectrum proposed by Passot-Pouquet [93] in $x-y$ and $x-z$ planes. The black lines show the location of the central jet edge which is shrouded by the swirler in the outer region.

The tested configurations are listed in Table 3.1. Two fields with different length scales merged for the inner and outer regions for cases Inflow-1.1 and Inflow-1.3 to match, to some limited extent, the radial dependency measured in the experiments.

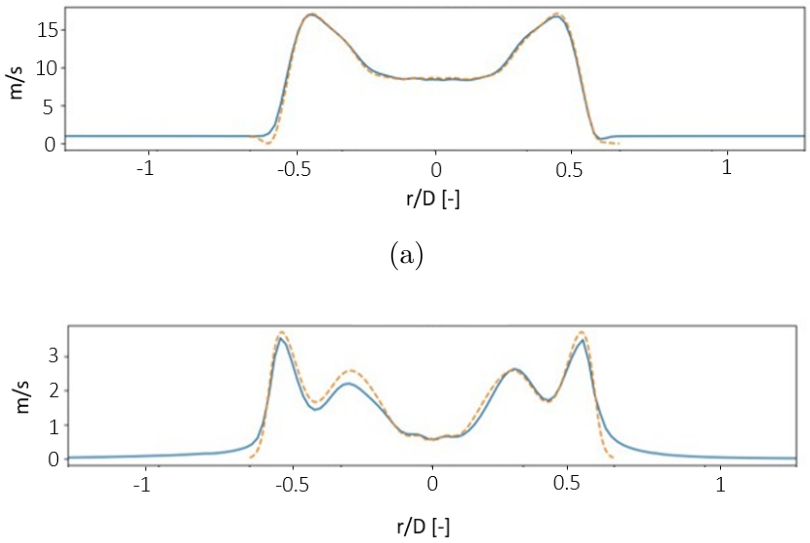

(a)

(b)

Figure 3.4 Radial dependency of the axial velocity average (a) and rms (b) at the burner exit obtained from PIV measurements (courtesy of Luming Fan), and the curved fit (yellow line)

Table 3.1 Inner and outer integral length scales (l_0) for the composite convected HIT inflow generation cases

Inflow generated	Inner l_0	Outer l_0
Inflow-1.1	$D/2$	$D/4$
Inflow-1.2	$D/3$	$D/3$
Inflow-1.3	$D/4$	$D/8$

Second approach: large-eddy simulation of the flow inside the injector

A large eddy simulation of the injector was carried out using the commercial code-Simcenter STARCCM+. This LES simulation was done by a collaborator, Sandeep Jella from Siemens Energy Canada, and was not part of the work performed by the author. The computational domain included the complete injector which comprises of the swirler and the perforated plate. Mass flow inlet conditions were used for the flow and the central jet with a relevant flow split imposed for each. Synthetic turbulence at each inlet was imposed using the method of Jarrin et al [94]. This was needed to ensure that the turbulent jets from the perforated plate correctly developed. A polyhedral mesh was used with a 0.2 mm cell characteristic length throughout the injector section as seen in Figure 3.7 (left) along with vorticity contour in the middle. A detailed sketch of the injector is also shown on the right. A finer mesh

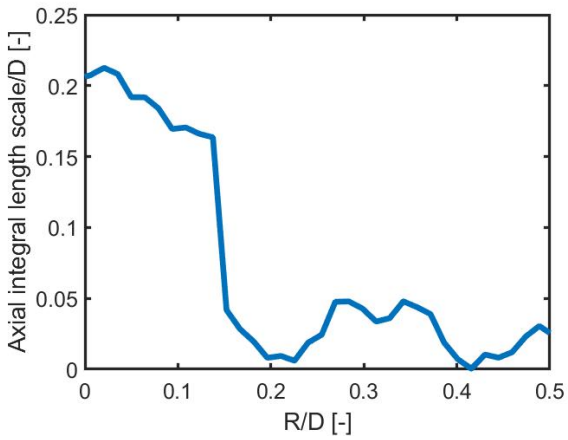

Figure 3.5 Radial dependency of the axial integral length scale at the burner exit obtained from PIV measurements, courtesy of Luming Fan

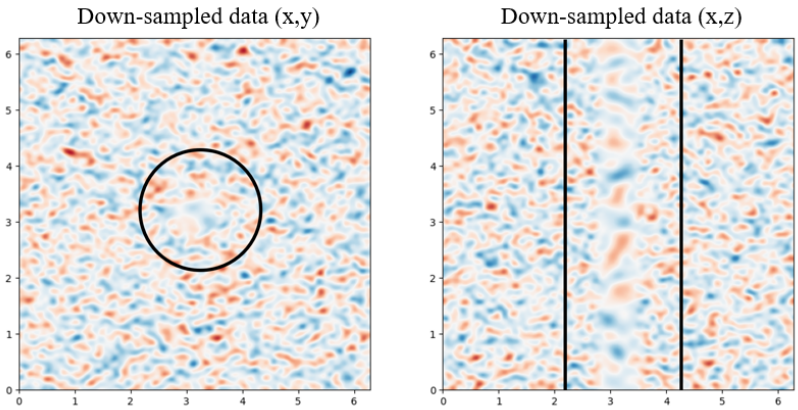

Figure 3.6 Generated velocity fluctuations in the HIT box in $x-y$ and $x-z$ planes merging two different length scales. The black lines show the location of the edge of the injector.

sizing has been used near regions of high curvature, e.g., swirler vane trailing edges and the splitter dividing the jet into the annular swirl stream and the central (non-swirl) jet. The mesh size was increased to 0.5 mm in the flame zone to a maximum of 2 mm in the farfield. The filtered form of the continuity, momentum and energy equations were solved using the mesh as a local filter. The Wall Adapting Local Eddy Viscosity (WALE) model of Nicoud et al [95] was used to model sub-grid stresses and to alleviate mesh requirements near the wall. The overall mesh size was approximately 21 million cells and was run on 800 CPUs on the Niagara supercomputer.

With respect to numerics, the transient terms were calculated using a 3 level, implicit time-stepping scheme based on a backward differentiation. Spatial discretisation for the convective

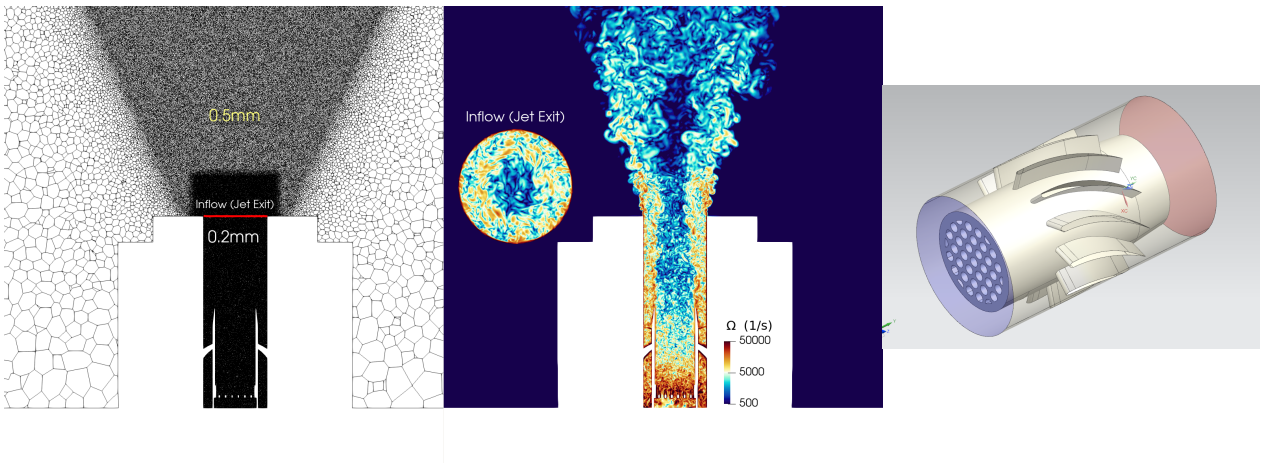

Figure 3.7 Mesh geometry in the large eddy simulation of the flow inside the injector (left), vorticity magnitude contour (middle), and injector geometry (right)

term was carried out using a hybrid third order MUSCL-based central differencing/upwinding scheme. A boundedness criterion based on a locally calculated normalized variable diagram value ensured flux oscillations were avoided. The diffusion terms were calculated using a pure second-order central differencing scheme; secondary gradients were evaluated to ensure cross-diffusion contributions to the diffusion flux resulting from non-orthogonal meshes was accounted for. Gradient evaluations for all variables utilized the method of least squares. Finally, flow and scalar equations were advanced in a segregated manner with the SIMPLE-Consistent (SIMPLEC) scheme used for pressure-velocity coupling.

A time-series of the velocity field extracted at the injector exit is used as the inflow velocity field for the DNS (Inflow-2).

3.3.2 Turbulent boundary layer

In order to resolve the viscous sublayer in the turbulent boundary layer, recent DNS studies of turbulent FWI suggest using at least one grid point within one wall unit [27,33], which is defined as:

$$y^* = \frac{\nu}{u_\tau} \tag{3.19}$$

where:

$$u_\tau = \sqrt{\frac{< \tau_w >}{\rho}} \tag{3.20}$$

and ν and $< \tau_w >$ are fluid kinematic viscosity and mean shear stress, respectively.

Recent studies use this criterion to resolve turbulent boundary layer in their DNS [33, 72, 74]. However, this claim was not comprehensively studied and can be dependent on the configuration. It is also, to some extent, solver dependent. In this series of simulations, we aim to assess the required resolution in the viscous sublayer of a turbulent boundary layer representative of the SFWI simulation, using the same solver (PeleLMeX). In particular, the wall is specified as an embedded boundary (EB), similar to the SFWI case. The EB feature in PeleLMeX is recent and has not previously been validated in turbulent boundary layers.

The simulation domain is shown in Figure 3.8. Inlet is on the left, and no-slip isothermal wall is at the bottom. The wall is incorporated using EBs, and is located one cell away from the domain edge, slightly (0.001% of base grid size) inside the second cell. Periodic boundary conditions are on the spanwise direction, outflow on the top and right faces. Laminar profiles from the Blasius solution are imposed at the inlet both for velocity and temperature. Turbulent Reynolds number based on the boundary layer momentum thickness at the inlet is $Re_{\theta,0} = 175$. Temperature of the flow and wall are chosen to resemble the SFWI simulation, which are 800 and 330 K respectively. Three simulations are performed each with a different maximum AMR level on the first ten layers off the wall. More specifications of the simulations are shown in Table 3.2, where wall normal distance is normalized as

$$y^+ = \frac{y}{y^*} \tag{3.21}$$

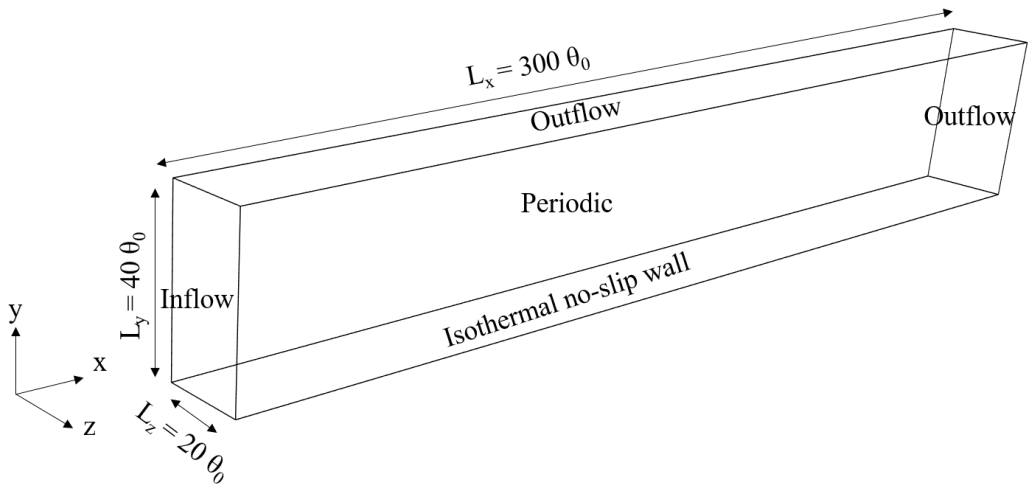

Figure 3.8 Sketch of the 3D domain for TBL simulations

Table 3.2 Specifications of the configurations for TBL simulations

Simulation index	Maximum AMR level on the wall	Number of cells [millions]	Total Cost [$*10^3 CPU hours$]	Maximum y^+ for the first cell
TBL0	0	33	40	2.6
TBL1	1	59	100	1.4
TBL2	2	184	400	0.72

The computational box has a dimension of $300\theta_0$, $40\theta_0$, $20\theta_0$ in the streamwise, wall-normal, and spanwise directions, respectively. θ_0 is the boundary layer momentum thickness at the inlet. There are 1560, 208, and 104 grids at the base level in the streamwise, wall-normal, and spanwise directions, respectively. The simulation setup is very similar to the study by Kong et al. [96], where they performed DNS of turbulent thermal boundary layer developing on isothermal and isoflux walls. In order to trigger laminar to turbulent transition of the boundary layer, velocity fluctuations have been added at the inlet to the mean flow. Fluctuations are obtained from a homogeneous isotropic turbulence box. The HIT box is added to the inlet periodically as suggested by previous studies on turbulent boundary layers [97, 98]. The HIT box is cubic and has a length equal to the width of the domain, i.e. $20\theta_0$. The integral length scale of the fluctuations is one fourth of the HIT box length and the ratio of rms of velocity fluctuations to bulk inlet velocity is $u'_0/U_\infty = 0.1$.

The simulations were run for more than 5 flow through times for each case, and then sampling was started. At each axial location, the statistics are averaged over time (more than 200 snapshots were captured for each case through 10 flow through times), spanwise direction (across all cells in the spanwise direction), and axial direction (averaged on cells over $15\theta_0$ distance).

3.3.3 Turbulent swirl flame-wall interaction

In this section, we first introduce the experimental setup utilized to perform the investigations on the experimental laboratory flame. We are considering an experimental case studied in [10], which was performed by a post-doc in the group. Then, we discuss the numerical setup developed to replicate the experimental flame in our DNS.

Experimental setup

A schematic of the experimental setup is shown in Figure 3.9. It incorporates a model low-swirl gas turbine burner, and a water-cooled plate with the dimensions of 60×40 cm^2. For

velocity and species concentration measurements, simultaneous stereo-PIV and OH×CH2O PLIF diagnostics are used. The burner is the one described in Section 3.3.1. The flame is impinging onto a flat plate with an angle of 30 degrees relative to the burner axis. The horizontal distance between the nozzle center and the plate is $L = 2D$ (64 mm). In this configuration, the lifted flame could interact with the plate sufficiently. A group of thermocouples were used to measure the temperature of the plate. It was shown that the surface temperature of the plate was stable around 330 K and uniform within 8 K. More details on the burner can be found in [10, 12].

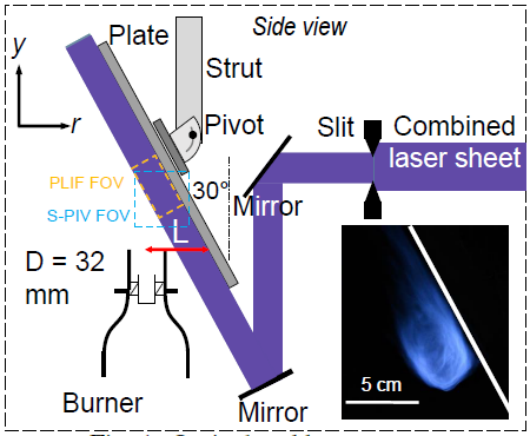

Figure 3.9 Optical and burner setup for the experiments

Numerical setup

The setup for the SFWI simulation is shown in Figure 3.10. The inclined wall is incorporated using the embedded boundary capability of the code. The bottom of the domain is the inflow where premixed air/fuel mixture enters the domain from the injector shown by the blue circle. The inflow is prescribed using the second approach (using LES data) discussed in Section 3.3.1 in that it produces better match with the experiments compared to the other approach. An air coflow with velocity U_c was prescribed for the outer-burner region to mimic the flow field in the experiments as much as possible. Other parameters for this simulation are listed in Table 3.3. η is estimated using Eq. 2.3. Velocity fluctuations rms, u_0', were measured in the experiments using stereo-PIV in the swirl region. Turbulent Reynolds number, Re_t, is estimated using $u_0' l_0/\nu$. More simulations with different equivalence ratios, hydrogen fractions, and wall boundary condition (adiabatic wall) will be performed in the future. The temperature of the wall is fixed at 330K, same as in the experiment. Laminar flame speed and thickness were calculated using Cantera [99] with the Aramco mechanism [100]. Combustion products of the corresponding mixture at the inflow are imposed at $t = 0$ near the nozzle exit to ignite

the incoming fuel/air mixture. At the base level (AMR level 0), there are 256 grids in each direction. The simulation was first run using only 1 level of AMR for two flow through times until the flame stabilized. A second level of AMR was then added, and multiple scoping runs testing different equivalence ratios, coflow velocity, and inlet velocity profiles were performed, summing around 8 flow through times. Then, the final configuration mentioned earlier was run for around four flow through times with level 2.

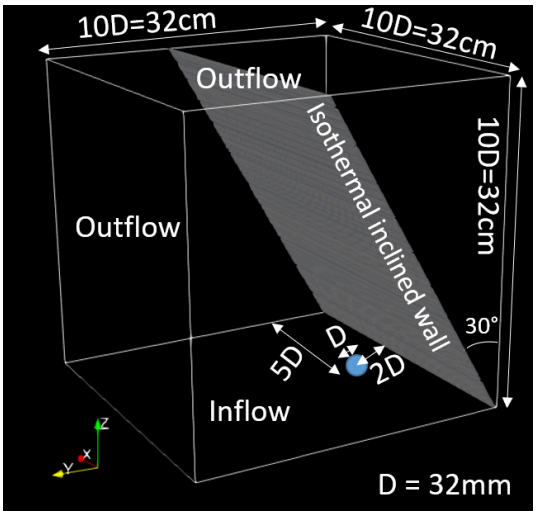

Figure 3.10 Three-dimensional domain for the numerical simulations

A 24-species, 105 reactions chemical kinetics mechanism derived from the Aramco detailed mechanism, developed for lean methane-hydrogen mixtures is utilized in the simulation [100].

Table 3.3 Specifications for the SFWI configuration

U_b[m/s]	ϕ	H_2:CH_4	l_f[mm]	S_l[cm/s]	u'_0[m/s]	l_0[mm]	η[μm]	Ka	Re_t
10	0.41	0.7:0.3	2.1	4.6	2.3	2.8	32	200	400

Table 3.4 shows the required resolution and corresponding AMR level to resolve the Kolmogorov length scale, wall unit, and flame thickness. The AMR strategy is based on refining the mentioned regions up to the required resolution. To that end, the software gets the relevant variables as the input to refine regions with: mass fractions of O and H higher than 1.0×10^{-4} and 1.0×10^{-5} respectively to resolve the flame front up to level 4, vorticity magnitude higher than 2.0×10^3 s^{-1} to resolve the Kolmogorov length scale up to level 4 [89], and also a criterion to resolve regions with temperature difference of adjacent cells higher than 200 K up to level 2 to avoid high gradients in the domain [89]. AMR level 4 is also used

all throughout the wall to resolve the viscous sublayer. As mentioned before, in this thesis simulations are performed only up to level 2, and simulations with level 4 were only tested for a few steps for cost estimate. Figure 3.11 shows the AMR levels around the flame front superimposed on the O mass fraction and vorticity magnitude fields using maximum AMR level 2. The white line represents the edge of the inclined wall.

Table 3.5 quantifies the cost of the SFWI simulation using each AMR level. To estimate the cost, the simulation was run for a few time steps at each level. Based on the physical time step size and the CPU hour cost for each step, the total computation cost for each level for one flow through time was estimated.

Table 3.4 Relevant length scales to be resolved for DNS resolution

Length scale	Required resolution [μm]	Required AMR level
Turbulence ($dx = 2\eta$)	110	4
Wall unit ($y^+ = 1$)	66	5[1]
Flame thickness (10 pts/species layer)	80	4

Table 3.5 Cost estimate of the SFWI simulation using each AMR level

Maximum AMR level	Grid spacing [μm]	Number of cells [millions]	Total cost per flow through [Million CPU-hours]
0	1,250	17	-
1	625	60	-
2	312.5	240	0.1
3	156.2	460	1.3
4	78.1	2,300	11.2

Figure 3.12a shows the calculated averaged y^* values vs. height above burner (HAB) in the middle plane along the x-axis. The blue line is the raw data calculated from the simulation. Since the way y^* was calculated resulted in noisy data, filter was applied. The horizontal dashed red, blue, green, and purple lines show the average distance between the first cell center and the wall ($\Delta x/2$) using AMR level 1, 2, 3, and 4. As will be discussed in Section 4.2, using y^+ up to 1.4 for the first grid point next to the wall can be deemed sufficient to

[1]Please refer to the discussion below Table 3.5 for more details.

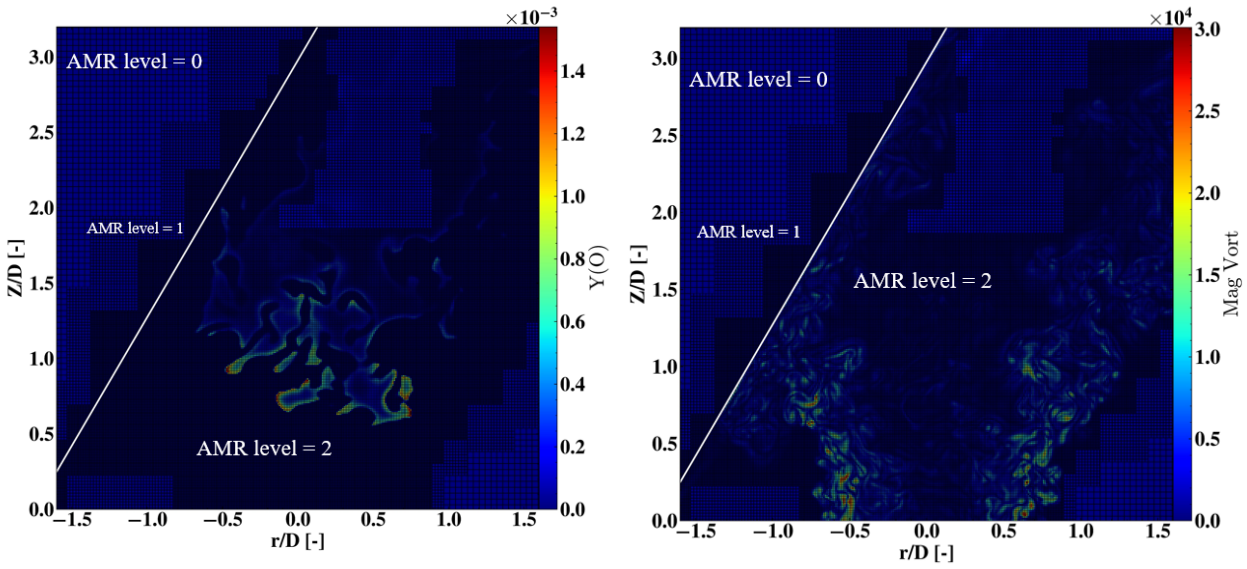

(a) (b)

Figure 3.11 Grid edges around the flame front for the present study superimposed on the O mass fraction field (left) and vorticity magnitude (right). The white line represents the edge of the inclined wall.

resolve a turbulent boundary layer with DNS accuracy with the present solver, including the use of EB. This means that using AMR level 4 on the wall can resolve y^* values as low as $39\mu m/1.4 = 28\ \mu m$. The implication of this is that using AMR level 4 is enough to resolve all the boundary layer on the wall. Figure 3.12b shows the y^* values as a 2D contour on the wall. The closed curve on the plots show isocontours of $y^* = 39\mu m$, which corresponds to $y^+ = 1$. The minimum y^* in the whole domain is $33\mu m$ which is around $y^+ = 1.2$.

Figure 3.13 presents the time evolution of instantaneous and mean heat release rate, integrated in the mid-plan along the x-axis. The equivalence ratio has changed from 0.39 (a test case) to 0.41 (present configuration) at the initial point in the instantaneous curve which results in gradual increase of HRR. Averaging (orange curve) starts once the flame seems to reach steady state. Averaged values (shown using the orange line) show fluctuations less than 5%, suggesting that a statistically steady state has been reached.

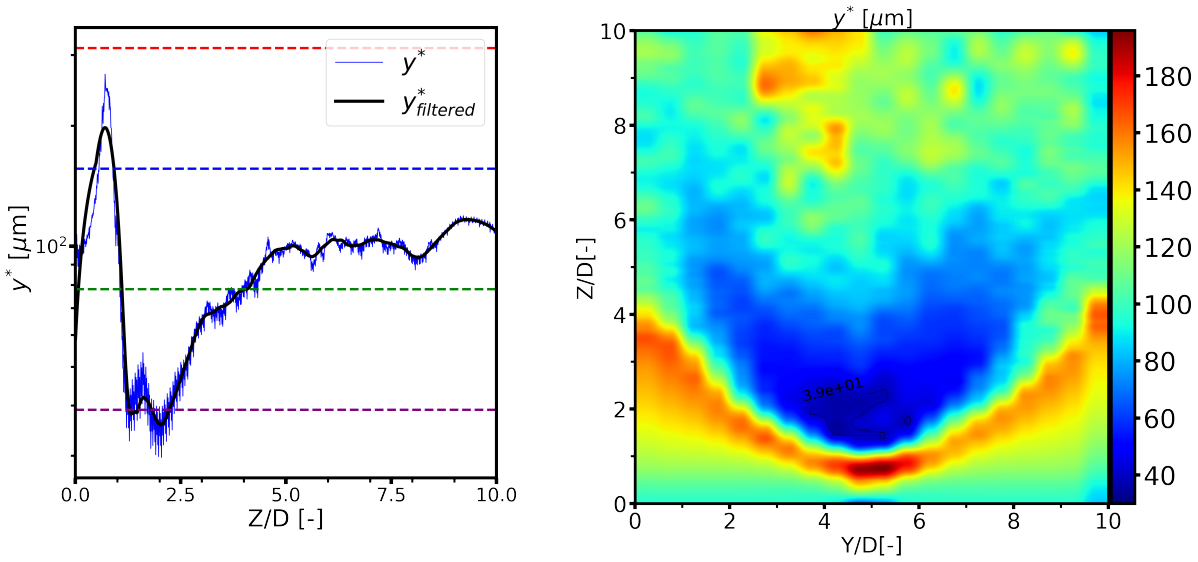

(a) (b)

Figure 3.12 y^* values vs. height above burner (HAB) in the middle plane along the x-axis (left) and y^* values as a 2D contour on the wall (right)

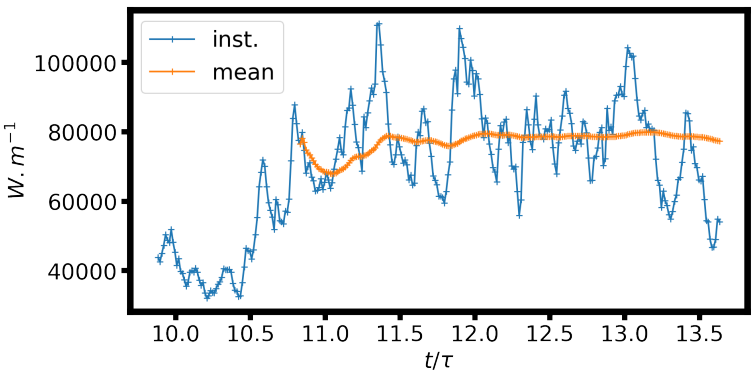

Figure 3.13 Time evolution of the integrated heat release rate in the mid-plane along the x-axis

CHAPTER 4 RESULTS

In this chapter we present the results obtained from the simulations mentioned in the previous chapter. They can be categorized into non-reactive swirl flow, turbulent boundary layer, and turbulent swirl flame-wall interaction.

4.1 Non-reactive swirl flow

As mentioned in the methodology section, the NRSF simulations were run using one level of AMR. Figures 4.1, 4.2 and 4.3 show the instantaneous, averaged and rms flow fields for the simulation Inflow-2 mentioned in Section 3.3.1. Statistics for axial velocity, radial velocity, azimuthal velocity, and vorticity magnitude are shown in the figures. The main characteristics of a swirl flow can be interpreted from these figures. A diverging flow is created downstream due to the outward radial velocity. A low velocity region is formed near the centerline starting around $Z = 1.5D$. This low-velocity region is created by the centrifugal pressure gradient and plays a pivotal role on flame stabilization at high inlet velocities [17]. It enables the hot combustion products rife with radicals to interact with fresh gas and ignite them. Average axial velocity also demonstrates that a strong shear flow is created between the swirl flow and the core flow. rms flow field also shows that velocity fluctuations are highest in the outer flow region compared to the central flow, which simply means those regions incorporate higher gradients. The fluctuations decay as the flow evolves downstream.

Figures 4.4 -4.9 are depicted here to make a comparison between simulations mentioned in Section 3.3.1 and the measurements in the experiment. Coflow velocity $U_c = 0.2$ m/s has been used. Both average and rms values of the three-component velocity are shown at six different heights above the burner. Simulations Inflow-1.1-3 in Figure 4.4 show much lower average axial velocity near the centerline at distances away from the inlet compared to the experiments. However, simulation Inflow-2 (the one using LES of the injector as in the inflow) shows good agreement with experiments. This discrepancy observed in Inflow-1.1-3 can have major consequences on the flame position and stabilization in a reactive environment.

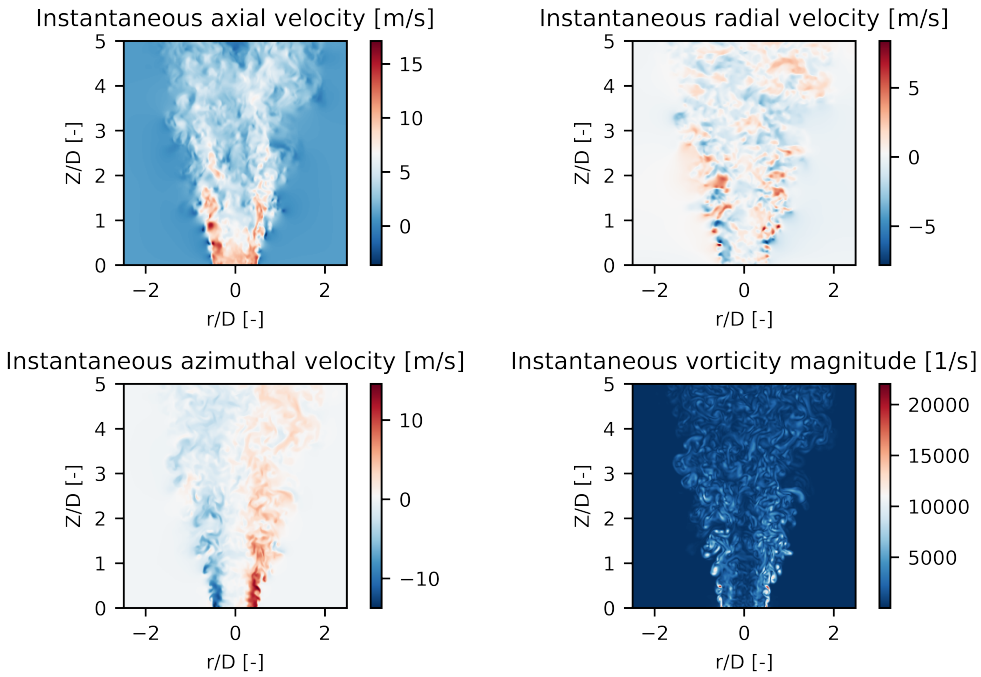

Figure 4.1 Instantaneous velocity and vorticity for the Inflow-2 simulation

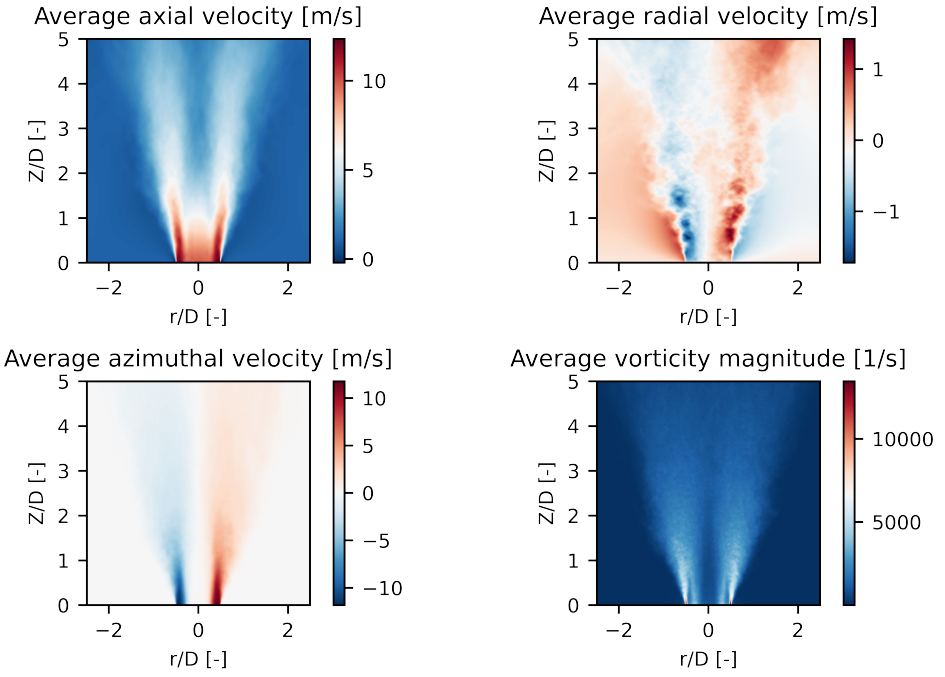

Figure 4.2 Average velocity and vorticity statistics for the Inflow-2 simulation

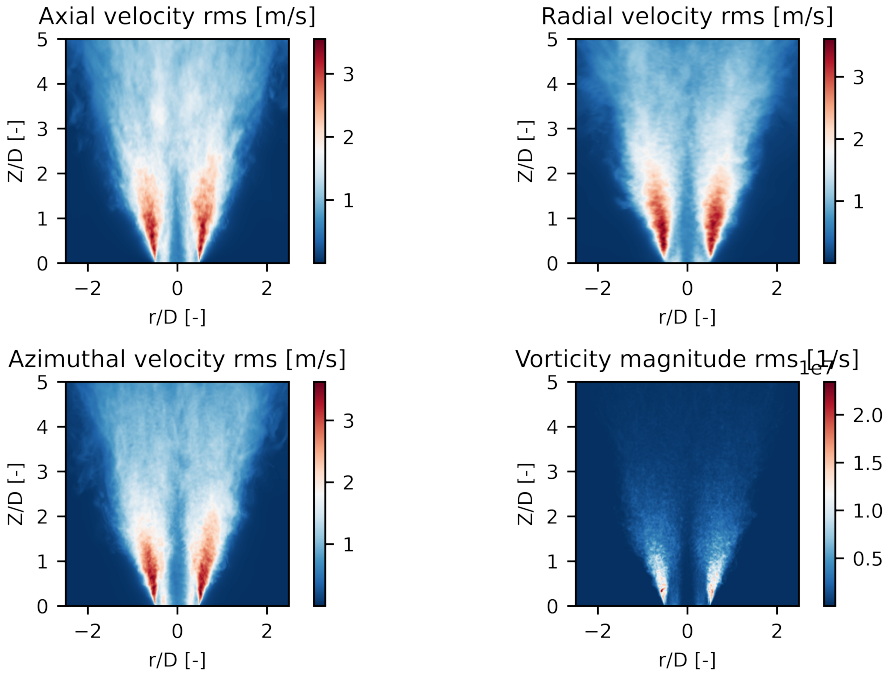

Figure 4.3 Rms velocity and vorticity statistics for the Inflow-2 simulation

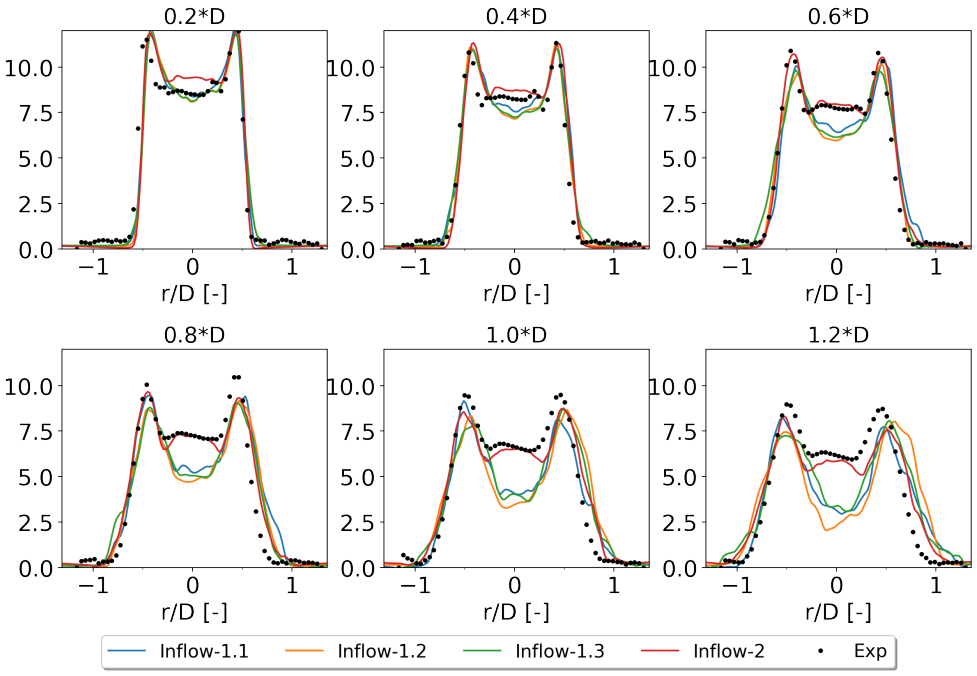

Figure 4.4 Average axial velocity [m/s] for simulations and experimental measurements

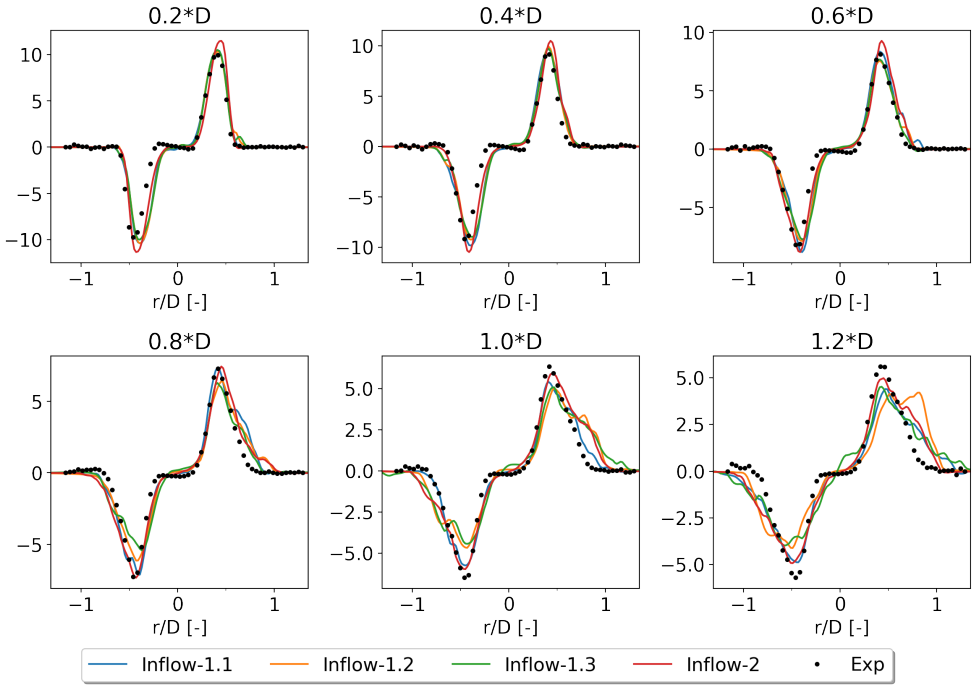

Figure 4.5 Average azimuthal velocity [m/s] for simulations and experimental measurements

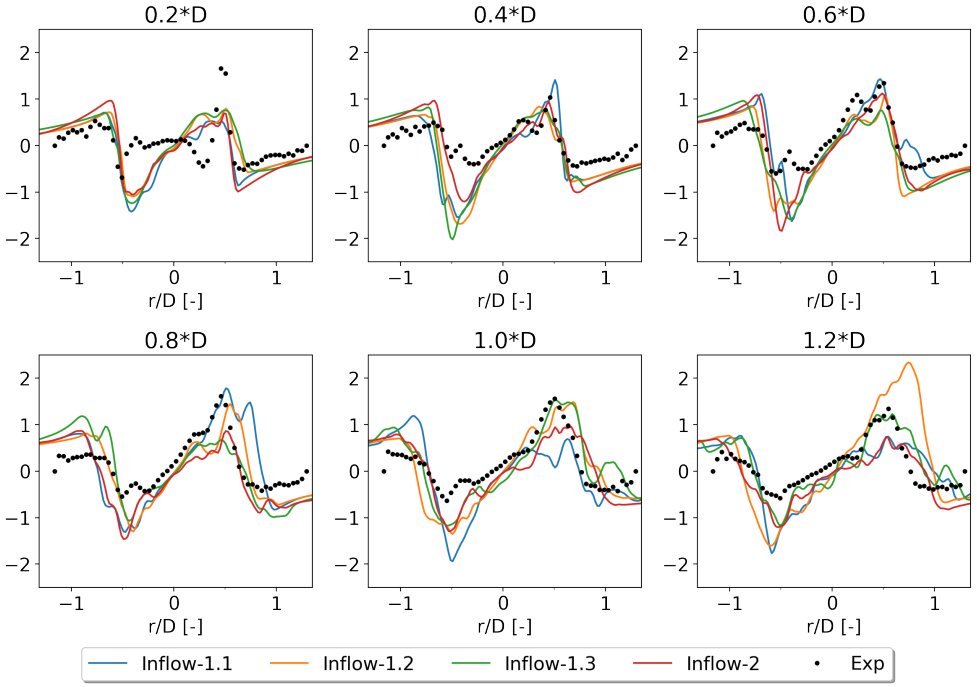

Figure 4.6 Average radial velocity [m/s] for simulations and experimental measurements

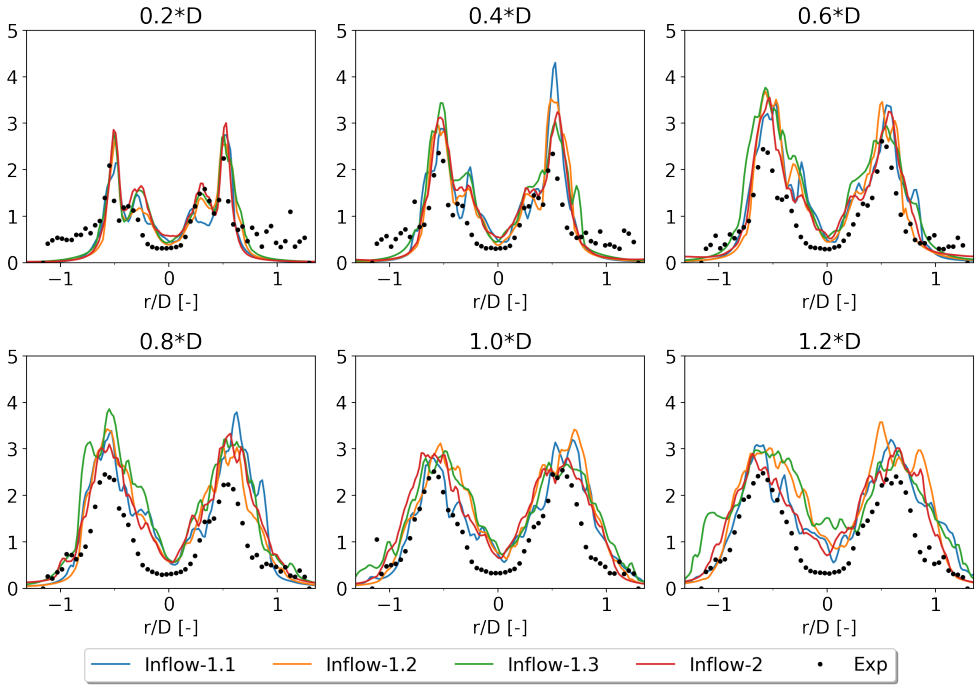

Figure 4.7 Rms axial velocity [m/s] for simulations and experimental measurements

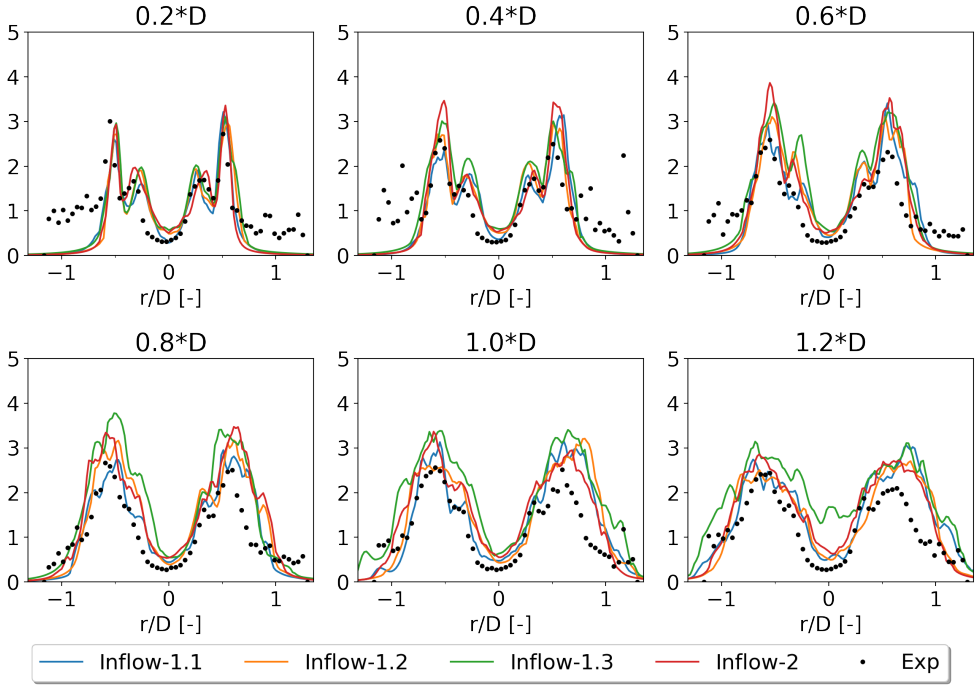

Figure 4.8 Rms azimuthal velocity [m/s] for simulations and experimental measurements

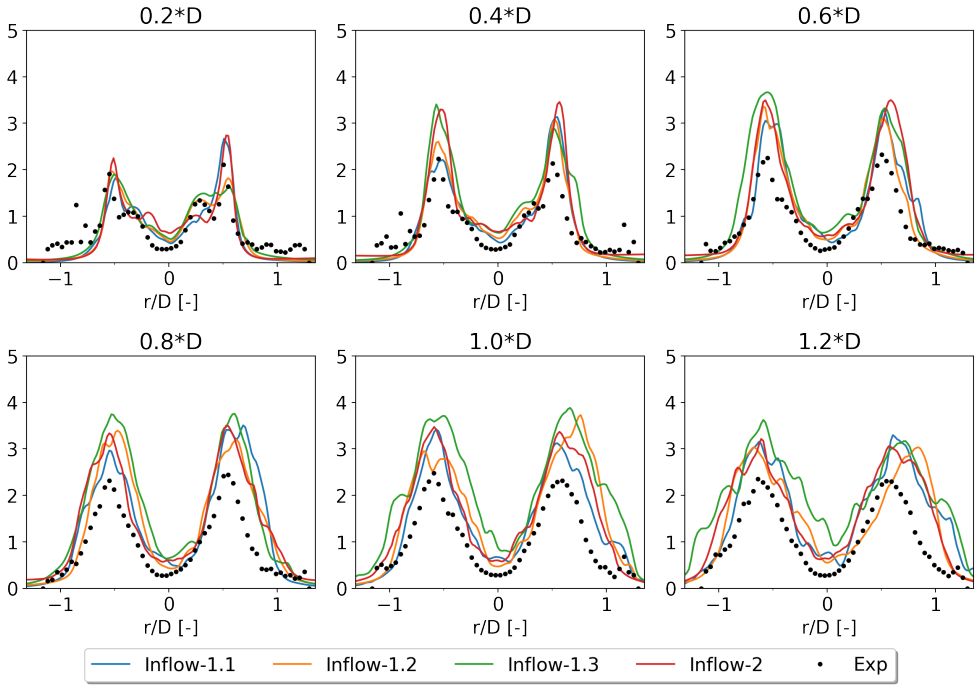

Figure 4.9 Rms radial velocity [m/s] for simulations and experimental measurements

Figure 4.10 shows the average axial velocity as a function of height above the burner in the centerline of the nozzle. The effect of coflow velocity using $U_c = 0.2$m/s and $U_c = 1$m/s are shown. More experimental data is not available further downstream since the observation window is limited. As mentioned before, the simulations Inflow-1.1-3 underpredict the axial velocity to a large degree, which is more distinguished here. For Inflow-2, there is a clear effect of the coflow, and the decay rate is much better captured with $U_c = 0.2$ m/s.

It can be concluded that resolving the flow inside the injector, and also coflow can have major consequences on the flow field developed. This is attributed to capturing the correct coherent structures and length scales attributed with the actual flow in the nozzle outlet, which is not possible to incorporate using the first approach. Finally, Inflow-2 was used in the reactive swirl flame-wall interaction simulation, discussed later.

4.2 Turbulent boundary layer

In this section, we present the results of the turbulent boundary layer (TBL) simulations mentioned in Table 3.2. As discussed in the methodology section, three simulations have been performed based on varying maximum AMR level on the wall. In the TBL2 simulation for instance, grids with AMR level 2 are used all through the length and span of the wall,

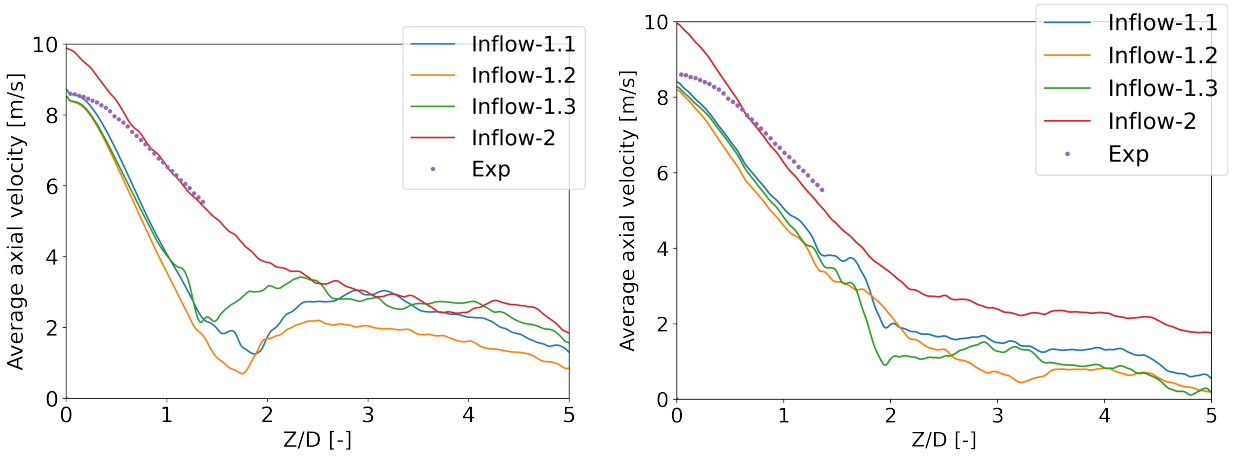

(a) $U_c = 0.2$ m/s (b) $U_c = 1$ m/s

Figure 4.10 Average axial velocity along the nozzle centerline for different coflow velocity cases

stretching up to $y^+ = 10$. This is followed by AMR level 1 from $y^+ = 10$ to $y^+ = 20$, and level 0 further away from the wall. For TBL1, ARM level 1 is used up to $y^+ = 10$, and level 0 elsewhere.

Figures 4.11 and 4.12 show normalized contours of instantaneous streamwise velocity and temperature for TBL2 at the middle plane of the domain. In these figures, the isothermal wall is located at the bottom and the inflow is on the left side. Normalized streamwise velocity and temperature are defined as:

$$\bar{U} = \frac{u}{U_\infty} \tag{4.1}$$

$$\Theta = \frac{T - T_{wall}}{T_\infty - T_{wall}} \tag{4.2}$$

where u is streamwise velocity, U_∞ is the free stream inlet velocity, and T_{wall} and T_∞ are wall and free stream inlet temperature respectively. Rectangular boxes of HIT, which are introduced in the domain periodically, are visible in the first plot. Periodically, these help trigger the laminar to turbulent transition and decay as they move downstream. The flow is almost laminar up to around $x = 60\theta_0$, going into transition and finally becoming turbulent.

Figure 4.13 shows the instantaneous skin friction and Stanton number contours for case TBL2. Heat flux is normalized using the Stanton number [101], defined as:

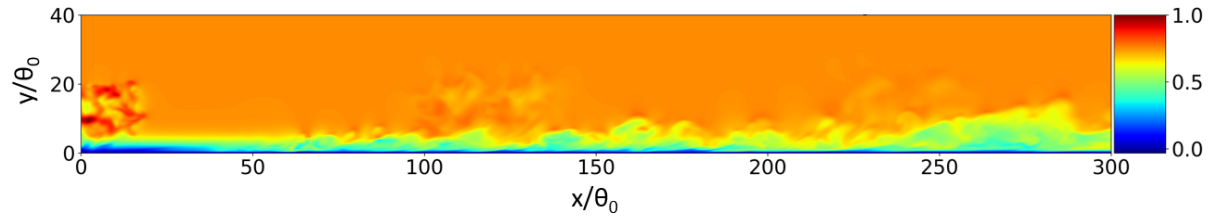

Figure 4.11 Instantaneous normalized streamwise velocity contours for the TBL2 simulation

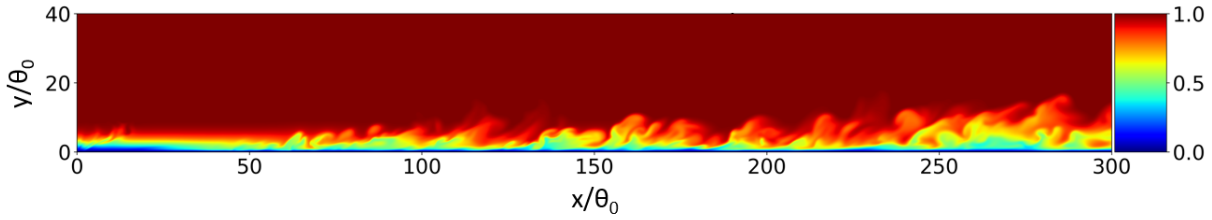

Figure 4.12 Instantaneous normalized temperature contours for the TBL2 simulation

$$St = \frac{q_{wall}}{\rho U_\infty c_p (T_{wall} - T_\infty)} \tag{4.3}$$

where q_{wall} is the local heat flux to the wall, ρ is the fluid density, and c_p is the fluid specific heat capacity. The view is from the top of the plate with inflow on the left and outflow on the right. Skin friction increases dramatically as the laminar boundary layer transitions around $x = 60\theta_0$ downstream, which is expected since turbulent boundary layer is attributed with higher skin friction than the laminar one [102].

Figure 4.14 shows the calculated normalized y^* values for TBL simulations as a function of axial position. y^* decreases rapidly as the boundary layer becomes progressively turbulent and remains almost constant after $x = 125\theta_0$. This position corresponds to the laminar to turbulent transition, as suggested in the previous plots. Good agreement for y^* is also observed between different levels. Literature suggests $y^*/\theta_0 \approx 0.1$ for adiabatic turbulent boundary layers in the range of Reynolds number of this simulation ($Re_\theta \approx 200$) [103]. However, since the wall temperature in this simulation is much lower than that of the free-stream fluid, with a ratio of kinematic viscosity of approximately five between the free stream and near-wall regions, we observe lower y^* values.

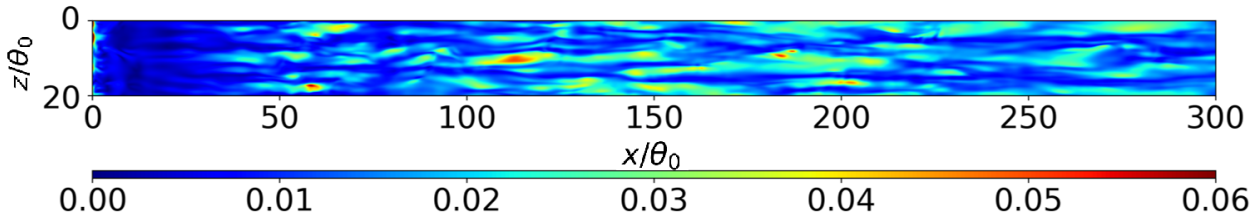

(a)

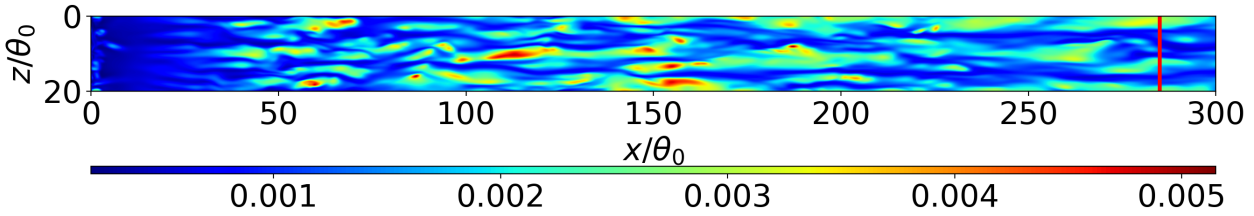

(b)

Figure 4.13 Instantaneous statistics for the TBL2 simulation on the wall: (a) skin friction (b) Stanton number. The red line in Figure (b) shows the averaging plane used to obtain statistics in Figures 4.15-4.16.

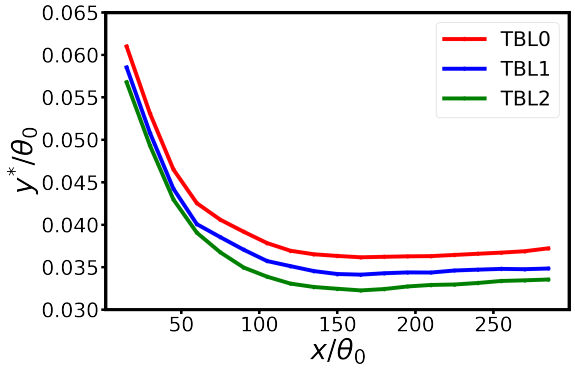

Figure 4.14 y^* vs. axial position for the TBL simulations

Here we compare the results of various statistics including mean and fluctuating averages for the three simulations as a function of wall distance, y^+. The investigation plane is located at 0.95 of domain length near the outlet, as shown in Figure 4.13 (b).

Figures 4.15 and 4.16 compare first order and second order statistics obtained for simulations TBL0, TBL1, and TBL2. v and w are wall-normal and spanwise velocity respectively. Ex-

cellent agreement is observed between the simulations for the mean quantities (Figures 4.15a and 4.15b), especially for level 1 and 2. For the rest of the plots in Figure 4.15b, deviations are observed for level 0, especially further away from the wall ($y^+ > 20$). However, good agreement between level 1 and 2 remains. Since the minimum y^+ is around 1.4 for TBL1 simulation, according to Table 3.2, one can conclude that using y^+ around 1.4 is sufficient to capture grid-independent first- and second-order statistics for the cooled turbulent boundary layer simulation studied here.

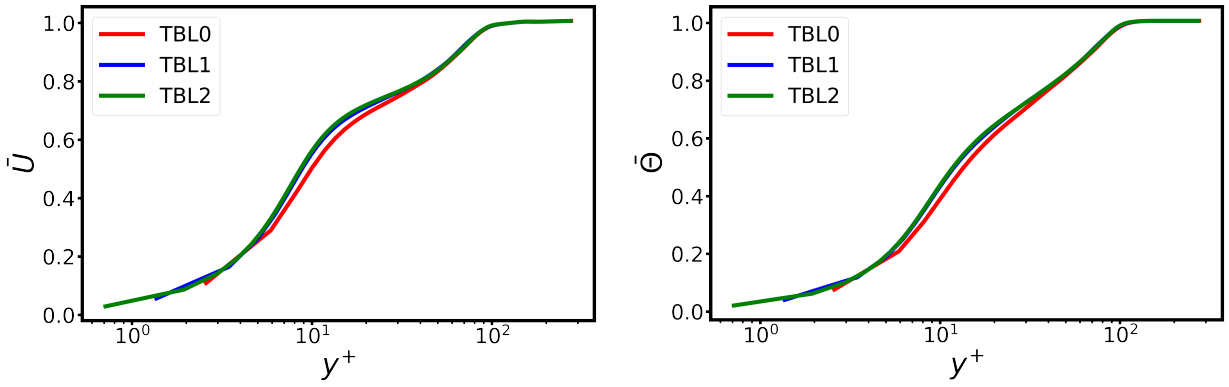

(a) (b)

Figure 4.15 First order statistics for the TBL simulations

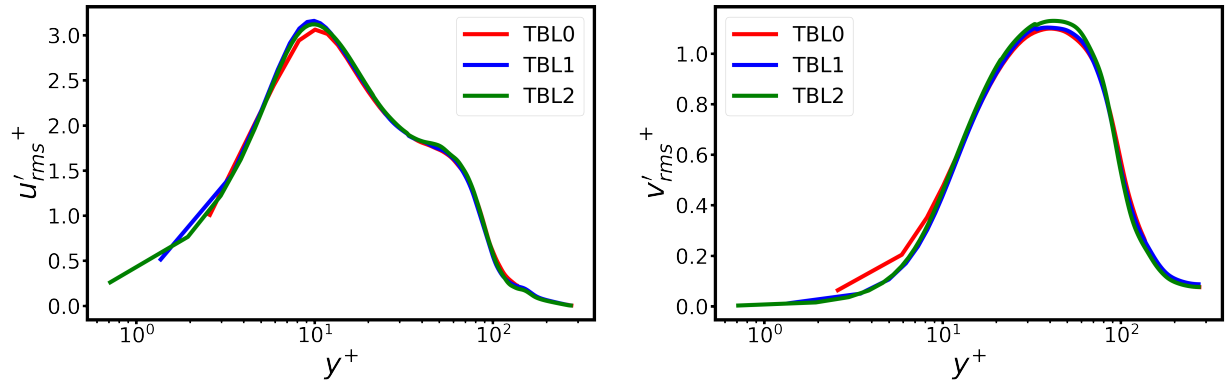

(a) (b)

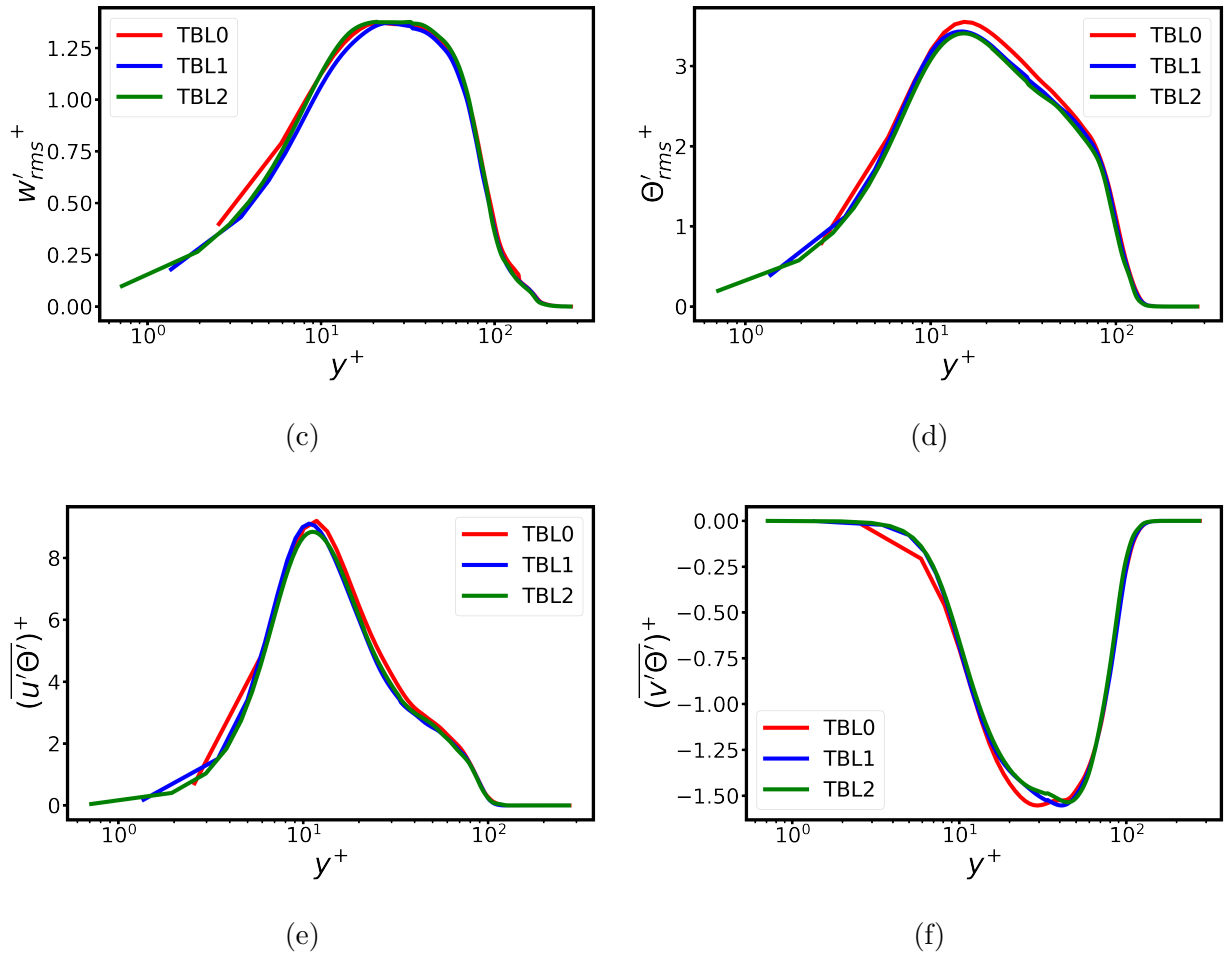

Figure 4.16 Second order statistics for the TBL simulations

Figure 4.17 shows averaged and rms of normalized heat flux to the isothermal cooled wall as a function of axial position. Heat flux is normalized using the Stanton number defined earlier. Both average and rms values tend to increase up to the laminar to turbulent transition point, followed by a very slow decrease as the Reynolds number increases, which was also observed in other studies on turbulent thermal boundary layers [103–105]. Great agreement is observed between different levels both for average and rms values. This shows that using y^+ around 1.4 is sufficient to obtain grid-independent first- and second-order statistics of heat flux from the turbulent boundary layer to the cooled wall.

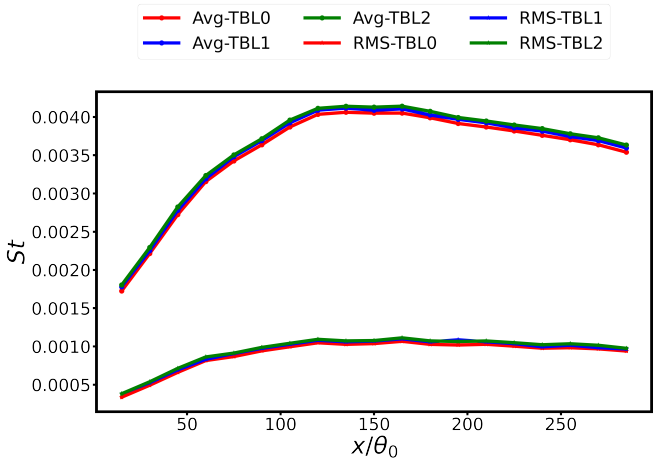

Figure 4.17 Average and rms of normalized heat flux to the wall as a function of axial position

4.3 Turbulent flame-wall interaction

As mentioned in the methodology section, the SFWI simulation has been run up to AMR level 2 in this thesis. We present the preliminary results obtained from the simulation. The rest of the project using AMR level 4 and more detailed numerical analysis will be performed in the future.

4.3.1 Comparison with experimental results

Figure 4.18 compares the concentration of OH for the experiment (left) with numerical simulation results (right). The results for the simulation using both Inflow-1 and Inflow-2 are shown. Coflow velocity is $U_c = 1$ m/s. The wall location is shown using the inclined white line on the left, and the white horizontal line marks $Z = 1.25D$ for reference. Comparing the results from the simulations and experiment, it is shown that using Inflow-2 leads to much better results in terms of flame location. Flame lift-off height is underpredicted using Inflow-1, which is expected since the axial velocity was also underpredicted in the non-reactive simulation results shown in Figure 4.10. Hence, Inflow-2 has been chosen as the ideal inflow for the simulation and was used for the results presented in the rest of this section. Good qualitative agreement is seen between the simulation using Inflow-2 and the experiment. Axial location and width of the flame match with the simulation, although only two levels of AMR have been used. The leading edge of the flame features fragmented flame fronts, which is attributed to the hydrogen fuel. Due to sub-unity Lewis number of hydrogen, the flame is subject to thermo-diffusive instabilities. This kind of instability leads to cellular

structures on the flame front [10, 42]. Moreover, due to higher mass diffusivity of hydrogen than thermal diffusivity, positive curvatures (convex to the reactants) are more probable than negative ones [41]. This is also visible in the OH concentration figures. The flame position also is well-captured in the simulation. Figure 4.19 also shows the mean position of OH concentration in the experiments (left) and simulation (right), using $U_c = 1$ m/s. This plot also shows that the simulation has good agreement in terms of mean flame position with the experiments.

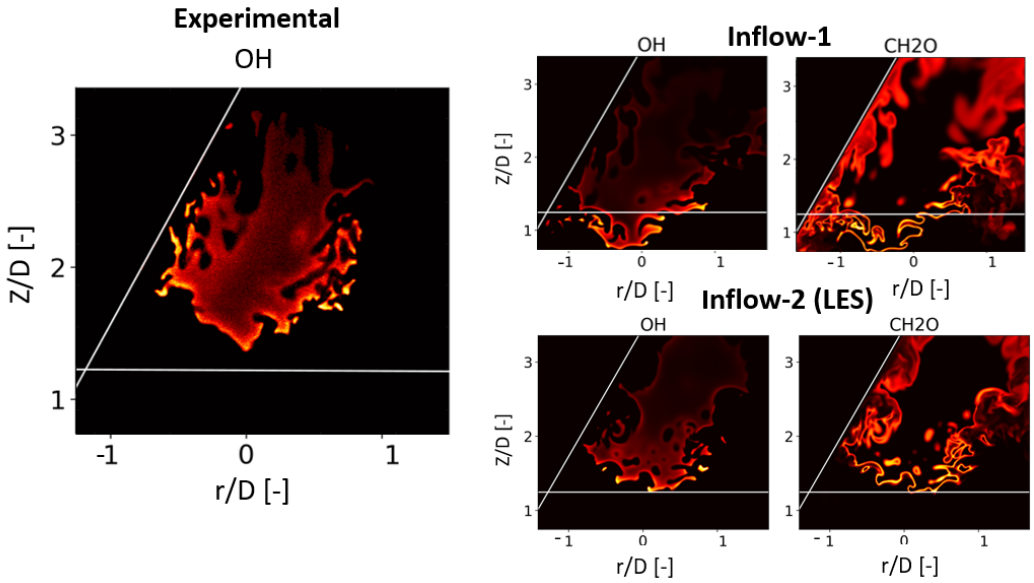

Figure 4.18 Instantaneous OH concentration in the experiment (left) and OH and CH2O concentration in the SFWI simulation with Inflow-1 (top right) and Inflow-2 (bottom right)

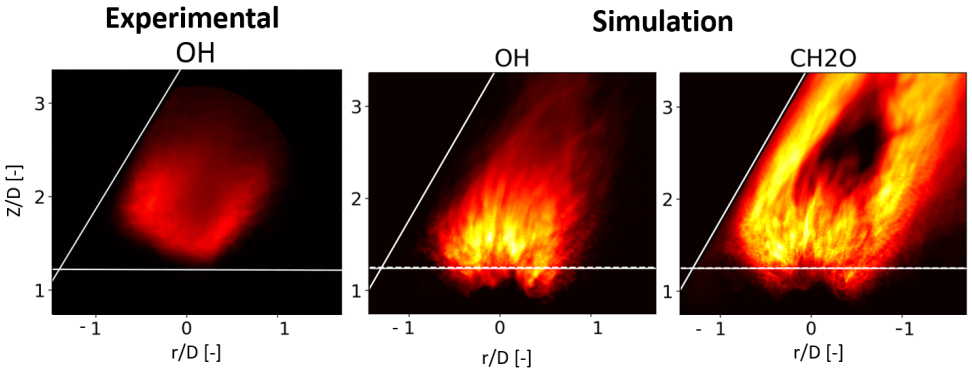

Figure 4.19 Mean OH concentration in the experiment (left) and mean OH and CH2O concentration in the SFWI simulation (right)

Figure 4.20 shows the average velocity magnitude from the experiments and the simulation

using Inflow-2 and different coflow velocities. The field of view in the experiments is from the PIV which is a rectangular section parallel with the wall. Three different cases have been shown from the simulation using $U_c = 2$ m/s, $U_c = 1$ m/s, and $U_c = 0.2$ m/s. The equivalence ratio for $U_c = 2$ m/s simulation is a bit lower (0.39) compared to the other simulations (0.41), but does not have major effects on the flow field. The main contributor to the difference observed in the simulations is due to the coflow velocity. It is shown that using higher coflow velocities can lead to narrower flame and recirculation zone. However, as mentioned in the methodology section, the range of uncertainty for coflow velocity lies between 0.2 m/s to 2 m/s. The low-velocity region formed in the simulation using colflow velocities 1 m/s and 0.2 m/s is wider than the experiments in the wall-normal direction. This shows the considerable impact of the coflow on the flame stabilization. Detailed experimental measurements of the coflow velocity are needed and will be available in the near future.

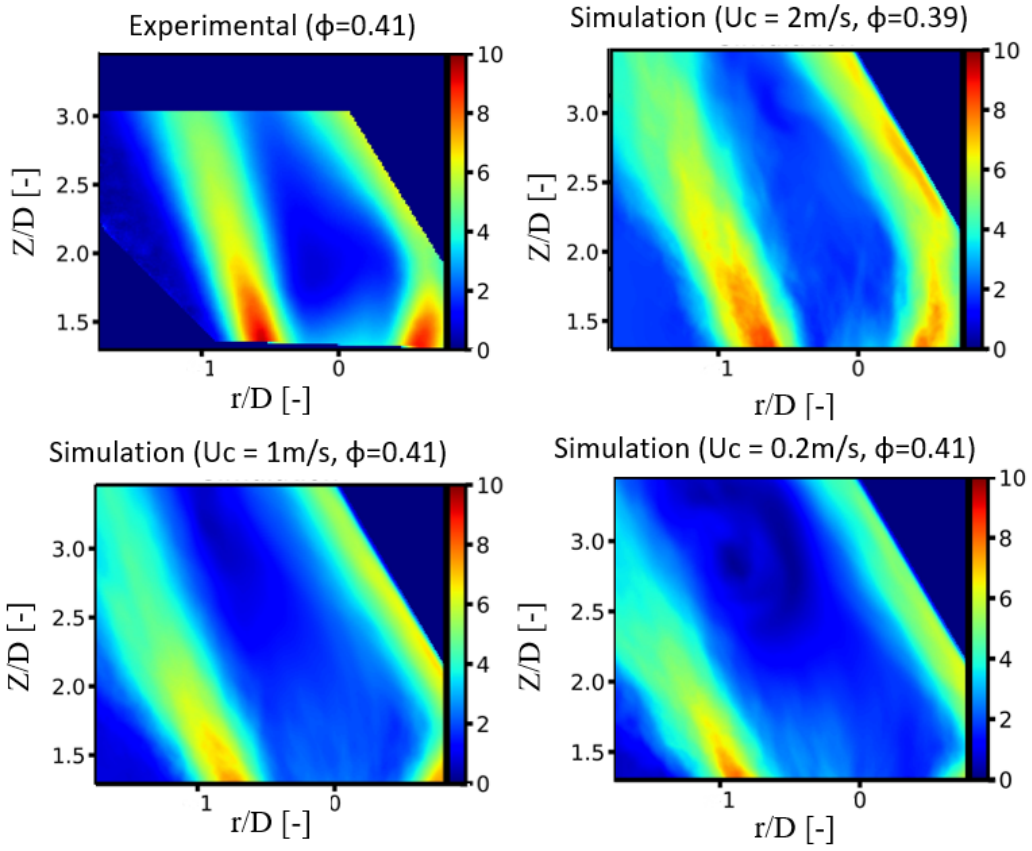

Figure 4.20 Average velocity magnitude comparison for experiment and simulation near the wall

4.3.2 General flow features

Figures presented in this section are obtained using Inflow-2 and $U_c = 1$ m/s. Figure 4.21 shows the instantaneous flow field plots using axial velocity and vorticity magnitude. The plots are zoomed in to show the flow field in more detail. The inclined wall is located at the left side of the domain. The low-velocity recirculation zone is visible in both plots starting a bit higher than $Z = D$. A high velocity jet is impinging on the inclined wall resulting in a very thin boundary layer in that region. Vorticity magnitude is shown to be higher in the outer shear layer due to the strong shear stress resulting from the interaction with the low-velocity coflow. The divergent swirl flow is visible from the vorticity plot, decaying as the flow evolves due to dissipation. It is also visible that a part of the flow impinging on the wall circulates back upstream towards the inlet, shown by negative axial velocity.

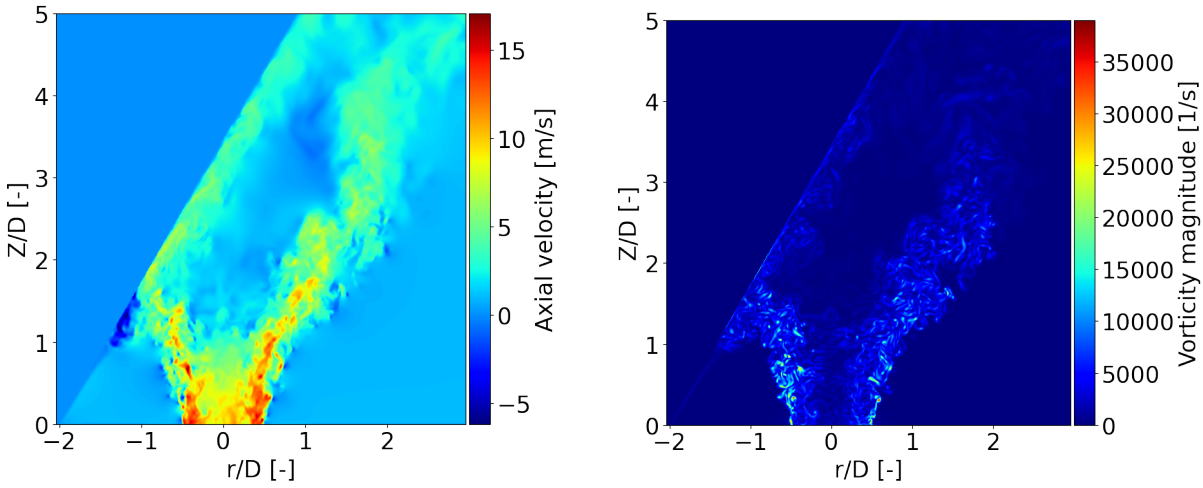

(a) Axial velocity

(b) Vorticity magnitude

Figure 4.21 Instantaneous flow field plots in the mid-plane along the x-axis for the SFWI simulation

Figure 4.22 shows instantaneous contours of several quantities in the stabilized flame in the mid-plane slice along the x-axis. Again, the plots do not show the full domain and are zoomed in the region of interest to have better visualization.

Figure 4.22a illustrates instantaneous temperature, showing that the flame is highly lifted, stabilizing around $Z = 1.2D$. Figure 4.22b shows that the flame features a corrugated yet continuous reaction zone in the leading edge region, followed by broken reaction zones downstream. A cloud of formaldehyde is observed downstream of the stabilization point (Figure 4.22c), which was also observed in the experiments [10]. In that paper, this was attributed to flame quenching as a result of high strain rate imposed on the flow. By looking

at Figures 4.22e and 4.22f, we can observe large amounts of unburned fuel in the domain which also account for incomplete combustion. Figure 4.22g is another testament to this fact showing high CO mass fraction, a good predictor of low combustion efficiency in the literature [16].

Figure 4.22h shows the ratio between methane and hydrogen mass fractions. Regions of increased ratio is observed near the flame front both upstream and downstream. Higher diffusivity of hydrogen compared to methane leads to lower mass fraction of hydrogen compared to methane. Figure 4.23 shows the time evolution of the ratio of $\gamma = Y_{CH_4}/Y_{H_2}$ at the outlet over inlet. The values at the inlet and outlet are averaged in the mid-plane. The time-averaged value over this period is around 1.05, which shows that hydrogen is consumed slightly more than methane on average in the domain.

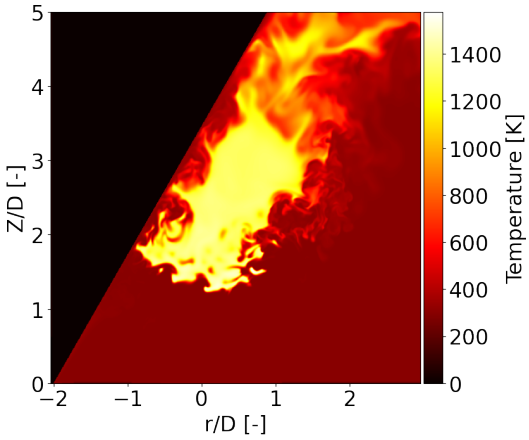

(a) Temperature

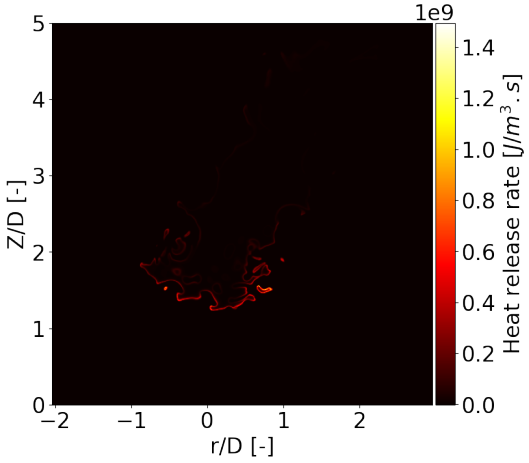

(b) Heat release rate

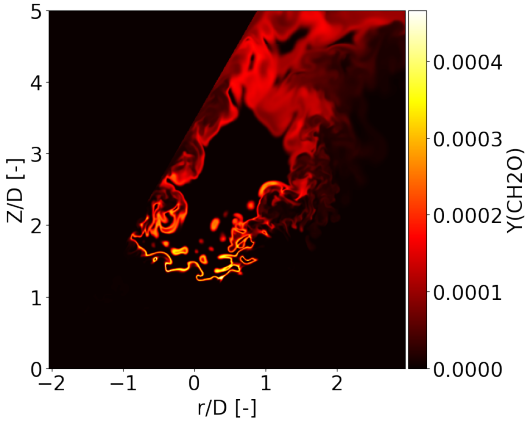

(c) Y(CH2O)

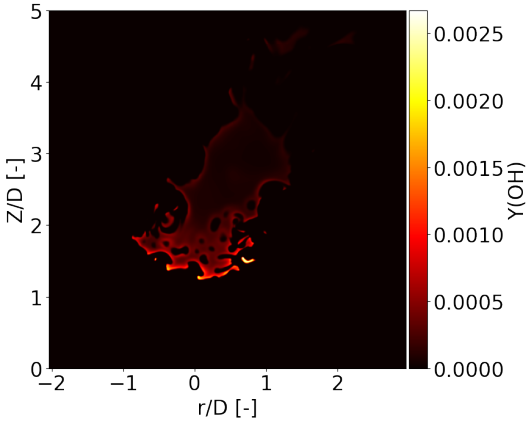

(d) Y(OH)

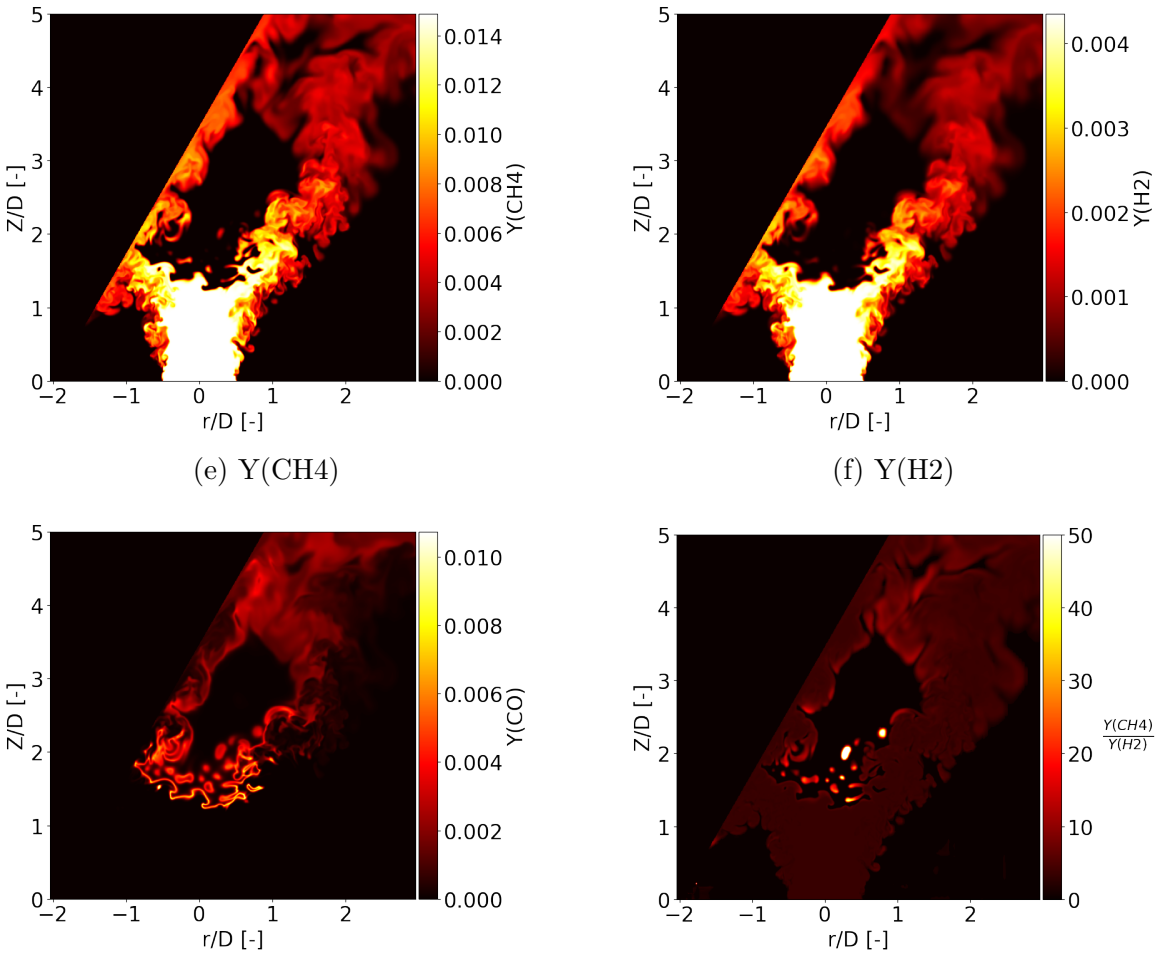

(e) Y(CH4)

(f) Y(H2)

(g) Y(CO)

(h) Y(CH4)/Y(H2)

Figure 4.22 Instantaneous plots in the mid-plane along the x-axis for SFWI simulation

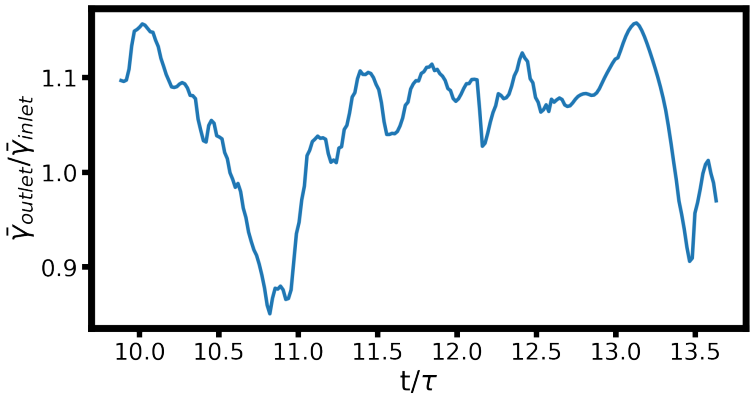

Figure 4.23 Time evolution of $\gamma = Y_{CH_4}/Y_{H_2}$ at the outlet over inlet

4.3.3 Flame quenching and wall heat loss

To assess whether heat loss to the wall plays an important role, the joint -PDF of enthalpy and equivalence ratio is shown in Figure 4.24. The red solid lines correspond to the excursion in enthalpy-equivalence ratio space of 1D unstrained flames with varying equivalence ratio in the unburned gas. The white dashed line corresponds to adiabatic mixing between the reactants and coflow air. It is clear from this figure that heat loss leads to incursions into regions of enthalpy-equivalence ratio space not accessed by adiabatic flames. This is attributed to non-negligible heat loss at the wall, as shown in Figure 4.25 showing the averaged and rms heat flux to the wall in the mid x-plane. The heat flux is normalized by the laminar flame power of the inlet mixture. The values are negative in the first few centimeters since the flame is lifted and the wall temperature is higher than the inlet mixture. This plot shows high values of average and rms heat flux to the wall. Maximum instantaneous heat flux ($\dot{Q}_{N,Q}$) as high as 0.12 of the laminar flame power was also observed. For hydrogen, this value was reported around 0.13 and 0.16 for laminar SWQ and HOQ scenarios respectively in the literature [62, 63]. The ratio of total heat loss to the wall to total heat released in the domain was found to be around 3%.

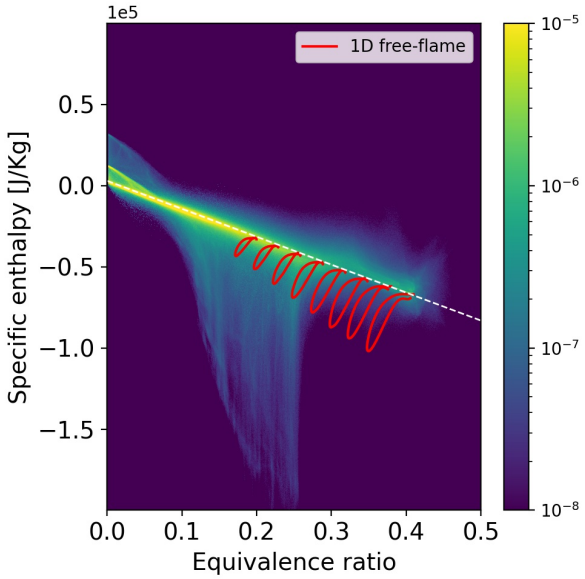

Figure 4.24 Joint-PDF of enthalpy and equivalence ratio for the entire SFWI domain. The red solid lines correspond to the excursion in enthalpy-equivalence ratio space of 1D unstrained flames with varying equivalence ratio in the unburned gas. The white dashed line is the adiabatic mixing line.

Figure 4.26a shows the conditional average of progress variable gradient magnitude ($|\nabla c|$)

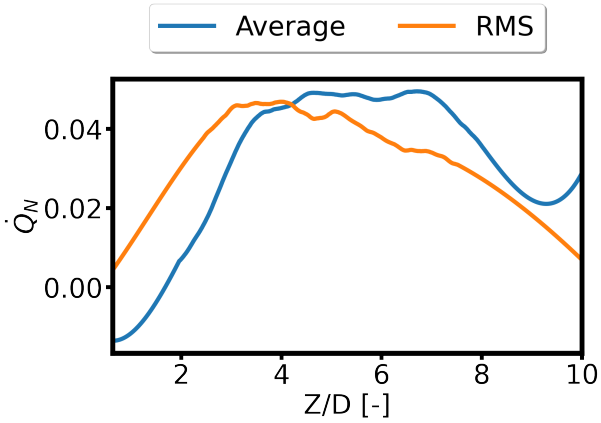

Figure 4.25 Average and rms wall heat flux normalized by laminar flame power along the mid x-plane

normalized by the laminar flame thickness of the inlet mixture, conditioned over equivalence ratio and progress variable. Progress variable is calculated based on O_2 mass fraction, and is not normalized between zero and one. Results from 1D laminar unstrained flames at various equivalence ratios are also denoted using colored markers. This plot shows that conditionally averaged $|\nabla c|$ is increased at all locations in the SFWI simulation compared to the 1D flame. This suggests that the large clouds of intermediates may be due to the low local equivalence ratios, associated with flame thickness of at least the same order of magnitude. Air entrainment from the surrounding causes these very lean mixtures as shown in Figure 4.26b. Note that increased equivalence ratio is observed in Figure 4.26b starting around $Z = D$ due to the diffusivity of hydrogen. This phenomenon, attributed to preferential diffusion, was also observed in previous studies on turbulent lean hydrogen flames [41].

Figure 4.27 shows the mean in-plane strain rate calculated in 2D (not including gradients normal to the plane) and 3D, normalized by 1D unstretched laminar flame extinction strain rate. The isocontours of average heat release rate at 10% of maximum heat release in the domain are also shown using green curves. The strain rate tensor is calculated using the equation:

$$\boldsymbol{\epsilon}_{ij} = \left(\frac{\partial u_i}{\partial x_j} + \frac{\partial u_j}{\partial x_i} \right) \tag{4.4}$$

Magnitude of the plane-normal component of the strain tensor is regarded as the in-plane strain rate magnitude. Since in the experiments there is no access to the velocity field normal to the plane (such as the one mentioned above), the mean strain rate calculated is two dimensional. It can be evaluated using the simulation if the 2D values are close to the

actual 3D values. Disagreements can be seen in the central flow near the nozzle inlet, and also inner shear layer. Generally, strain rate is more intense in the actual scenario compared to the extracted values in the experiments, but the differences are not that large. High values of strain rate are imposed on the flow around the flame front, almost an order of magnitude higher than the mean extinction strain rate of the corresponding 1D laminar flame, which is around 20 [1/s], calculated using Cantera, such as in [10]. These preliminary results suggest that the flame undergoes extinction due to high strain rate in the shear layer, which leads to the depletion of intermediate species and unburned fuel observed in Figure 4.22.

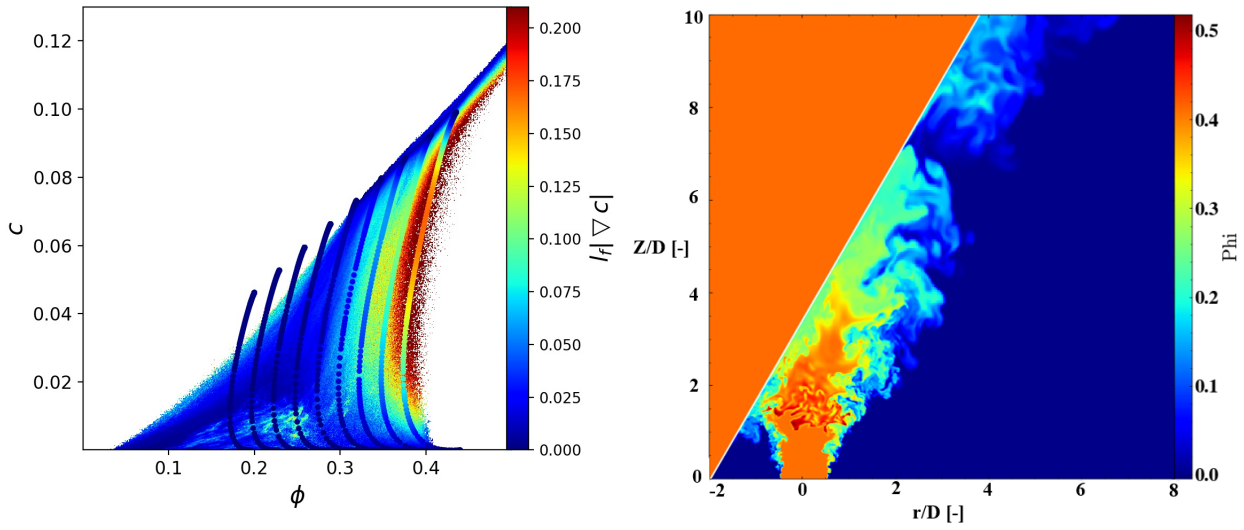

(a) (b)

Figure 4.26 (a) Conditional average of normalized progress variable gradient magnitude conditioned over equivalence ratio and progress variable. Results from 1D laminar unstrained flames at various equivalence ratios are also denoted using colored markers. (b) Instantaneous contours of equivalence ratio in the mid-plane along the x-axis for the SFWI case.

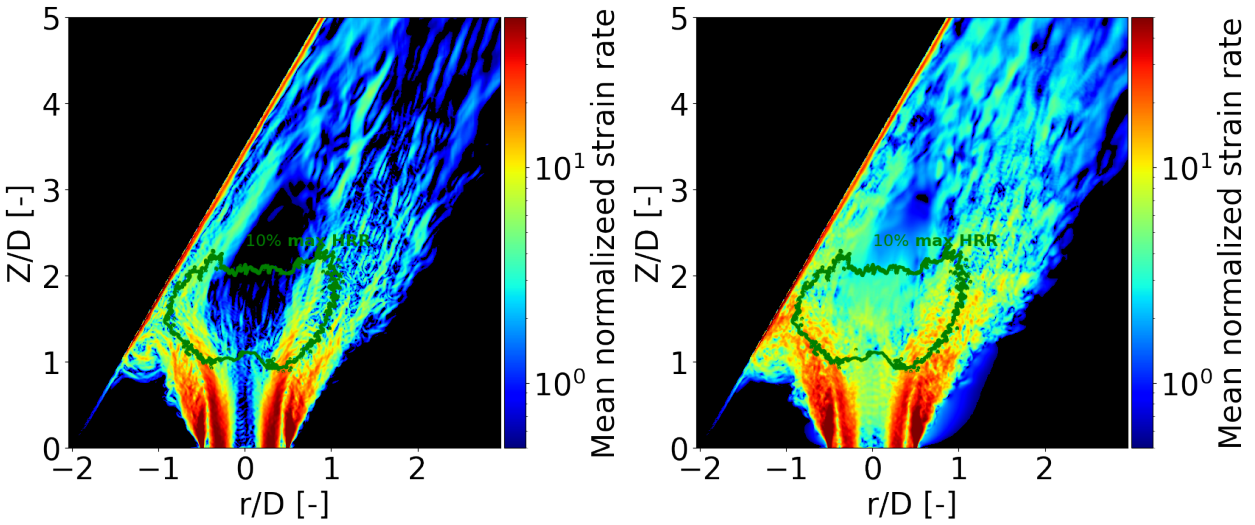

(a) Mean in-plane 2D strain rate

(b) Mean in-plane 3D strain rate

Figure 4.27 Mean in-plane 2D and 3D strain rate magnitudes

CHAPTER 5 Conclusion

5.1 Summary

Turbulent flame-wall interaction is an important phenomenon occurring in a wide range of engines which is not thoroughly understood. Advanced engines, such as modern gas turbines (GTs), are becoming more compact which accentuates flame-wall interaction. Moreover, there is an essential need for transition towards zero-carbon or low-carbon fuels to mitigate global warming and to meet low-emission regulations. After reviewing the literature, it was revealed that there are no DNS studies on turbulent flame-wall interaction of low-carbon swirl flames. Currently, these flames are of special interest in the GT combustion community to reduce carbon emission in aeroengines as well as for power generation. In this project, a setup for direct numerical simulation (DNS) of swirl laboratory flames with high hydrogen content interacting with walls is prepared.

First, non-reactive simulations have been performed to identify the best approach to impose inflow velocity for the laboratory flame. Two approaches have been proposed: first, using experimental measurements of mean and rms of velocity as the inflow, and second, performing an auxiliary LES of the nozzle flow and setting the nozzle outlet as the inflow boundary condition in the flame-wall interaction simulation. The second approach showed better match with the actual flow field in the experiments due to resolving all the complex coherent structures and turbulent length scales created by the swirler vanes.

Next, a series of simulations on a turbulent thermal boundary layer has been performed to assess the required resolution to resolve the boundary layer in the swirl flame-wall interaction simulation. It was revealed that having a minimum $y^+ = 1.4$ is sufficient to achieve grid independence on first and second-order statistics for the target turbulent boundary layer.

Next, simulations of the swirl flame interacting with the wall were performed using the second approach (linking the LES of the nozzle flow). Good agreement was observed in terms of flame lift-off height and length between the simulation and the experiments both in terms of instantaneous and mean values, although not enough AMR levels were used to resolve all the length scales in the domain. The coflow velocity, U_c, was found to have significant effect on the flame shape. Higher values of U_c reduced the width of the flame and recirculation zone, having better agreement with the experiments. Precise experimental measurements of U_c will be conducted in the near future. The flame front was fragmented and with broken reaction zones, similar to that experimentally observed. High values of strain rate was observed,

especially in the outer shear layer region, and was observed to decrease near the flame front distinguished with high values of heat release. Large amounts of formaldehyde was observed. It was argued that this may be due to the low local equivalence ratios as a consequence of air entrainment. Large amounts of unburned fuel and CO was also observed in the domain which are markers of low combustion efficiency. It was also found that wall heat loss is non-negligible and leads to a non-adiabatic thermochemical state manifold, which is associated with increased modeling complexity.

Finally, this setup is ready to run the swirl flame interacting with wall simulation with DNS resolution once the new coflow measurements are available.

5.2 Future work

The simulation will next be resumed with AMR level 3 for several flow through times, followed by the DNS resolution (AMR level 4) for approximately one flow through time.

Performing simulations by changing the boundary condition on the inclined wall from isothermal to adiabatic can shed more light on the quenching mechanism of low-carbon swirl flames by removing the effects of heat loss to the wall.

Simulations at thermochemical conditions closer to modern GTs (i.e., higher inlet temperature and pressure) and more complex geometries can be useful since they represent the actual flow conditions occurring in the combustors. This will need higher temporal and spatial resolution due to higher pressures and as a result, higher costs.

Using other zero-carbon fuels such as ammonia, or amomnia/hydrogen mixtures can also be useful since it has shown to be another good candidate for decarbonization purposes.

5.3 Publications

Here, the list of the publications from this project including papers, conference presentations, and posters are listed.

5.3.1 Refereed journal article

1. L. Fan, B. Savard, S. Carlyle, M. Nozari, R. Naaman, B. Fond, P. Vena, “Simultaneous stereo-PIV and OH×CH2O PLIF measurements in turbulent ultra lean CH4/H2 swirling wall-impinging flames”, Proceedings of the Combustion Institute, Volume 39, Issue 2, 2023, Pages 2179-2188, ISSN 1540-7489

Contributions: Used Cantera to calculate 1D laminar flame characteristics such as extinction strain rate, flame speed, and flame thickness.

5.3.2 Conference presentations

Conference papers

1. M. Nozari, M. Vabre, B. Savard, S. Jella, L. Fan, P. Vena, M. Day, L. Esclapez, "DNS of a laboratory lean CH4/H2 low-swirl flame impinging on an inclined wall: prescribing the complex inflow velocity field", Presented at the Proceedings of the Combustion Institute - Canadian Section Spring Technical Meeting, May 15-18, 2023, University of Alberta, Edmonton, Canada

2. M. Nozari, B. Savard, L. Fan, P. Vena, M. Day, L. Esclapez, "Towards DNS of a laboratory lean CH4/H2 low-swirl flame impinging on an inclined wall", Presented at the Proceedings of the Combustion Institute - Canadian Section Spring Technical Meeting, May 11-14, 2022, The University of Ottawa, Ottawa, Canada

Workshop presentation

1. M. Nozari, M. Vabre, L. Fan, L. Esclapez, P. Vena, M. Day, B. Savard, "(Towards) DNS of a laboratory lean CH4/H2 low-swirl flame impinging on an inclined wall", Presented at the 17th Premixed Turbulent Flames (PTF) Workshop, 22-23 July 2022, Vancouver, Canada

5.3.3 Posters

1. O. Chabot, M. Nozari, M. Vabre, L. Fan, P. Vena, M. Day, L. Esclapez, B. Savard, "Direct Numerical Simulation of Flame-Wall Interaction for Low-Carbon Gas Turbine Combustion", Poster presented at the Journée GPS„ March 2023, Polytechnique Montréal, Montréal, Canada

2. M. Nozari, B. Savard, L. Fan, P. Vena, M., L. Esclapez, "Towards DNS of a lean CH4/H2 low swirl laboratory scale flame impinging on an inclined wall", Poster presented at the 39th International Symposium on Combustion, 24-29 July 2022, Vancouver, Canada

REFERENCES

[1] T. Poinsot and D. Veynante, *Theoretical and Numerical Combustion*. R.T. Edwards Inc., 2005.

[2] C. K. Law, *Combustion Physics*. Cambridge University Press, 2006.

[3] S. R. Turns, *An Introduction to Combustion: Concepts and Applications*, 3rd ed. Maidenhead, England: McGraw Hill Higher Education, Feb. 2011.

[4] "CEFRC Combustion Summer School," 2014. [Online]. Available: https://cefrc.princeton.edu/

[5] N. Peters, *Turbulent Combustion*. Cambridge University Press, Aug. 2000.

[6] A. De Lataillade, F. Dabireau, B. Cuenot, and T. Poinsot, "Flame/wall interaction and maximum wall heat fluxes in diffusion burners," *Proceedings of the Combustion Institute*, vol. 29, no. 1, pp. 775–779, 2002. [Online]. Available: https://www.sciencedirect.com/science/article/pii/S1540748902800992

[7] A. Dreizler and B. Böhm, "Advanced laser diagnostics for an improved understanding of premixed flame-wall interactions," *Proceedings of the Combustion Institute*, vol. 35, no. 1, pp. 37–64, 2015. [Online]. Available: https://www.sciencedirect.com/science/article/pii/S1540748914003988

[8] M. Steinhausen, Y. Luo, S. Popp, C. Strassacker, T. Zirwes, H. Kosaka, F. Zentgraf, U. Maas, A. Sadiki, A. Dreizler, and C. Hasse, "Numerical investigation of local heat-release rates and thermo-chemical states in side-wall quenching of laminar methane and dimethyl ether flames," *Flow, Turbulence and Combustion*, vol. 106, no. 2, pp. 681–700, May 2020. [Online]. Available: https://doi.org/10.1007/s10494-020-00146-w

[9] F. Zentgraf, P. Johe, A. D. Cutler, R. S. Barlow, B. Böhm, and A. Dreizler, "Classification of flame prehistory and quenching topology in a side-wall quenching burner at low-intensity turbulence by correlating transport effects with CO2, CO and temperature," *Combustion and Flame*, p. 111681, 2021. [Online]. Available: https://www.sciencedirect.com/science/article/pii/S0010218021004247

[10] L. Fan, B. Savard, S. Carlyle, M. Nozari, R. Naaman, B. Fond, and P. Vena, "Simultaneous stereo-PIV and OH×CH2O PLIF measurements in turbulent ultra

lean CH4/H2 swirling wall-impinging flames," *Proceedings of the Combustion Institute*, 2022. [Online]. Available: https://www.sciencedirect.com/science/article/pii/S1540748922004199

[11] M. Day, L. Esclapez, N. Wimer, J. Bell, A. Nonaka, and U. O. of Science, "PeleLMeX," 5 2022. [Online]. Available: https://www.osti.gov//servlets/purl/1873317

[12] Q. An, S. Kheirkhah, J. Bergthorson, S. Yun, J. Hwang, W. J. Lee, M. K. Kim, J. H. Cho, H. S. Kim, and P. Vena, "Flame stabilization mechanisms and shape transitions in a 3D printed, hydrogen enriched, methane/air low-swirl burner," *International Journal of Hydrogen Energy*, vol. 46, no. 27, pp. 14 764–14 779, 2021. [Online]. Available: https://www.sciencedirect.com/science/article/pii/S036031992100207X

[13] N. K. Rizk, J. S. Chin, A. W. Marshall, and M. K. Razdan, "Predictions of NOx Formation Under Combined Droplet and Partially Premixed Reaction of Diffusion Flame Combustors ," *Journal of Engineering for Gas Turbines and Power*, vol. 124, no. 1, pp. 31–38, 03 1999. [Online]. Available: https://doi.org/10.1115/1.1391280

[14] M. Ferrarotti, W. De Paepe, and A. Parente, "Reactive structures and NOx emissions of methane/hydrogen mixtures in flameless combustion," *International Journal of Hydrogen Energy*, vol. 46, no. 68, pp. 34 018–34 045, 2021. [Online]. Available: https://www.sciencedirect.com/science/article/pii/S0360319921028597

[15] H. Kobayashi, A. Hayakawa, K. Somarathne, and E. Okafor, "Science and technology of ammonia combustion," *Proceedings of the Combustion Institute*, vol. 37, no. 1, pp. 109–133, 2019. [Online]. Available: https://www.sciencedirect.com/science/article/pii/S1540748918306345

[16] A. H. Lefebvre and D. R. Ballal, *Gas Turbine Combustion*. CRC Press, Apr. 2010.

[17] Y. Minamoto, K. Aoki, M. Tanahashi, and N. Swaminathan, "DNS of swirling hydrogen–air premixed flames," *International Journal of Hydrogen Energy*, vol. 40, no. 39, pp. 13 604–13 620, 2015. [Online]. Available: https://www.sciencedirect.com/science/article/pii/S036031991502145X

[18] C. Ji, D. Wang, J. Yang, and S. Wang, "A comprehensive study of light hydrocarbon mechanisms performance in predicting methane/hydrogen/air laminar burning velocities," *International Journal of Hydrogen Energy*, vol. 42, no. 27, pp. 17 260–17 274, 2017. [Online]. Available: https://www.sciencedirect.com/science/article/pii/S0360319917321833

[19] M. D. Joannon, G. Langella, F. Beretta, A. Cavaliere, and C. Noviello, "MILD combustion: Process features and technological constrains," *Combustion Science and Technology*, vol. 153, no. 1, pp. 33–50, 2000. [Online]. Available: https://doi.org/10.1080/00102200008947249

[20] J. E. Temme, P. M. Allison, and J. F. Driscoll, "Combustion instability of a lean premixed prevaporized gas turbine combustor studied using phase-averaged PIV," *Combustion and Flame*, vol. 161, no. 4, pp. 958–970, 2014. [Online]. Available: https://www.sciencedirect.com/science/article/pii/S0010218013003532

[21] A. Ingenito, A. Agresta, R. Andriani, and F. Gamma, "RQL combustion as an effective strategy to NOx reduction in gas turbine engines," vol. Volume 1: Advances in Aerospace Technology, p. V001T01A061, 11 2014. [Online]. Available: https://doi.org/10.1115/IMECE2014-36898

[22] P. De Boer, W. McLean, and H. Homan, "Performance and emissions of hydrogen fueled internal combustion engines," *International Journal of Hydrogen Energy*, vol. 1, no. 2, pp. 153–172, 1976. [Online]. Available: https://www.sciencedirect.com/science/article/pii/0360319976900689

[23] Y. Karagöz, T. Sandalcı, L. Yüksek, A. S. Dalkılıç, and S. Wongwises, "Effect of hydrogen–diesel dual-fuel usage on performance, emissions and diesel combustion in diesel engines," *Advances in Mechanical Engineering*, vol. 8, no. 8, p. 1687814016664458, 2016. [Online]. Available: https://doi.org/10.1177/1687814016664458

[24] M. Nozari, M. Eidiattarzade, S. Tabejamaat, and B. Kankashvar, "Emission and performance of a micro gas turbine combustor fueled with ammonia-natural gas," *International Journal of Engine Research*, vol. 0, no. 0, p. 14680874211005052, 0. [Online]. Available: https://doi.org/10.1177/14680874211005052

[25] S. S. Yang and Ömer L. Gülder, "Sooting characteristics of ethanol-ethylene blends in laminar coflow diffusion flames up to 10 bar," *Combustion and Flame*, vol. 225, pp. 39–47, 2021. [Online]. Available: https://www.sciencedirect.com/science/article/pii/S0010218020304521

[26] S. Mohammadnejad, P. Vena, S. Yun, and S. Kheirkhah, "Internal structure of hydrogen-enriched methane–air turbulent premixed flames: Flamelet and non-flamelet behavior," *Combustion and Flame*, vol. 208, pp. 139–157, 2019. [Online]. Available: https://www.sciencedirect.com/science/article/pii/S0010218019302755

[27] A. Gruber, R. Sankaran, E. R. Hawkes, and J. H. Chen, "Turbulent flame–wall interaction: a direct numerical simulation study," *Journal of Fluid Mechanics*, vol. 658, p. 5–32, 2010.

[28] E. R. Hawkes and J. H. Chen, "Direct numerical simulation of hydrogen-enriched lean premixed methane–air flames," *Combustion and Flame*, vol. 138, no. 3, pp. 242–258, 2004. [Online]. Available: https://www.sciencedirect.com/science/article/pii/S0010218004001154

[29] T. Mitani and F. Williams, "Studies of cellular flames in hydrogenoxygennitrogen mixtures," *Combustion and Flame*, vol. 39, no. 2, pp. 169–190, 1980. [Online]. Available: https://www.sciencedirect.com/science/article/pii/0010218080900152

[30] J. Bell, M. Day, and M. Lijewski, "Simulation of nitrogen emissions in a premixed hydrogen flame stabilized on a low swirl burner," *Proceedings of the Combustion Institute*, vol. 34, no. 1, pp. 1173–1182, 2013. [Online]. Available: https://www.sciencedirect.com/science/article/pii/S1540748912003380

[31] X. Wen, S. Hartl, A. Dreizler, J. Janicka, and C. Hasse, "Flame structure analysis of turbulent premixed/stratified flames with H2 addition considering differential diffusion and stretch effects," *Proceedings of the Combustion Institute*, vol. 38, no. 2, pp. 2993–3001, 2021. [Online]. Available: https://www.sciencedirect.com/science/article/pii/S154074892030359X

[32] R. Palulli, M. Talei, and R. L. Gordon, "Unsteady flame–wall interaction: Impact on CO emission and wall heat flux," *Combustion and Flame*, vol. 207, pp. 406–416, 2019. [Online]. Available: https://www.sciencedirect.com/science/article/pii/S0010218019302718

[33] B. Jiang, D. Brouzet, M. Talei, R. L. Gordon, Q. Cazeres, and B. Cuenot, "Turbulent flame-wall interactions for flames diluted by hot combustion products," *Combustion and Flame*, vol. 230, p. 111432, 2021. [Online]. Available: https://www.sciencedirect.com/science/article/pii/S0010218021001711

[34] M. Mann, C. Jainski, M. Euler, B. Böhm, and A. Dreizler, "Transient flame–wall interactions: Experimental analysis using spectroscopic temperature and co concentration measurements," *Combustion and Flame*, vol. 161, no. 9, pp. 2371–2386, 2014. [Online]. Available: https://www.sciencedirect.com/science/article/pii/S0010218014000674

[35] K. Yunoki, R. Kai, S. Inoue, and R. Kurose, "Numerical simulation of co formation and reduction on flame propagation due to heat loss through the cooled wall," *Energy*, vol. 236, p. 121352, 2021. [Online]. Available: https://www.sciencedirect.com/science/article/pii/S0360544221016005

[36] Y. Zhiyin, "Large-eddy simulation: Past, present and the future," *Chinese Journal of Aeronautics*, vol. 28, no. 1, pp. 11–24, 2015. [Online]. Available: https://www.sciencedirect.com/science/article/pii/S1000936114002064

[37] S. B. Pope, *Turbulent Flows*. Cambridge University Press, 2000.

[38] T. M. Alshaalan and C. J. Rutland, "Turbulence, scalar transport, and reaction rates in flame-wall interaction," *Symposium (International) on Combustion*, vol. 27, no. 1, pp. 793–799, 1998, twenty-Seventh Sysposium (International) on Combustion Volume One. [Online]. Available: https://www.sciencedirect.com/science/article/pii/S0082078498804748

[39] G. Bruneaux, T. Poinsot, and J. H. Ferziger, "Premixed flame–wall interaction in a turbulent channel flow: budget for the flame surface density evolution equation and modelling," *Journal of Fluid Mechanics*, vol. 349, p. 191–219, 1997.

[40] P. Zhao, L. Wang, and N. Chakraborty, "Analysis of the flame–wall interaction in premixed turbulent combustion," *Journal of Fluid Mechanics*, vol. 848, p. 193–218, 2018.

[41] M. Day, S. Tachibana, J. Bell, M. Lijewski, V. Beckner, and R. K. Cheng, "A combined computational and experimental characterization of lean premixed turbulent low swirl laboratory flames ii. hydrogen flames," *Combustion and Flame*, vol. 162, no. 5, pp. 2148–2165, 2015. [Online]. Available: https://www.sciencedirect.com/science/article/pii/S0010218015000164

[42] A. J. Aspden, M. S. Day, and J. B. Bell, "Turbulence–flame interactions in lean premixed hydrogen: transition to the distributed burning regime," *Journal of Fluid Mechanics*, vol. 680, p. 287–320, 2011.

[43] M. Day, J. Bell, P.-T. Bremer, V. Pascucci, V. Beckner, and M. Lijewski, "Turbulence effects on cellular burning structures in lean premixed hydrogen flames," *Combustion and Flame*, vol. 156, no. 5, pp. 1035–1045, 2009. [Online]. Available: https://www.sciencedirect.com/science/article/pii/S0010218008002927

[44] P. Rajpara, R. Shah, and J. Banerjee, "Effect of hydrogen addition on combustion and emission characteristics of methane fuelled upward swirl can combustor," *International Journal of Hydrogen Energy*, vol. 43, no. 36, pp. 17 505–17 519, 2018. [Online]. Available: https://www.sciencedirect.com/science/article/pii/S0360319918322663

[45] H. Tennekes, *A first course in turbulence*. Cambridge, Massachusetts: The MIT Press, 1972.

[46] B. Savard, E. R. Hawkes, K. Aditya, H. Wang, and J. H. Chen, "Regimes of premixed turbulent spontaneous ignition and deflagration under gas-turbine reheat combustion conditions," *Combustion and Flame*, vol. 208, pp. 402–419, 2019. [Online]. Available: https://www.sciencedirect.com/science/article/pii/S001021801930327X

[47] S. Mohammadnejad, Q. An, P. Vena, S. Yun, and S. Kheirkhah, "Thick reaction zones in non-flamelet turbulent premixed combustion," *Combustion and Flame*, vol. 222, pp. 285–304, 2020. [Online]. Available: https://www.sciencedirect.com/science/article/pii/S0010218020303709

[48] B. Savard, B. Bobbitt, and G. Blanquart, "Structure of a high karlovitz n-C7H16 premixed turbulent flame," *Proceedings of the Combustion Institute*, vol. 35, no. 2, pp. 1377–1384, 2015. [Online]. Available: https://www.sciencedirect.com/science/article/pii/S1540748914002910

[49] A. J. Aspden, M. S. Day, and J. B. Bell, "Towards the distributed burning regime in turbulent premixed flames," *Journal of Fluid Mechanics*, vol. 871, p. 1–21, 2019.

[50] E. R. Hawkes, O. Chatakonda, H. Kolla, A. R. Kerstein, and J. H. Chen, "A petascale direct numerical simulation study of the modelling of flame wrinkling for large-eddy simulations in intense turbulence," *Combustion and Flame*, vol. 159, no. 8, pp. 2690–2703, 2012, special Issue on Turbulent Combustion. [Online]. Available: https://www.sciencedirect.com/science/article/pii/S0010218011003944

[51] R. Sankaran, E. R. Hawkes, J. H. Chen, T. Lu, and C. K. Law, "Structure of a spatially developing turbulent lean methane–air bunsen flame," *Proceedings of the Combustion Institute*, vol. 31, no. 1, pp. 1291–1298, 2007. [Online]. Available: https://www.sciencedirect.com/science/article/pii/S1540748906002884

[52] J. F. Driscoll, J. H. Chen, A. W. Skiba, C. D. Carter, E. R. Hawkes, and H. Wang, "Premixed flames subjected to extreme turbulence: Some questions and recent

answers," *Progress in Energy and Combustion Science*, vol. 76, p. 100802, 2020. [Online]. Available: https://www.sciencedirect.com/science/article/pii/S036012851930036X

[53] S. Kheirkhah and Ömer L. Gülder, "A revisit to the validity of flamelet assumptions in turbulent premixed combustion and implications for future research," *Combustion and Flame*, p. 111635, 2021. [Online]. Available: https://www.sciencedirect.com/science/article/pii/S0010218021003783

[54] Q. Fan, X. Liu, X. Cai, C. Brackmann, M. Alden, X.-S. Bai, and Z. Li, "Structure and scalar correlation of ammonia/air turbulent premixed flames in the distributed reaction zone regime," *Combustion and Flame*, vol. 241, p. 112090, 2022. [Online]. Available: https://www.sciencedirect.com/science/article/pii/S0010218022001092

[55] M. J. Dunn, A. R. Masri, and R. W. Bilger, "A new piloted premixed jet burner to study strong finite-rate chemistry effects," *Combustion and Flame*, vol. 151, no. 1, pp. 46–60, 2007. [Online]. Available: https://www.sciencedirect.com/science/article/pii/S0010218007001459

[56] Y.-C. Chen and R. W. Bilger, "Experimental investigation of three-dimensional flame-front structure in premixed turbulent combustion: Ii. lean hydrogen/air bunsen flames," *Combustion and Flame*, vol. 138, no. 1, pp. 155–174, 2004. [Online]. Available: https://www.sciencedirect.com/science/article/pii/S0010218004000987

[57] J. Hult, S. Gashi, N. Chakraborty, M. Klein, K. W. Jenkins, S. Cant, and C. F. Kaminski, "Measurement of flame surface density for turbulent premixed flames using PLIF and DNS," *Proceedings of the Combustion Institute*, vol. 31, no. 1, pp. 1319–1326, 2007. [Online]. Available: https://www.sciencedirect.com/science/article/pii/S1540748906001994

[58] Q. Fan, X. Liu, L. Xu, A. A. Subash, C. Brackmann, M. Aldén, X.-S. Bai, and Z. Li, "Flame structure and burning velocity of ammonia/air turbulent premixed flames at high karlovitz number conditions," *Combustion and Flame*, vol. 238, p. 111943, 2022. [Online]. Available: https://www.sciencedirect.com/science/article/pii/S0010218021006866

[59] B. Zhou, C. Brackmann, Q. Li, Z. Wang, P. Petersson, Z. Li, M. Aldén, and X. song Bai, "Distributed reactions in highly turbulent premixed methane/air flames: Part i. flame structure characterization," *Combustion and Flame*, vol. 162, no. 7, pp. 2937–2953, 2015. [Online]. Available: https://www.sciencedirect.com/science/article/pii/S0010218015000504

[60] A. W. Skiba, T. M. Wabel, C. D. Carter, S. D. Hammack, J. E. Temme, and J. F. Driscoll, "Premixed flames subjected to extreme levels of turbulence part i: Flame structure and a new measured regime diagram," *Combustion and Flame*, vol. 189, pp. 407–432, 2018. [Online]. Available: https://www.sciencedirect.com/science/article/pii/S0010218017303139

[61] J. Sotton, B. Boust, S. A. Labuda, and M. Bellenoue, "Head-on quenching of transient laminar flame: heat flux and quenching distance measurements," *Combustion Science and Technology*, vol. 177, no. 7, pp. 1305–1322, 2005. [Online]. Available: https://doi.org/10.1080/00102200590950485

[62] F. Dabireau, B. Cuenot, O. Vermorel, and T. Poinsot, "Interaction of flames of H2 + O2 with inert walls," *Combustion and Flame*, vol. 135, no. 1, pp. 123–133, 2003. [Online]. Available: https://www.sciencedirect.com/science/article/pii/S0010218003001548

[63] T. Poinsot, D. Haworth, and G. Bruneaux, "Direct simulation and modeling of flame-wall interaction for premixed turbulent combustion," *Combustion and Flame*, vol. 95, no. 1, pp. 118–132, 1993. [Online]. Available: https://www.sciencedirect.com/science/article/pii/0010218093900569

[64] S. Labuda, M. Karrer, J. Sotton, and M. Bellenoue, "Experimental study of single-wall flame quenching at high pressures," *Combustion Science and Technology*, vol. 183, no. 5, pp. 409–426, 2011. [Online]. Available: https://doi.org/10.1080/00102202.2010.528815

[65] R. Friedman and W. C. Johnston, "The wall-quenching of laminar propane flames as a function of pressure, temperature, and air-fuel ratio," *Journal of Applied Physics*, vol. 21, no. 8, pp. 791–795, Aug. 1950. [Online]. Available: https://doi.org/10.1063/1.1699760

[66] C. K. Westbrook, A. A. Adamczyk, and G. A. Lavoie, "A numerical study of laminar flame wall quenching," *Combustion and Flame*, vol. 40, pp. 81–99, 1981. [Online]. Available: https://www.sciencedirect.com/science/article/pii/0010218081901127

[67] W. Daniel, "Flame quenching at the walls of an internal combustion engine," *Symposium (International) on Combustion*, vol. 6, no. 1, pp. 886–894, 1957, sixth Symposium (International) on Combustion. [Online]. Available: https://www.sciencedirect.com/science/article/pii/S0082078457801258

[68] C. Hasse, M. Bollig, N. Peters, and H. Dwyer, "Quenching of laminar iso-octane flames at cold walls," *Combustion and Flame*, vol. 122, no. 1, pp. 117–129, 2000. [Online]. Available: https://www.sciencedirect.com/science/article/pii/S0010218000001073

[69] Y. Luo, C. Strassacker, C. Hasse, and U. Maas, "Simulation of side-wall quenching of laminar premixed flames with manifold-based reduced kinetic models implemented in generalised coordinates," *Combustion Theory and Modelling*, vol. 25, no. 4, pp. 669–694, 2021. [Online]. Available: https://doi.org/10.1080/13647830.2021.1933603

[70] C. Jainski, M. Rißmann, S. Jakirlic, B. Böhm, and A. Dreizler, "Quenching of premixed flames at cold walls: Effects on the local flow field," *Flow, Turbulence and Combustion*, vol. 100, no. 1, pp. 177–196, Aug. 2017. [Online]. Available: https://doi.org/10.1007/s10494-017-9836-8

[71] H. Kosaka, F. Zentgraf, A. Scholtissek, C. Hasse, and A. Dreizler, "Effect of flame-wall interaction on local heat release of methane and DME combustion in a side-wall quenching geometry," *Flow, Turbulence and Combustion*, vol. 104, no. 4, pp. 1029–1046, Nov. 2019. [Online]. Available: https://doi.org/10.1007/s10494-019-00090-4

[72] K. Niemietz, L. Berger, M. Huth, A. Attili, and H. Pitsch, "Direct numerical simulation of flame-wall interaction at gas turbine relevant conditions," *Proceedings of the Combustion Institute*, 2022. [Online]. Available: https://www.sciencedirect.com/science/article/pii/S1540748922003698

[73] J. Lai, N. Chakraborty, P. Zhao, and L. Wang, "Heat flux and flow topology statistics in oblique and head-on quenching of turbulent premixed flames by isothermal inert walls," *Combustion Science and Technology*, vol. 191, no. 2, pp. 353–381, 2019. [Online]. Available: https://doi.org/10.1080/00102202.2018.1467897

[74] H. Wang, G. Chen, K. Luo, E. R. Hawkes, J. H. Chen, and J. Fan, "Turbulence/flame/wall interactions in non-premixed inclined slot-jet flames impinging at a wall using direct numerical simulation," *Proceedings of the Combustion Institute*, vol. 38, no. 2, pp. 2711–2720, 2021. [Online]. Available: https://www.sciencedirect.com/science/article/pii/S1540748920303990

[75] J. C. Massey, Z. X. Chen, and N. Swaminathan, "Modelling heat loss effects in the large eddy simulation of a lean swirl-stabilised flame," *Flow, Turbulence and Combustion*, vol. 106, no. 4, pp. 1355–1378, Jul. 2020. [Online]. Available: https://doi.org/10.1007/s10494-020-00192-4

[76] P. Agostinelli, D. Laera, I. Boxx, L. Gicquel, and T. Poinsot, "Impact of wall heat transfer in large eddy simulation of flame dynamics in a swirled combustion chamber," *Combustion and Flame*, vol. 234, p. 111728, 2021. [Online]. Available: https://www.sciencedirect.com/science/article/pii/S0010218021004715

[77] H. Wang, E. R. Hawkes, B. Savard, and J. H. Chen, "Direct numerical simulation of a high Ka CH4/air stratified premixed jet flame," *Combustion and Flame*, vol. 193, pp. 229–245, 2018. [Online]. Available: https://www.sciencedirect.com/science/article/pii/S0010218018301354

[78] H. Wang, E. R. Hawkes, B. Zhou, J. H. Chen, Z. Li, and M. Aldén, "A comparison between direct numerical simulation and experiment of the turbulent burning velocity-related statistics in a turbulent methane-air premixed jet flame at high karlovitz number," *Proceedings of the Combustion Institute*, vol. 36, no. 2, pp. 2045–2053, 2017. [Online]. Available: https://www.sciencedirect.com/science/article/pii/S1540748916303625

[79] H. Wang, E. R. Hawkes, and J. H. Chen, "A direct numerical simulation study of flame structure and stabilization of an experimental high Ka CH4/air premixed jet flame," *Combustion and Flame*, vol. 180, pp. 110–123, 2017. [Online]. Available: https://www.sciencedirect.com/science/article/pii/S001021801730069X

[80] H. Wang, E. R. Hawkes, J. H. Chen, B. Zhou, Z. Li, and M. Aldén, "Direct numerical simulations of a high Karlovitz number laboratory premixed jet flame – an analysis of flame stretch and flame thickening," *Journal of Fluid Mechanics*, vol. 815, p. 511–536, 2017.

[81] M. Day, S. Tachibana, J. Bell, M. Lijewski, V. Beckner, and R. K. Cheng, "A combined computational and experimental characterization of lean premixed turbulent low swirl laboratory flames: I. methane flames," *Combustion and Flame*, vol. 159, no. 1, pp. 275–290, 2012. [Online]. Available: https://www.sciencedirect.com/science/article/pii/S0010218011001969

[82] K.-J. Nogenmyr, C. Fureby, X. Bai, P. Petersson, R. Collin, and M. Linne, "Large eddy simulation and laser diagnostic studies on a low swirl stratified premixed flame," *Combustion and Flame*, vol. 156, no. 1, pp. 25–36, 2009. [Online]. Available: https://www.sciencedirect.com/science/article/pii/S0010218008002083

[83] M. Cheng, H. Wang, K. Luo, and J. Fan, "A DNS study on the flame structures and flame stabilization mechanism of a laboratory-scale lean premixed jet flame in crossflow," *Proceedings of the Combustion Institute*, 2022. [Online]. Available: https://www.sciencedirect.com/science/article/pii/S1540748922003704

[84] H. Wang, K. Luo, F. Yi, and J. Fan, "Analysis of flame characteristics in a laboratory-scale turbulent lifted jet flame via DNS," *International Journal of Spray*

and Combustion Dynamics, vol. 5, no. 3, pp. 225–242, 2013. [Online]. Available: https://doi.org/10.1260/1756-8277.5.3.225

[85] J. Lai, U. Ahmed, M. Klein, and N. Chakraborty, "A comparison between head-on quenching of stoichiometric methane-air and hydrogen-air premixed flames using direct numerical simulations," *International Journal of Heat and Fluid Flow*, vol. 93, p. 108896, 2022. [Online]. Available: https://www.sciencedirect.com/science/article/pii/S0142727X21001260

[86] P. Zhao, L. Wang, and N. Chakraborty, "Effects of the cold wall boundary on the flame structure and flame speed in premixed turbulent combustion," *Proceedings of the Combustion Institute*, vol. 38, no. 2, pp. 2967–2976, 2021. [Online]. Available: https://www.sciencedirect.com/science/article/pii/S1540748920303060

[87] U. Ahmed, N. Chakraborty, and M. Klein, "Scalar gradient and strain rate statistics in oblique premixed flame–wall interaction within turbulent channel flows," *Flow, Turbulence and Combustion*, vol. 106, no. 2, pp. 701–732, Jun. 2020. [Online]. Available: https://doi.org/10.1007/s10494-020-00169-3

[88] A. Nonaka, J. B. Bell, M. S. Day, C. Gilet, A. S. Almgren, and M. L. Minion, "A deferred correction coupling strategy for low mach number flow with complex chemistry," *Combustion Theory and Modelling*, vol. 16, no. 6, pp. 1053–1088, 2012. [Online]. Available: https://doi.org/10.1080/13647830.2012.701019

[89] D. K. Dalakoti, B. Savard, E. R. Hawkes, A. Wehrfritz, H. Wang, M. S. Day, and J. B. Bell, "Direct numerical simulation of a spatially developing n-dodecane jet flame under spray a thermochemical conditions: Flame structure and stabilisation mechanism," *Combustion and Flame*, vol. 217, pp. 57–76, 2020. [Online]. Available: https://www.sciencedirect.com/science/article/pii/S0010218020301309

[90] A. S. Almgren, J. B. Bell, P. Colella, L. H. Howell, and M. L. Welcome, "A conservative adaptive projection method for the variable density incompressible navier–stokes equations," *Journal of Computational Physics*, vol. 142, no. 1, pp. 1–46, 1998. [Online]. Available: https://www.sciencedirect.com/science/article/pii/S0021999198958909

[91] M. S. Day and J. B. Bell, "Numerical simulation of laminar reacting flows with complex chemistry," *Combustion Theory and Modelling*, vol. 4, no. 4, pp. 535–556, 2000. [Online]. Available: https://doi.org/10.1088/1364-7830/4/4/309

[92] R. B. PEMBER, L. H. HOWELL, J. B. BELL, P. COLELLA, W. Y. CRUTCHFIELD, W. A. FIVELAND, and J. P. JESSEE, "An adaptive projection method for unsteady, low-Mach number combustion," *Combustion Science and Technology*, vol. 140, no. 1-6, pp. 123–168, 1998. [Online]. Available: https://doi.org/10.1080/00102209808915770

[93] T. Passot and A. Pouquet, "Numerical simulation of compressible homogeneous flows in the turbulent regime," *Journal of Fluid Mechanics*, vol. 181, p. 441–466, 1987.

[94] N. Jarrin, S. Benhamadouche, D. Laurence, and R. Prosser, "A synthetic-eddy-method for generating inflow conditions for large-eddy simulations," *International Journal of Heat and Fluid Flow*, vol. 27, no. 4, pp. 585–593, 2006, special Issue of The Fourth International Symposium on Turbulence and Shear Flow Phenomena - 2005.

[95] F. Nicoud and F. Ducros, *Flow, Turbulence and Combustion*, vol. 62, no. 3, pp. 183–200, 1999. [Online]. Available: https://doi.org/10.1023/a:1009995426001

[96] H. Kong, H. Choi, and J. S. Lee, "Direct numerical simulation of turbulent thermal boundary layers," *Physics of Fluids*, vol. 12, no. 10, pp. 2555–2568, 10 2000. [Online]. Available: https://doi.org/10.1063/1.1287912

[97] D. Li, K. Luo, and J. Fan, "Direct numerical simulation of heat transfer in a spatially developing turbulent boundary layer," *Physics of Fluids*, vol. 28, no. 10, p. 105104, 2016. [Online]. Available: https://doi.org/10.1063/1.4964686

[98] X. Wu and P. Moin, "Transitional and turbulent boundary layer with heat transfer," *Physics of Fluids*, vol. 22, no. 8, p. 085105, 2010. [Online]. Available: https://doi.org/10.1063/1.3475816

[99] D. G. Goodwin, R. L. Speth, H. K. Moffat, and B. W. Weber, "Cantera: An object-oriented software toolkit for chemical kinetics, thermodynamics, and transport processes," https://www.cantera.org, 2021, version 2.5.1.

[100] R. Li, G. He, F. Qin, C. Pichler, and A. A. Konnov, "Comparative analysis of detailed and reduced kinetic models for CH4+H2 combustion," *Fuel*, vol. 246, pp. 244–258, 2019. [Online]. Available: https://www.sciencedirect.com/science/article/pii/S0016236119303588

[101] H. Zhao, A. Wei, K. Luo, and J. Fan, "Direct numerical simulation of turbulent boundary layer with heat transfer," *International Journal of Heat and Mass Transfer*, vol. 99, pp. 10–19, 2016. [Online]. Available: https://www.sciencedirect.com/science/article/pii/S0017931016301831

[102] H. Schlichting and K. Gersten, *Boundary-Layer Theory*. Springer Berlin Heidelberg, 2017. [Online]. Available: https://doi.org/10.1007/978-3-662-52919-5

[103] Q. Li, P. Schlatter, L. Brandt, and D. S. Henningson, "DNS of a spatially developing turbulent boundary layer with passive scalar transport," *International Journal of Heat and Fluid Flow*, vol. 30, no. 5, pp. 916–929, 2009, the 3rd International Conference on Heat Transfer and Fluid Flow in Microscale. [Online]. Available: https://www.sciencedirect.com/science/article/pii/S0142727X09001040

[104] H. Kong, H. Choi, and J. S. Lee, "Direct numerical simulation of turbulent thermal boundary layers," *Physics of Fluids*, vol. 12, no. 10, pp. 2555–2568, 2000. [Online]. Available: https://aip.scitation.org/doi/abs/10.1063/1.1287912

[105] G. Araya and L. Castillo, "DNS of turbulent thermal boundary layers up to Re=2300," *International Journal of Heat and Mass Transfer*, vol. 55, no. 15, pp. 4003–4019, 2012. [Online]. Available: https://www.sciencedirect.com/science/article/pii/S0017931012001871

APPENDIX A SORET EFFECTS ON 1D LAMINAR UNSTRAINED FLAMES

Figure A.1 shows the effects of using different transport models: with Soret effects using the multicomponent transport model, without Soret effects using the mixture-averaged transport model, and without Soret effects using the multicomponent transport model. Simulations are performed using Cantera, with thermochemical conditions the same as for the SFWI simulation, i.e., equivalence ratio of 0.41, 70% H_2 and 30% CH_4 content. The Aramco reduced mechanism is used, same as in the SFWI simulation. Negligible effects of Soret transport is observed on the flame structure at the present thermochemical conditions.

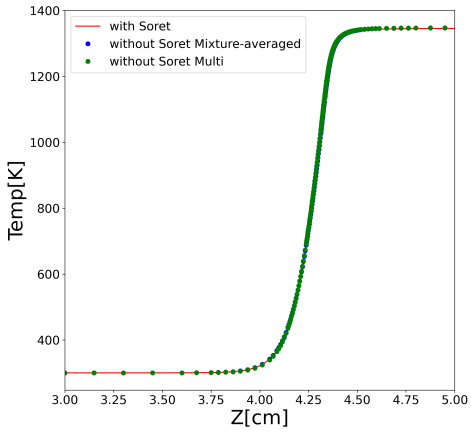

(a) Temperature

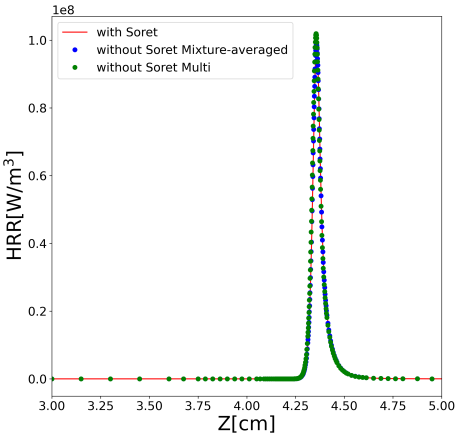

(b) Heatrelease rate

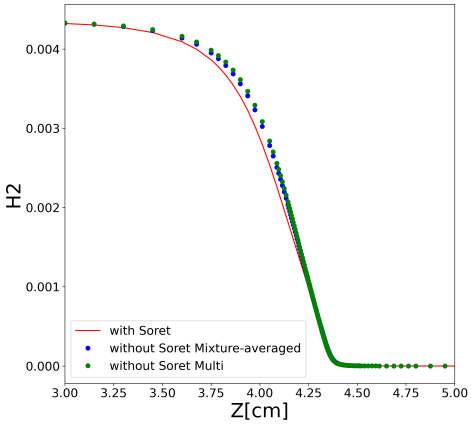

(c) Y(H2)

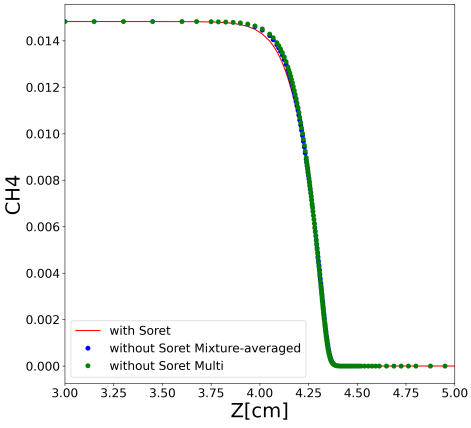

(d) Y(CH4)

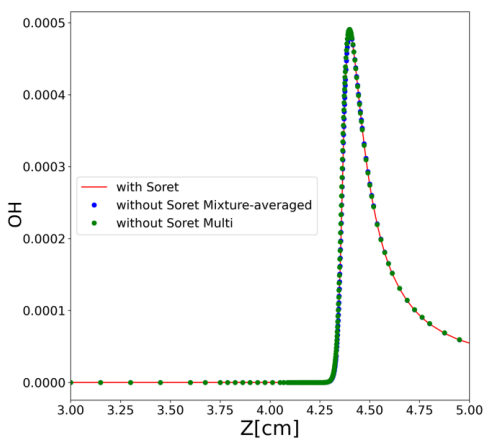

(e) Y(OH)

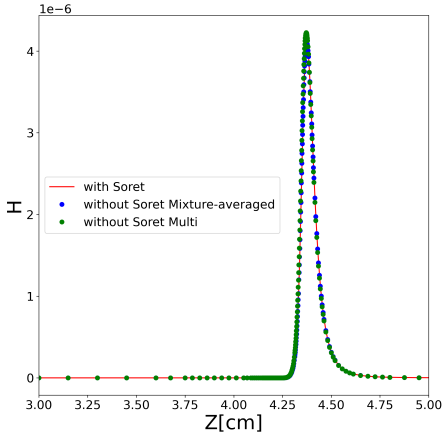

(f) Y(H)

Figure A.1 1D laminar unstrained flame structure using different transport models: with Soret effects using the multicomponent transport model, without Soret effects using the mixture-averaged transport model, and without Soret effects using the multicomponent transport model.

APPENDIX B NON-REACTIVE SWIRL FLOW

Figures B.1-B.6 present a comparison of the radial dependency of average and rms of axial, azimuthal, and radial velocity when using one and two levels of AMR in the non-reactive swirl flow simulation. Great agreement is observed between the profiles obtained with both AMR levels.

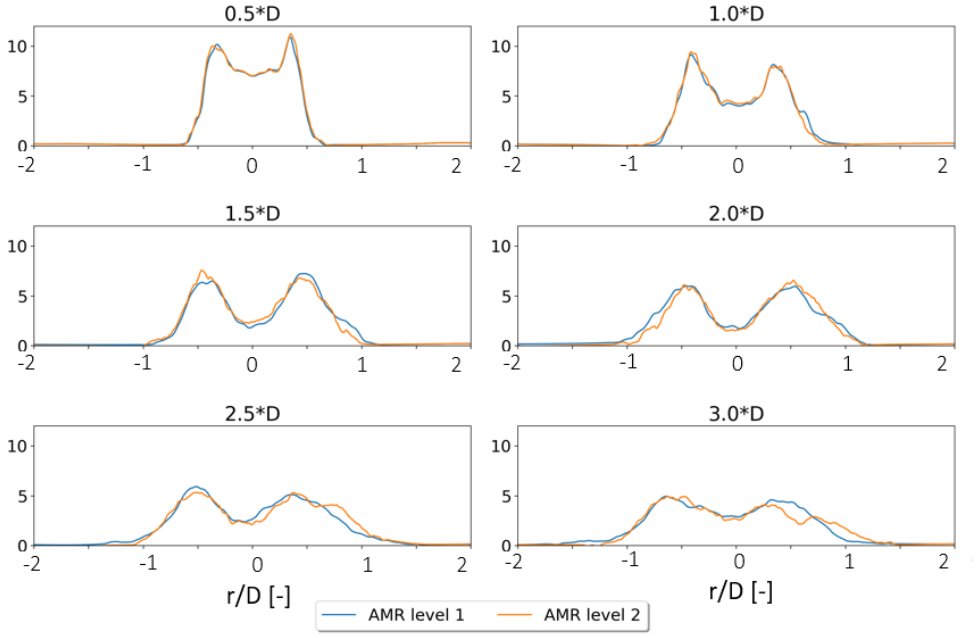

Figure B.1 Average axial velocity [m/s] for simulations with one and two levels of AMR

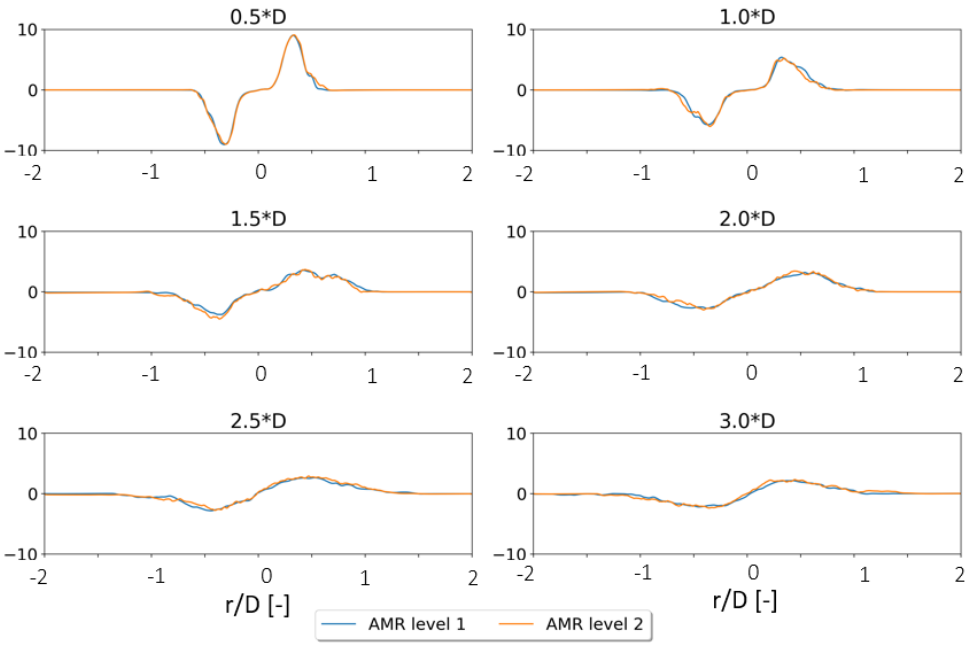

Figure B.2 Average azimuthal velocity [m/s] for simulations with one and two levels of AMR

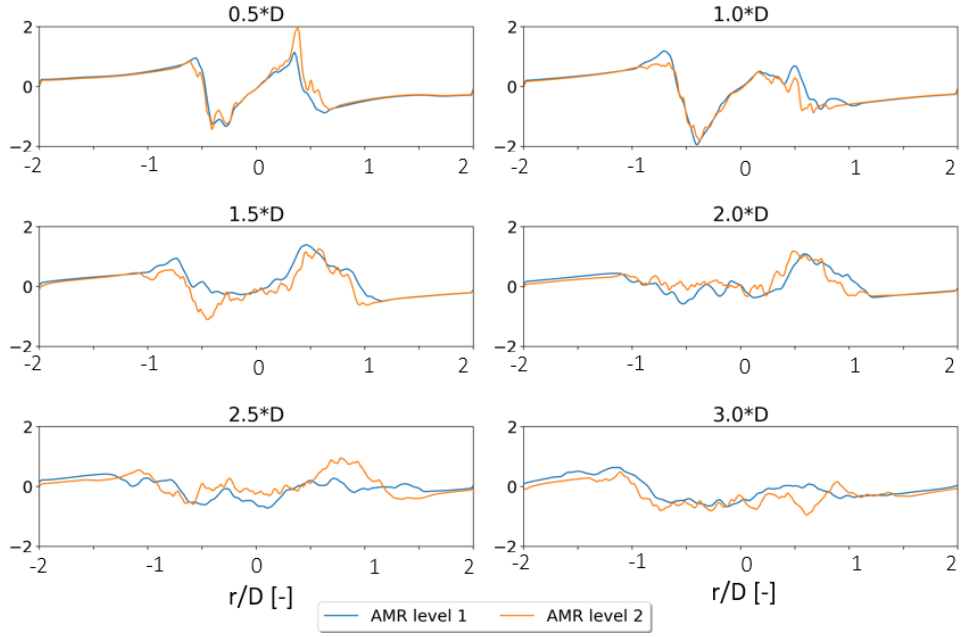

Figure B.3 Average radial velocity [m/s] for simulations with one and two levels of AMR

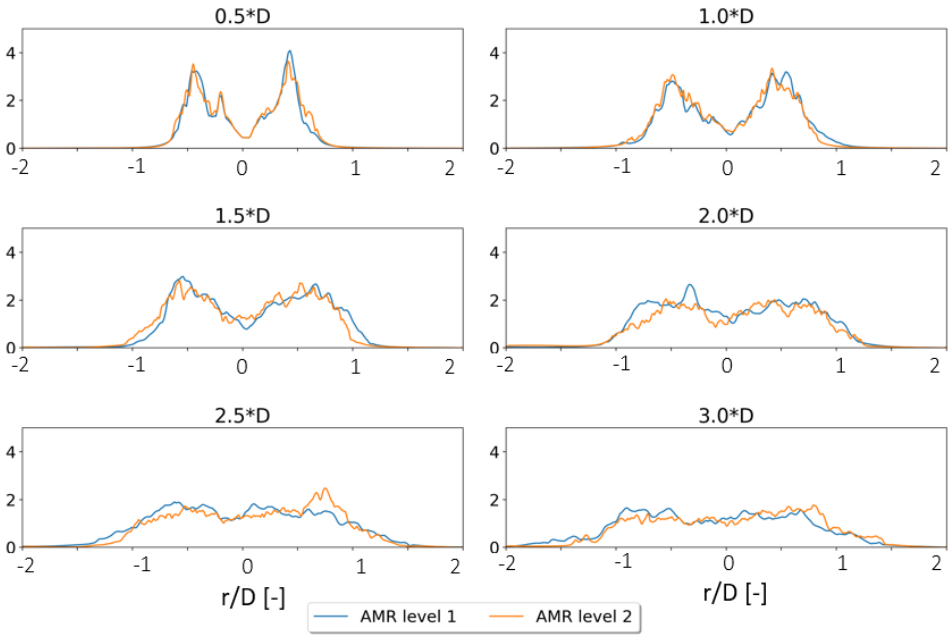

Figure B.4 Axial velocity rms [m/s] for simulations with one and two levels of AMR

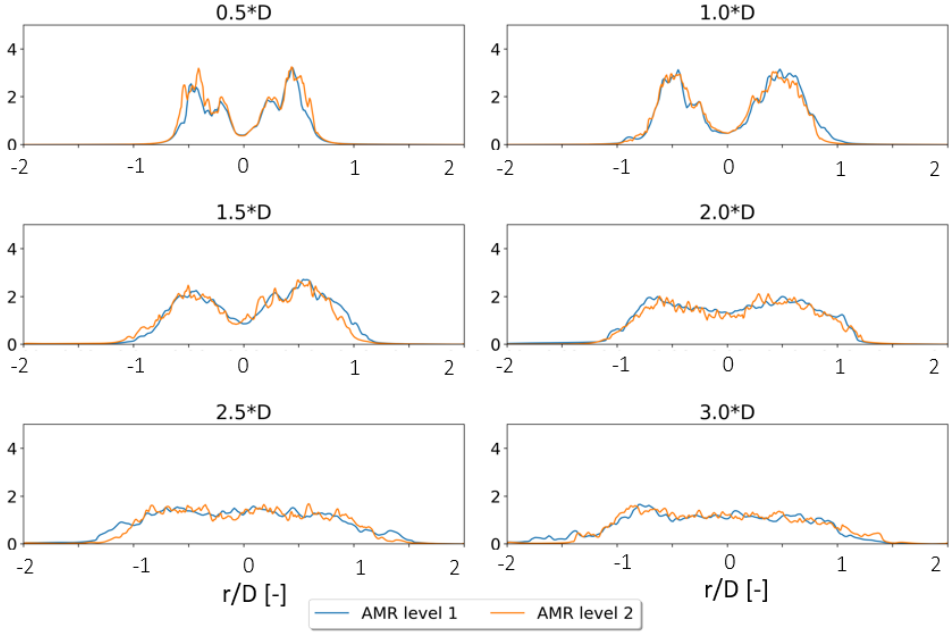

Figure B.5 Azimuthal velocity rms [m/s] for simulations with one and two levels of AMR

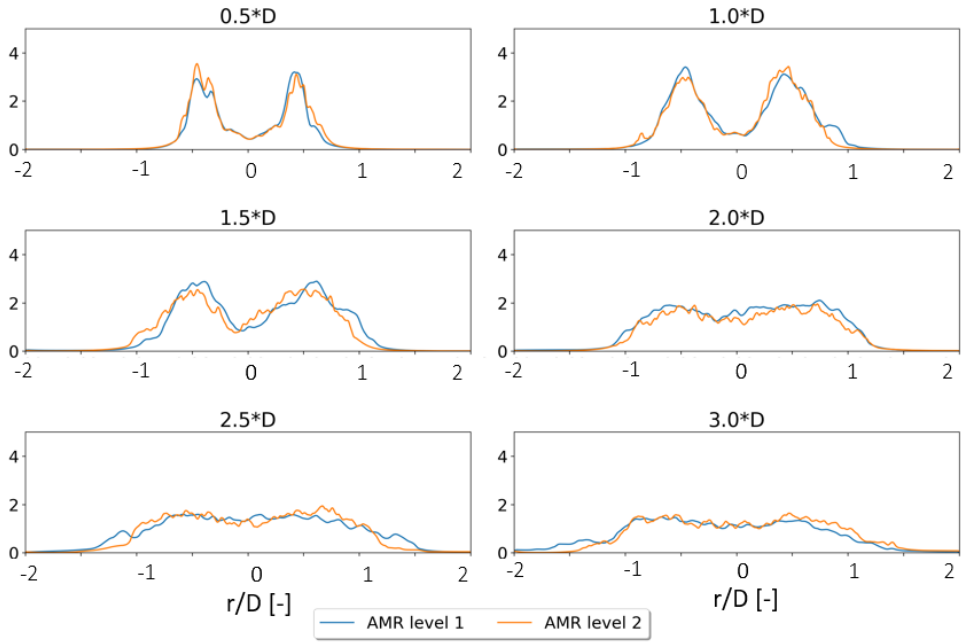

Figure B.6 Radial velocity rms [m/s] for simulations with one and two levels of AMR